IIT RESEARCH INST CHICAGO IL
EVALUATION OF TIME DOMAIN EM COUPLING TECHNIQUES, VOLUME I.(U)
AUG 80 A TAFLOVE
RADC-TR-80-251-VOL-1
NL F/G 20/14 AD-A092 031 UNCLASSIFIED 1062 \$600 osi

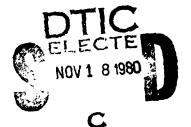
EVALUATION OF TIME DOMAIN EM COUPLING TECHNIQUES, VOL I



EVALUATION OF TIME DOMAIN EM COUPLING TECHNIQUES

IIT Research Institute

Dr. Allen Taflove



APPROVED FOR PUBLIC RELEASE; DISTRIBUTION UNLIMITED

BOC FILE COP

ROME AIR DEVELOPMENT CENTER Air Force Systems Command Griffiss Air Force Base, New York 13441

80 11 12 750

This report has been reviewed by the RADC Public Affairs Office (PA) and is releasable to the National Technical Information Service (NTIS). At NTIS it will be releasable to the general public, including foreign nations.

RADC-TR-80-251, Vol I (of two) has been reviewed and is approved for publication.

APPROVED:

Daniel E. Marren

DANIEL E. WARREN Project Engineer

APPROVED:

DAVID C. LUKE, Lt Colonel, USAF

Chief, Reliability & Compatibility Division

FOR THE COMMANDER: John P. Kluss

JOHN P. HUSS

Acting Chief, Plans Office

SUBJECT TO EXPORT CONTROL LAWS

This document contains information for manufacturing or using munitions of war. Export of the information contained herein, or release to foreign nationals within the United States, without first obtaining an export license, is a violation of the International Traffic in Arms Regulations. Such violation is subject to a penalty of up to 2 years imprisonment and a fine of \$100,000 under 22 U.S.C 2778.

Include this notice with any reproduced portion of this document.

If your address has changed or if you wish to be removed from the RADC mailing list, or if the addressee is no longer employed by your organization, please notify RADC (RBCT) Griffiss AFB NY 13441. This will assist us in maintaining a current mailing list.

Do not return this copy. Retain or destroy.

UNCLASSIFIED

	SECURITY CLASSIFICATION OF THIS PAGE (When D. Entered)	
	(7) REPORT DOCUMENTATI A PAGE	READ INSTRUCTIONS
_		BEFORE COMPLETING FORM 3. REGIPIENT'S CATALOG NUMBER
(18)	IN ACCO	131
4	RADC-TR-80-251_Vol-1 (of two) HD-7092	S. TYPE OF REPORT & PERIOD COVERED
		Final Technical Report
	EVALUATION OF TIME DOMAIN EM	7 Dec 78—29 Feb 80
	COUPLING TECHNIQUES	6. PERFORMING UTG. REPORT MCMBER
- 1	Volume I.	N/A
	7. AUTHOR(a)	8. CONTRACT OR GRANT NUMBER(#)
(10)		
	Dr.) Allen/Taflove / (5)	F30602-79-C-0039,
	TF.	30602-77-C-01631
	9. PERFORMING ORGANIZATION NAME AND ADDRESS	AREA & WORK UNIT NUMBERS
	IIT Research Institute	62702F (17) = 1
	10 West 35th Street	23380323
	Chicago IL 60616	<u> </u>
	Rome Air Development Center (RBCT)	12. REPORT DATE
j	Griffiss AFB NY 13441	August 1980
	Griffiss AFB NI 13441	
1	14. MONITORING AGENCY NAME & ADDRESS(If different from Controlling Office)	178 15. SECURITY CLASS. (of this report)
	1	, and the second of the second
	(12 17/2)	UNCLASSIFIED
	Same	154. DECLASSIFICATION DOWNGRADING
		N/A SCHEDULE
1	16. DISTRIBUTION STATEMENT (of this Report)	
ſ	17. DISTRIBUTION STATEMENT (of the abstract entered in Block 20, if different from	n Report)
ı		İ
l	Same	
j		ļ
}-	18. SUPPLEMENTARY NOTES	
		1
- 1	RADC Project Engineer: Daniel E. Warren (RBCT)	1
i		
ł		
	19. KEY WORDS (Continue on reverse side if necessary and identify by block number)	
	Electromagnetic Compatibility Finite Diff	erence Techniques
ļ1	Electromagnetic Coupling Computer	•
\	Aperture Coupling Computer Son	ftware
	Time Domain Solutions	
	O. ABSTRACT (Continue on reverse side if necessary and identify by block number)	
	This research program investigated a new tool for	or the analysis of elec-
	romagnetic coupling and shielding problems: the	he finite-difference,
- [1	ime-domain (FD-TD) solution of Maxwell's equation	ions. The objective of
	the program was to evaluate the suitability of	the FD-TD method to
- 49	letermine the amount of electromagnetic coupling	g through an aperture into
Į	an enclosed conducting container and the interac	ction and coupling of the
] 1	penetrating fields with internal electronics.	Two specific container
_	FORM	
L	D 1 JAN 73 1473 EDITION OF 1 NOV 65 IS OBSOLETE	INCLASSIFIED

SECURITY CLASSIFICATION OF THIS PAGE (When Data Enter

nia Enterna)

SECURITY CLASSIFICATION OF THIS PAGE(When Data Entered)

models were used for the evaluation. The first, a conducting cylinder with one open end; the other, the guidance section of a missile. Each of these two configurations was modeled to calculate the electromagnetic field coupled into the structure.

The following specific questions were addressed during this program:

- 1. Can the FD-TD method accurately model electromagnetic coupling into a conducting structure for arbitrary angles of incidence and arbitrary wave polarization?
- 2. Can the FD-TD method accurately model a complex structure with both irregular-shaped apertures and dielectric or permeable materials within the interior?
- 3. Can the FD-TD method predict the voltage, current, or power that the coupled field may indice on wires or cable bundles inside of a metal structure?
- 4. What are the size limits of an object that can be modeled using the FD-TD method?
- 5. What is the capability of the FD-TD method to interface with other analysis techniques, such as "Method of Moments?

Overall, this program showed that the FD-TD method can be successfully applied to electromagnetic coupling problems involving conducting structures with hole and sleeve-type apertures illuminated by a plane wave having an arbitrary polarization and angle of incidence. Further, the FD-TD method can be applied to complex cavity-like structures having internal metal and dielectric materials, as well as connecting wires. Accuracy of the FD-TD results was very good relative to the uncertainties of available experimental and numerical-theory approaches. Convergence of the electromagnetic fields to the sinusoidal steady state occurred within about 3 cycles of the incident wave when a slight value of isotropic loss was assigned to the interior of the structures modeled. This resulted in program central processor times of less than 5 minutes for FD-TD lattices containing as many as 1.5 million unknowns time-stepped to = 800 using the Control Data STAR-100 and Cyber 203 computers. max This program also established the feasibility of a hybrid MOM/FD-TD analysis technique based upon the use of Schelkunoff's equivalent electric current theorem at apertures of a cavity. This hybrid technique was shown to give consistent results for structures illuminated at both oblique and axial incidence by plane waves. Further, this technique was shown to give consistent results for apertures strongly coupled to internal wires or other metal and dielectric structures.

This program has shown that the pure FD-TD and hybrid MOM/FD-TD methods have great promise for applications involving complex conducting and dielectric structures illuminated by plane waves at arbitrary angles of incidence and polarization. Further, great promise is shown for those structures that are simultaneously electrically large compared to a wavelength and penetrated by locally complex cavity-backed apertures having dimensions comparable to a wavelength. Such structures requiring resolution of both large and small details at the same time have not been well treated by any one previous analytical or numerical approach.

1.0 BACKGROUND

Electromagnetic penetration problems are difficult to treat with many analytical or numerical methods because of the inability of these methods to simply deal with the effects of structure apertures, curvatures, corners, and internal contents. Usually, only relatively simple geometries and apertures are studied in an attempt to gain insight into the key penetration mechanisms and to allow an indirect estimate of the penetration for more complicated problems.

In RADC Contracts F30602-77-C-0163 and F30602-79-C-0039, IIT Research Institute (IITRI) investigated the application of a new approach for the direct modeling of electromagnetic interaction problems: the finite-difference, time-domain (FD-TD) solution of Maxwell's equations. The FD-TD method treats the irradiation of a structure as an initial value problem. At t=0, a plane wave source of frequency, f, is assumed to be turned on. The propagation of waves from this source is simulated by solving a finite-difference analog of the time-dependent Maxwell's equations on a lattice of cells, including the structure. Time-stepping is continued until the sinusoidal steady state is achieved at each cell. The field envelope, or maximum absolute value, during the final half wave-cycle of time-stepping is taken as the magnitude of the phasor of the steady-state field.

This method has two key advantages relative to available modeling approaches. First, it is simple to implement for complicated metal/dielectric structures because arbitrary electrical parameters can be assigned to each lattice cell using a data card deck. Second, its computer memory and running time requirement is not prohibitive for many complex structures of interest. In the RADC work, IITRI has shown the FD-TD method to be capable of accurately solving for hundred of thousands of unknown field components within a few minutes on an array-processing computer. Consistently, a ± 1 dB accuracy relative to known analytical and experimental bench marks has been achieved for a variety of dielectric and metal geometries.

 $oldsymbol{\lambda}$, the first

The objective of IITRI's RADC study was to evaluate the suitability of the FD-TD method to determine the amount of electromagnetic coupling through an aperture into an enclosed conducting container and the interaction and coupling of the penetrating fields with internal electronics. Two specific container models were used for the evaluation. The first, a conducting cylinder with one open end. The other, the guidance section of a missile. Each of these two configurations was modeled to calculate the electromagnetic field coupled into the structure.

The ultimate aim of research in this area is two-fold. First, develop an easily used general code solving for the fields within arbitrary metal/dielectric structures having multiple apertures, while assuring a known bounded level of uncertainty. And second, develop a more sophisticated intuitive understanding of basic wave penetration mechanisms in time domain, such as transient propagation through beyond-cutoff cavity interiors, field build-up at edges, and convergence to the sinusoidal steady state.

2.0 OBJECTIVES OF RADC CONTRACT F30602-79-C-0039

The first-stage evaluation of the FD-TD method, RADC Contract F30602-77-C-0163, demonstrated that the FD-TD method can be successfully applied to axial - incidence, electromagnetic wave coupling problems involving highly conducting structures with hole and sleeve-type apertures. Accuracy of the FD-TD results was very good relative to the uncertainties of available experimental and numerical-theory approaches. Convergence of the EM fields to the sinusoidal steady state occurred within about 2 cycles of the incident wave. This resulted in program running times of 3.5 minutes or less on the CDC STAR-100 for 10^5 - cell lattices.

The following questions concerning the FD-TD method remained unanswered at the conclusion of RADC Contract F30602-77-C-0163:

1. Can the FD-TD method accurately model EM coupling into a conducting structure for arbitrary angles of incidence and arbitrary wave polarization?

- 2. Can the FD-TD method accurately model a complex structure with both irregular-shaped apertures <u>and</u> dielectric or permeable materials within the interior?
- 3. Can the FD-TD method predict the voltage, current, or power that the coupled field may induce on wires or cable bundles inside of a metal structure?
- 4. What are the size limits of an object that can be modeled using the FD-TD method?
- 5. What is the capability of the FD-TD method to interface with other analysis techniques, such as "Method of Moments"?

The objective of the second-stage evaluation of the FD-TD method, RADC Contract F30602-79-C-0039, was to systematically address the five questions raised above. It was felt that favorable conclusions on most or all of these questions would probably lead to eventual application of the FD-TD method to complex EM coupling problems of interest to RADC and the electromagnetic compatibility community.

3.0 DESCRIPTION OF COUPLING ANALYSIS PROBLEMS CONSIDERED

3.1 Task 1: Prediction of the Coupling into an Open-Ended Cylinder for Broadside Incidence

IITRI employed the FD-TD technique to solve the following electromagnetic coupling problems:

<u>Interacting structure</u> - Circular (19.0 cm diameter), 68.5 cm long, open-ended aluminum cylinder (shown in Figures 3 and 4 of the Final Report);

<u>Incident wave</u> - 300 MHz plane wave propagating perpendicular to the cylinder axis (i.e., broadside to the cylinder). Wave polarization cases investigated:

Case 1 - Transverse electric (TE), i.e., wave electric field perpendicular to the plane formed by the cylinder axis and the incident wavevector;

Case 2 - Transverse magnetic (TM), i.e., wave magnetic field perpendicular to the plane formed by the cylinder axis and the incident wavevector;

<u>Desired fields</u> - Each component of total \overline{E} and total \overline{H} in the axial cross-section plane of the cylinder down to 40 cm from the open end. First, with the cross-section plane parallel to the incident transverse field component, and again with the plane parallel to the incident wavevector:

Resolution - 1/3 cm uniformly throughout the mapping planes;

<u>Plotted values</u> - In decibels relative to an incident \overline{E} of 1 volt/meter and an incident \overline{H} of 1/377 ampere/meter.

To solve these coupling problems, IITRI suitably modified an existing FD-TD computer code to model the cylinder at broadside incidence for either the TE or TM cases of wave polarization. Details of the models are given in Sections 3.1 and 3.2 of the Final Report.

3.2 Task 2: Prediction of the Coupling into a Loaded Missile Guidance Section

IITRI employed the FD-TD technique to solve the following electromagnetic coupling problems:

<u>Interacting structure</u> - Missile guidance section with two apertures: a circular one in the nose, and a sleeve fitting located 23-1/3 cm aft. Missile body geometry beyond sleeve fitting assumed to continue to infinity with constant cross-section shape. Models of interior contents investigated:

- Case 1 Dielectric materials of the nose cone shell, including separate specifications of the fiberglas shell material, phenolic cup, and magnesium fluoride infrared dome (as shown in Figures 19 - 21 of the Final Report);
- Case 2 All dielectric material of Case 1 with the addition of the following metal and dielectric interior components (located as shown in Figures 24 26 of the Final Report):

- Head coil assembly (assumed solid metal);
- Cooled detector unit CDU (assumed solid metal);
- 3) Phenolic ring around the CDU;
- 4) Preamp can (metal);
- 5) Wire connecting the CDU to the preamp can;
- 6) Wire connecting the preamp can to the metal backplane; and
- 7) Longitudinal metal support rods.

<u>Incident wave</u> - 300 MHz plane wave propagating down the axis of the structure toward its nose aperture;

<u>Desired fields</u> - Each component of total \overline{E} and total \overline{H} in two axial cross-section planes of the structure. First, with the cross-section plane parallel to the incident \overline{E} , and again with the plane parallel to the incident \overline{H} ;

Resolution - 1/3 cm uniformly throughout the mapping planes;

<u>Plotted values</u> - In decibels relative to an incident \overline{E} of 1 volt/meter and an incident \overline{H} of 1/377 ampere/meter.

To solve these coupling problems, IITRI suitably modified an existing FD-TD computer code and composed two new data card decks describing the separate cases of the internal structure of the guidance section. Details of the models are given in Sections 4.1 and 4.2 of the Final Report.

3.3 Task 3: Prediction of the Coupling to Wires or Cable Bundles

IITRI conducted a study of the ability of the FD-TD method to predict electromagnetic coupling to a wire or cable bundle using Case 2 of the missile guidance section model. As stated, this case included two connecting wires:

1) Wire 1 - between the cooled detector unit and the preamp can; and 2)
Wire 2 - between the preamp can and the metal backplane. Wire 1 and Wire 2
were really idealizations of two multiconductor wire bundles extended between the structures mentioned. Some wires of each bundle terminated in electronic components; some were small-diameter cables with grounded shields. The goal was to model the direct metal-to-metal current path through the missile guidance section. Therefore, using a simple single-wire model for each bundle,

only the ground-path current and equivalent common-mode current of each bundle was modeled using the FD-TD method.

Modeling of Wire 1 and Wire 2 was done using the FD-TD method in a direct manner by specifying each wire model as a filamentary conducting path of realistic location relative to the other components of the model. In this manner, certain transmission line properties of each wire, such as capacitance and external inductance, that arise due to its location relative to other structures are automatically accounted for in the time-domain solution of Maxwell's equations for the whole model, which includes the interaction of the wire and all adjacent structures. The transmission-line properties of each wire that arise due to internal impedance are accounted for by adjusting the model wire conductivity so that these properties match those of the actual conductor. This procedure is discussed in Section 5 of the Final Report.

3.4 Task 4: Determination of the Size Limits of an Object that can be Modeled by the FD-TD Method

IITRI conducted a study of the maximum size of an object that can be modeled using the FD-TD method, given limitations of the available computer system. In general, the computer resources needed by the FD-TD method increase for larger structures and finer spatial resolutions, since more memory and processing time is required to account for higher levels of geometric detail. Factors such as computer central memory size, data transmission rate of on-line mass storage memory, floating-point operation speed, and computer architecture were considered in this study. Details of the study are reported in Section 6 of the Final Report.

3.5 Task 5: Investigation of Interfacing the FD-TD Method with Other Analysis Techniques

Under this task, IITRI developed a new hybrid method-of-moments (MOM) / FD-TD technique based on a novel use of an aperture electric current field equivalence theorem due to Schelkunoff. This hybrid technique and its applications, described in Section 7 of the Final Report, is basically an equivalent aperture excitation method. This allows analysis of the coupling problem in two distinct steps:

- Step 1 Analysis of the relatively simple exterior problem using the method of moments to determine the equivalent excitation currents and/or fields in the aperture regions. This can be done independent of any knowledge of the interior contents of the object of interest.
- Step 2 Use of the FD-TD method to analyze the relatively complex interior problem, assuming as an excitation the equivalent currents or fields found in Step 1.

In this way, each analysis technique is applied in the structure size and complexity range that it is best suited for, allowing an overall solution that is accurate for large, simple structures with small, complex apertures or other fine interior details.

IITRI employed the hybrid MOM/FD-TD technique to solve the following electromagnetic coupling problems:

<u>Interacting structure</u> - Circular (19.0 cm diameter), 68.5 cm long, open-ended aluminum cylinder (shown in Figures 40, 41, 52, and 53 of the Final Report);

<u>Incident wave</u> - 300 MHz plane wave propagating towards the open end of the cylinder. Wave angles of incidence investigated:

Case 1 - Axial incidence;

Case 2 - Oblique incidence (wavevector at a 45° angle with respect to the cylinder axis) and transverse magnetic (TM) polarization;

<u>Desired fields</u> - Each component of total \overline{E} and total \overline{H} in the axial cross section plane of the cylinder down to 40 cm from the open end. First, with the cross-section plane parallel to the incident \overline{H} component, and again with the plane parallel to the incident \overline{E} component;

Resolution - 0.5 cm uniformly throughout the mapping planes;

<u>Plotted values</u> - In decibels relative to an incident \overline{E} of 1 volt/meter and an incident \overline{H} of 1/377 ampere/meter.

To solve these coupling problems, IITRI suitably modified two existing FD-TD computer codes to accept data for the equivalent aperture electric current excitation. These data were then obtained from Drs. D. Wilton and A. Glisson* who employed their MOM code for the electric currents over the cylinder aperture locus when shorted, as specified by the Schelkunoff theorem. Details of the models are given in Sections 7.4.1 and 7.4.2 of the Final Report.

IITRI also employed the hybrid MOM/FD-TD technique to solve the electromagnetic coupling problem of the loaded missile guidance section, which had been previously solved by IITRI during this research program using the pure FD-TD method (Task 2, Case 2). The excitation consisted of MOM-derived data for the equivalent electric current excitation over the nose aperture and the sleeve-fitting aperture when shorted, as specified by the Schelkunoff theorem. These data were again obtained from Drs. D. Wilton and A. Glisson. Details of this model are given in Section 7.4.3 of the Final Report.

All hybrid MOM/FD-TD numerical results were then compared to available pure FD-TD results (for the open-ended cylinder at axial incidence, and the loaded missile guidance section), and to available pure MOM results (for the open-ended cylinder at axial incidence and at oblique incidence). The goal was to establish the consistency and accuracy of the hybrid modeling technique.

4.0 RESULTS AND DISCUSSION

Completion of Program Task 1 demonstrates the capability of the FD-TD method to accurately model the electromagnetic fields coupled into a cylindrical structure which is illuminated with an electromagnetic plane wave having an arbitrary polarization. Elements of Task 5 demonstrate this modeling capability for an arbitrary wave angle of incidence, as well.

Completion of Program Task 2 demonstrates the capability of the FD-TD method to map fields coupled into a complex conical structure that has both irregular shaped apertures and interior dielectric and metallic materials.

^{*}Consultants to IITRI from the EE Department, University of Mississippi.

Determination of the accuracy bound for this method, as applied to complex structures, awaits the results of future experimental programs since other numerical approaches cannot deal directly with this level of complexity. No comparative data is available at this time.

Completion of Program Task 3 demonstrates the ability of the FD-TD technique to directly predict the current that the coupled fields may induce on a wire or bundle of wires which is located inside a complicated structure (such as a missile guidance section). Here, the observed parallelism of the computed magnetic field contours near the modeled wire(s) is employed in combination with Ampere's law to translate FD-TD-computed magnetic fields to wire current magnitudes. Confirmation of the FD-TD-computed wire currents is required in a future experimental program.

Completion of Program Task 4 demonstrates the computer resources needed to implement the FD-TD technique for a given size structure illuminated by electromagnetic waves of a given frequency. This task leads to the conclusions that: 1) If on-line mass storage is used, the structure size is limited mainly by the maximum "wall clock time" of the program which is acceptable to both the user of the program and the operator of the computing center; 2) If mass storage is not used, the structure size is sharply limited by the available central memory because larger objects (or ones with higher spatial resolution) simply cannot be specified within the bounds of the memory field.

Completion of Program Task 5 leads to the following conclusions: 1) Hybrid MOM/FD-TD results are consistent with previous data derived from both pure MOM and pure FD-TD methods, implying the validity of the hybrid formulation; 2) Arbitrary angles of wave incidence can be treated using the hybrid MOM/FD-TD method simply by specifying the proper aperture equivalent current excitation, without having to change the FD-TD geometry of the structure; 3) Wires or other structures in the interior of a cavity strongly coupled to an aperture can be easily and consistently modeled using the hybrid MOM/FD-TD approach; and 4) Complex sub-sections of elongated simply-shaped structures are prime candidates for detailed modeling of the interior penetrating fields via the hybrid MOM/FD-TD method.

Overall, under RADC Contract F30602-79-C-0039, IITRI demonstrated that the FD-TD method can be successfully applied to electromagnetic coupling problems involving highly-conducting structures with hole and sleeve-type apertures illuminated by a plane wave having an arbitrary polarization and angle of incidence. Further, IITRI showed that the FD-TD method can be applied to complex cavity-like structures having internal metal and dielectric materials, as well as connecting wires. Accuracy of the FD-TD results was very good relative to the uncertainties of available experimental and numerical-theory approaches. Convergence of the electromagnetic fields to the sinusoidal steady state occurred within about 3 cycles of the incident wave when a slight value of isotropic conductivity was assigned to the interior of the structures modeled. This resulted in program central processor times of less than 5 minutes for FD-TD lattices containing as many as 1.5 million unknowns time-stepped to $n_{\text{max}} = 800$ using the Control Data STAR-100 and Cyber 203 computers.

During this research program, IITRI also established the feasibility of a hybrid MOM / FD-TD analysis technique based upon the use of Schelkunoff's equivalent current theorem at apertures of a cavity. This hybrid technique was shown to give consistent results for structures illuminated at both oblique and axial incidence by plane waves. Further, this technique was shown to give consistent results for apertures strongly coupled to internal wires or other metal and dielectric structures.

IITRI has shown that the pure FD-TD and hybrid MOM / FD-TD methods have great promise for applications involving complex conducting and dielectric structures illuminated by plane waves at arbitrary angles of incidence and polarization. Further, great promise is shown for those structures that are simultaneously electrically large compared to a wavelength and penetrated by locally complex cavity-backed apertures having dimensions comparable to a wavelength. Such structures requiring resolution of both large and small details at the same time have not been well treated by any one previous analytical or numerical approach.

PREFACE

IIT Research Institute (IITRI) is pleased to submit this Final Report on "Evaluation of Time Domain Electromagnetic Coupling Techniques" to Rome Air Development Center (RADC/RBCT). The report covers work performed by IITRI under Air Force Contract No. F30602-79-C-0039, designated as IITRI Project No. E6461. The report is in two volumes. Volume 1 covers details of the technical work, including relevant theory and numerical results. Volume 2 provides listings of the Fortran computer programs used to obtain the results of Volume 1.

The principal investigator on this program was Dr. Allen Taflove, with support provided by Dr. Korada Umashankar of IITRI on Task 5; Mr. Neil Robertson of IITRI on data reduction and contour map plotting; and Prof. Donald Wilton and Dr. Allen Glisson of the University of Mississippi on computation of frequency-domain data for checking of results and for Task 5. The project duration was 7 December 1978 to 29 February 1980.

Respectfully submitted, IIT RESEARCH INSTITUTE

ale Tollow

Allen Taflove, Ph.D. Research Engineer

TABLE OF CONTENTS

		Page
PREF	ACE	ii
1.0	INTRODUCTION	1
2.0	THE FD-TD METHOD	3
	2.1 Basic Ideas	3
	2.2 Computational Details for a Uniform, Cubic Lattice	8
	2.3 Initial Evaluation of the FD-TD Method - Results of Previous RADC Contract F30602-77-C-0163	23
3.0	PROGRAM TASK 1: PREDICTION OF THE COUPLING INTO AN OPEN-ENDED CYLINDER	28
	3.1 Broadside Incidence and Transverse Electric (TE) Wave Polarization	28
	3.2 Broadside Incidence and Transverse Magnetic (TM) Wave Polarization	39
	3.3 Oblique Incidence and Transverse Magnetic (TM) Wave Polarization	41
	3.4 Conclusions	48
4.0	PROGRAM TASK 2: PREDICTION OF THE COUPLING INTO A MISSILE GUIDANCE SECTION	49
	4.1 Model 1 - Includes the Interior Dielectric Material	49
	4.2 Model 2 - Includes the Key Interior Metal Components as Well as the Dielectric Material	56
	4.3 Conclusions	66
		00
5.0	PROGRAM TASK 3: PREDICTION OF THE COUPLING TO WIRES OR CABLE BUNDLES	67
	5.1 Wire Model	67
	5.2 Results	69
	5.3 Conclusions	71

TABLE OF CONTENTS (cont.)

			Page
6.0	PRO(GRAM TASK 4: DETERMINATION OF THE SIZE LIMITS OF AN OBJECT THAT CAN BE MODELED BY THE FD-TD METHOD	72
	6.1	General Considerations	
	6.2	Required Computer Memory	72
	6.3	Required Computer Processing Time	73
	6.4	Impact of Requirements for Computer Memory, CP Time, and PP Time	77
7.0	PRO0	GRAM TASK 5: INVESTIGATION OF INTERFACING THE FD-TD METHOD WITH OTHER ANALYSIS TECHNIQUES	79
	7.1	Introduction	79
	7.2	Basis of the Hybrid Technique	80
	7.3	Canonical Case Studies: MOM/MOM Hybrid Technique	87
	7.4	Case Studies: MOM/FD-TD Hybrid Technique	95
8.0	DISC	CUSSION AND CONCLUSIONS	119
REFE	RENCE	ES	120
APPEI	XIDN	A - Analytical and Numerical Formulation of the Perfectly Conducting Body of Revolution	123
	Ι.	<pre>Integral Equation: Coupled Form</pre>	123
	II.	Modal Form of Equations	127
I	II.	Reduction to Modal Matrix Form	131
	IV.	Modal Excitation Terms	137
	٧.	Modal Matrix Solution	138
1	VI.	Application to the Hybrid MOM/FD-TD Case Studies of Section 7.4	140
APPE	XIDN	B - Integral Equations for the Finite Wire / Narrow Slot Geometry	150

LIST OF FIGURES

Figur	<u>e</u>	Page
1	Positions of the Field Components About a Unit Cell of the Yee Lattice	4
2	Ideal FD-TD Lattice Truncation Conditions	16
3	Horizontal Symmetry Plane View of Open-Ended Cylinder, TE/Broadside Case	29
4	Cross-Section of Model of Open-Ended Aluminum Cylinder, TE/Broadside Case	30
5	Convergence of the Computed Electric Field Along the Cylinder Axis, TE/Broadside Case	32
6	Comparison of Results for the Axial Magnetic Field Within the Cylinder, TE/Broadside Case	33
7	Computed E _Z Contours in Cylinder Horizontal Symmetry Plane, TE/Broadside Case	34
8	Computed H _X Contours in Cylinder Horizontal Symmetry Plane, TE/Broadside Case	35
9	Computed Hy Contours in Cylinder Horizontal Symmetry Plane, TE/Broadside Case	36
10	Computed Electric Field Contours in the Cylinder Vertical Obs Plane, TE/Broadside Case	. 37
11	Computed Magnetic Field Contours in the Cylinder Vertical Obs Plane, TE/Broadside Case	. 38
12	Convergence of the Computed Magnetic Field Along the Cylinder Axis, TM/Broadside Case	40
13	Comparison of Results for the Axial Electric Field Within the Cylinder, TM/Broadside Case	42
14	Computed H _Z Contours in Cylinder Horizontal Symmetry Plane, TM/Broadside Case	43
15	Computed E _x Contours in Cylinder Horizontal Symmetry Plane, TM/Broadside Case	44

Figure		<u>Page</u>
16	Computed E _y Contours in Cylinder Horizontal Symmetry Plane, TM/Broadside Case	45
17	Computed Electric Field Contours in the Cylinder Vertical Obs Plane, TM/Broadside Case	46
18	Computed Magnetic Field Contours in the Cylinder Vertical Obs Plane, TM/Broadside Case	47
19	Geometry of Nose Cone Model at Vertical Symmetry Plane, Showin Component Materials	
20	Geometry of Nose Cone Model at Horizontal Symmetry Plane, Showing Component Materials	v- 51
21	Key Cross-Sections of Nose-Cone Model	52
22	Computed Field Contours in Nose Cone Vertical Symmetry Plane.	54
23	Computed Field Contours in Nose Cone Horizontal Symmetry Plane	55
24	Geometry of Nose Cone Model at Vertical Symmetry Plane, Showing Component Materials	57
25	Geometry of Nose Cone Model at Horizontal Observation Plane, Showing Component Materials	58
26	Key Cross-Sections of Nose Cone Model. Head-Coil Assembly and Cooled Detector Unit Not Shown	i 59
27	Computed E_Z Field Contours in Nose Cone Vertical Symmetry Plane (in DB)	61
28	Computed H_X Contours in Nose Cone Vertical Symmetry Plane (in DB)	62
29	Computed Ey Field Contours in Nose Cone Vertical Symmetry Plan (in DB)	ne 63
30	Electric Field Contours in Nose Cone Horizontal Observation Plane (in DB)	64
31	Magnetic Field Contours in Nose Cone Horizontal Observation Plane (in DB)	65

Figure		Page
32	Geometry of Ampere's Law	70
33	Perfectly Conducting Scatterer with Aperture	81
34	MOM/MOM Hybrid Technique	83
35	MOM/FD-TD Hybrid Technique	85
36	Geometry of Wire Scatterer Behind Narrow Slot	88
37	Shadow-Side Slot Magnetic Current Distribution in Presence of the Screen and the Wire	90
38	Wire Electric Current Distribution in the Presence of the Screen and the Narrow Slot	91
39	Multiport Generalized Network Representation for Hybriding the Method of Moments Technique	94
40	View of MOM/FD-TD Hybrid Cylinder Model at FD-TD Lattice Plane i = 24.5 for Axial Incidence Case (Case No. 1)	96
41	Cross-Section of Cylinder Model for MOM/FD-TD Hybrid Case No. 1	97
42	Comparison of Computed Radial Electric Field Distribution Along Axis of Cylinder	99
43	Comparison of Computed Radial Electric Field Distribution Along Axis of Cylinder	100
44	Comparison of Computed E_Z Contours in Horizontal Symmetry Plane	101
45	Comparison of Computed H_X Contours in Horizontal Symmetry Plane	102
46	Comparison of Computed Hy Contours in Horizontal Symmetry Plane	103
47	Comparison of Computed E_Z Contours in Vertical Symmetry Plane	104
48	Comparison of Computed H _X Contours in Vertical Symmetry Plane	105

Figure		<u>Page</u>
49	Comparison of Computed E_y Contours in Vertical Symmetry Plane	106
50	Computed Field Contours in Cylinder Horizontal Symmetry Plane	107
51	Computed Field Contours in Cylinder Vertical Symmetry Plane	108
52	View of MOM/FD-TD Hybrid Cylinder Model at FD-TD Lattice Plane i = 24.5 for Oblique Incidence, TM Polarization Case (Case No. 2)	110
53	Cross Section of Cylinder Model for MOM/FD-TD Hybrid Case No. 2	111
54	Comparison of Results for the Axial Electric Field Within the Cylinder, 45°/TM Incidence Case	112
55	View of MOM/FD-TD Missile Guidance Section Model at FD-TD Lattice Plane i = 24.5 for Axial Incidence (Case No. 3)	113
56	Comparison of Computed H_X Contours in Nose Cone Vertical Symmetry Plane	116
57	Comparison of Computed H_{χ} Field Along a Vertical Cut Through the Nose Cone at the Sleeve Fitting	117
58	Comparison of Computed E_Z Field Along a Vertical Cut Through the Nose Cone at the Sleeve Fitting	118
A-1	Geometry of Perfectly Conducting Body of Revolution	125
A-2a	Generating Arc at ϕ = 0 of the Body of Revolution	132
A-2b	Generating Arc at ϕ = 0 of the Body of Revolution	133
A-3	Coordinate Systems for MOM/FD-TD Hybrid Analysis of Open-Ended Cylinder at Cylinder Aperture (Axial Incidence Case and 45°/TM Incidence Case)	d M 141

_	igure		Page
	A-4	Mode Coefficients for Aperture Equivalent Electric Current, Hybrid MOM/FD-TD Formulation of Axial Incidence Illumination of Open-Ended Cylinder	142
	A-5a	Mode Coefficients for Aperture Equivalent Electric Current, Hybrid MOM/FD-TD Formulation of Oblique Incidence TM Illumination of Open-Ended Cylinder	
	A-5b	Mode Coefficients for Aperture Equivalent Electric Current, Hybrid MOM/FD-TD Formulation of Oblique Incidence TM Illumination of Open-Ended Cylinder	146
	A-6	Geometry and Coordinate Systems for MOM/FD-TD Hybrid Analysis of Missile Guidance Section, Axial Incidence	148
	A-7	Mode Coefficients for Aperture Equivalent Electric Current, Hybrid MOM/FD-TD Formulation of Axial Incidence Illumination of Missile Guidance Section	149

EVALUATION

The purpose of this effort was to further examine the capabilities of the Finite Difference-Time Domain (FD-TD) technique when used to predict electromagnetic coupling. This technique has demonstrated capabilities far superior to any developed thus far. The FD-TD technique can model a structure that consists of a number of materials including dielectrics and finite conductors. This technique has been used to map the electromagnetic fields coupled through complex shaped apertures and the currents induced on wires behind the aperture. There is no restriction on the direction of incidence or polarization.

The FD-TD technique has been hybridized with "Method of Moments" to improve the economy of computer resources, and increase the range of applicability of both techniques.

In order for the FD-TD technique to receive wide distribution it is recommended that this technique be developed into a user oriented computer code. As FD-TD is used more, the results can be used to impact further development of this technique.

Samiel E. Marran

DANIEL E. WARREN

Project Engineer

VOLUME 1 - THEORY AND NUMERICAL RESULTS

1.0 INTRODUCTION

Electromagnetic penetration problems are difficult to treat with many analytical or numerical methods because of the inability of these methods to simply deal with the effects of structure apertures, curvatures, corners, and internal contents. Usually, only relatively simple geometries and apertures are studied in an attempt to gain insight into the key penetration mechanisms and to allow an indirect estimate of the penetration for more complicated problems.

This research program investigated the application of a new approach for the direct modeling of electromagnetic interaction problems: the finite-difference, time-domain (FD-TD) solution of Maxwell's equations. The FD-TD method treats the irradiation of a structure as an initial value problem. At t=0, a plane wave source of frequency, f, is assumed to be turned on. The propagation of waves from this source is simulated by solving a finite-difference analog of the time-dependent Maxwell's equations on a lattice of cells, including the structure. Time-stepping is continued until the sinusoidal steady state is achieved at each cell. The field envelope, or maximum absolute value, during the final half wave-cycle of time-stepping is taken as the magnitude of the phasor of the steady-state field.

This method has two key advantages relative to available modeling approaches. First, it is simple to implement for complicated metal/dielectric structures because arbitrary electrical parameters can be assigned to each lattice cell using a data card deck. Second, its computer memory and running time requirement is not prohibitive for many complex structures of interest. In recent work, the FD-TD method has been shown capable of accurately solving for hundreds of thousands of unknown field components within a few minutes on an array-processing computer. Consistently, a + 1 dB accuracy relative to

known analytical and experimental bench marks has been achieved for a variety of dielectric and metal geometries.

The objective of the present study is to more completely evaluate the suitability of the FD-TD method to determine the amount of electromagnetic coupling through an aperture into an enclosed conducting container and the interaction and coupling of the penetrating fields with internal electronics. Two specific container models are used for the evaluation. The first, a conducting cylinder with one open end. The other, the guidance section of a missile. Each of these two configurations is modeled to calculate the electromagnetic field coupled into the structure.

The ultimate aim of research in this area is two-fold. First, develop an easily used general code solving for the fields within arbitrary metal/dielectric structures having multiple apertures, while assuring a known bounded level of uncertainty. And second, develop a more sophisticated intuitive understanding of basic wave penetration mechanisms in time domain, such as transient propagation through beyond-cutoff cavity interiors, field build-up at edges, and convergence to the sinusoidal steady state.

This report first reviews in Section 2.0 the basic theory behind the FD-TD method, referencing extensively technical report RADC-TR-78-142, "Time Domain Solutions for Electromagnetic Coupling," the final technical report on Contract F30602-77-C-0163 (the forerunner of the present contract). This section also briefly summarizes the results of the previous contract.

Sections 3.0 through 7.0 document the results of the present research effort in terms of the following five tasks:

- Task 1: Prediction of the Coupling into an Open-Ended Cylinder;
- Task 2: Prediction of the Coupling into a Missile Guidance Section,
- Task 3: Prediction of the Coupling to Wires or Cable Bundles,
- Task 4: Determination of the Size Limits of an Object that can be Modeled by the FD-TD Method; and
- Task 5: Investigation of Interfacing the FD-TD Method with Other Analysis Techniques.

Appendices A and B provide theoretical and numerical background to the results of Task 5. These appendices discuss the basis of the hybrid technique involving the Method of Moments and the FD-TD method.

2.0 THE FD-TD METHOD

This section will review the following topics relevant to the use of the FD-TD method: 1) the basic ideas behind the method; 2) computational details; and 3) past usages and results in RADC Contract F30602-77-C-0163.

2.1 Basic Ideas

2.1.1 Wave Tracking

The FD-TD method is a direct solution of Maxwell's time-dependent curl equations. The goal is to model the propagation of an electromagnetic wave into a volume of space containing a dielectric or conducting structure. By time stepping, i.e., repeatedly implementing a finite-difference analog of the curl equations at each cell of the corresponding space lattice, the incident wave is tracked as it first propagates to the structure and then interacts with it via surface current excitation, diffusion, penetration, and diffraction. Wave tracking is completed when the desired late-time or sinusoidal steady state behavior is observed at each lattice cell. The rationale for this procedure is that it achieves simplification by analyzing the interaction of the wavefront with portions of the structure surface at a given instant in time, rather than attempting a simultaneous solution of the entire problem.

Time stepping for the FD-TD method is accomplished by an explicit finite-difference procedure due to Yee [1]. For a cubic-cell space lattice, this procedure involves positioning the components of \overline{E} and \overline{H} about a unit cell of the lattice as shown in Figure 1, and evaluating \overline{E} and \overline{H} at alternate half time steps. In this manner, centered difference expressions can be used for both the space and time derivatives to attain second-order accuracy in the space and time increments without requiring simultaneous equations to compute the fields at the latest time step.

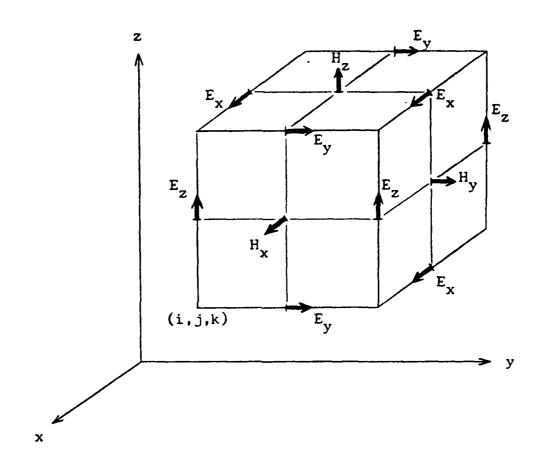


Fig. 1 POSITIONS OF THE FIELD COMPONENTS
ABOUT A UNIT CELL OF THE YEE LATTICE

2.1.2 Modeling the Structure of Interest

The finite-difference formulation of the FD-TD method allows the straightforward modeling of the surfaces and interiors of arbitrary dielectric or conducting structures. The structure of interest is mapped into the space lattice by first choosing the space increment and then employing a data card deck to assign values of permittivity and conductivity to each component of \overline{E} . No special handling of electromagnetic boundary conditions at media interfaces is required because the curl equations generate these conditions in a natural way by themselves. Therefore, the basic computer program need not be modified to change from structure to structure. In this manner, inhomogeneities or fine details of the structure can be modeled with a maximum resolution of one unit cell; thin surfaces can be modeled as infinitely thin, stepped-edge sheets.

The explicit formulation of the FD-TD method is particularly suited for programming with minimum storage and execution time using recently developed array-processing computers. First, the required computer storage and running time increases linearly with N, the total number of unknown field components. Computer techniques (such as the method of moments) which require the solution of simultaneous equations usually have a storage requirement proportional to N^2 and a running time proportional to N^2 to N^3 [2]. Second, since all FD-TD operations are explicit and can be performed in parallel, rapid array-processing techniques can be readily applied. As will be demonstrated later, these can be employed to solve for 10^5 - 10^6 field components in a single FD-TD problem, as opposed to a maximum of about 10^3 field components for conventional approaches using simultaneous equation solutions [2].

2.1.3 Algorithm Refinements

Yee applied the FD-TD method to compute the waveforms of TM and TE pulses scattered from infinitely long, rectangular cross-section, conducting cylinders. Other workers investigated electromagnetic pulse interactions in time-varying inhomogeneous media [3], with metallic bodies of revolution [4], and with detailed models of aircraft [5]. Three distinct problems emerged in the process of adapting the FD-TD method to model realistic situations:

- 1. Lattice truncation conditions. The field components at the lattice truncation planes cannot be determined directly from the Maxwell's equations analog and must be computed using an auxiliary radiative truncation condition. However, care must be exercised because this condition must not cause excessive spurious reflection of waves scattered outward by the structure modeled. The goal is to formulate truncation planes as close as possible to the structure (to minimize computer storage), and yet achieve virtual invisibility of these planes to all possible waves within the lattice.
- 2. Plane wave source condition. The simulation of either an incident plane-wave pulse or single-frequency plane wave should not take excessive storage or cause spurious wave reflections. The former would occur if the incident wave is programmed as an initial condition; the latter would occur if the incident wave is programmed as a fixed field excitation along a single lattice plane.
- 3. Sinusoidal steady state information. Such data can be obtained either by (1) directly programming a single-frequency incident plane wave or (2) performing a separate Fourier transformation step on the pulse waveform response. Both methods require time stepping to a maximum time equal to several wave periods at the desired frequency. The second method has two additional requirements. First, a short rise time pulse suffers from accumulating waveform error due to overshoot and ringing as it propagates through the space lattice. This leads to a numerical noise component which should be filtered before Fourier transformation. Second, Fourier transformation of many lattice-cell field vs. time waveforms (each probably extending over hundreds of time steps) would significantly add to the total requirements for computer storage and execution time.

Previous work leading to RADC Contract F30602-77-C-0163 described efforts to solve the above problems for the case of the cubic-unit-cell space lattice [6], [7]. Simple truncation conditions were developed for two- and three-dimensional lattices that reduced the reflection coefficient of closely-positioned truncation planes to the order of 0.1 for waves of arbitrary incidence. A plane-wave source condition was described that allowed generation of

an arbitrary pulsed or sinusoidal incident wave without requiring any additional storage and without causing spurious wave reflections. Finally, it was shown that sinusoidal steady-state data could be computed using the FD-TD method by directly programming a single-frequency incident plane wave and time-stepping to the steady state over several periods of the incident wave. Observed accuracy for low-permittivity cylindrical dielectric geometries was ± 1 dB at points of electric field maxima, and ± 1 lattice cell in locating electric field maxima and minima.

Under RADC Contract F30602-77-C-0163, additional FD-TD method provisions were developed to allow accurate solutions for the fields penetrating metal structures having one or more apertures [8]. This class of structures exhibits a different electromagnetic penetration response than convex dielectric objects due to such phenomena as aperture coupling, edge effects, and beyond-cutoff interiors. Further, the reflection coefficient of the metal surfaces modeled is larger than that of dielectric surfaces, leading to increased diffraction and the necessity for improved lattice truncation conditions. The new FD-TD method provisions are now qualitatively discussed.

The first algorithm development involves the introduction of an anisotropic lossy air medium outside of the modeled structure to aid in reducing the effective reflection coefficient of the lattice truncation planes. Modeling of such a medium is possible because separate difference equations are available for each field vector component, thus allowing individual specification of loss to each field component. For the three-dimensional case, it is useful to specify an anisotropic electric field loss, $\sigma_{\mbox{\scriptsize ext}},$ in the free-space region exterior to the structure. This loss term is used only in the difference equations for the electric field components not present in the incident plane wave. It is selected to induce 1/e decay of these components as they propagate over a distance about equal to the total dimension of the lattice. These choices avoid any exponential decay of the incident wave, which would lead to serious modeling error for structure sizes comparable to the 1/e distance. Further, the resulting modified scattered wave is reduced in amplitude upon reaching the lattice truncations and is further damped as its remnants reverberate between the structure and the truncations. tion of this development has been found to be important in maintaining a ± 1

dB accuracy of the FD-TD results for metal structures. For low permittivity dielectric structures, the assumption of completely lossless air in the exterior region is sufficient for this accuracy level.

The second algorithm development involves the introduction of a small isotropic conductivity, $\sigma_{\rm int}$, within the interior of the modeled metal structure. The purpose of modeling the slightly lossy air is to cause the reverberating fields within the structure to converge more rapidly to the expected steady-state condition, especially for the case when the interior cavity volume is normally beyond cutoff at the frequency of the incident plane wave. In this case, the transient internal fields are highly reactive (carry little real power flow) and quickly dissipate when forced to supply energy to maintain an electric field distribution across a slightly lossy medium.

Accurate results are obtained in these circumstances when $\sigma_{\mbox{\scriptsize int}}$ is chosen to provide an equivalent 10 dB of loss for a plane wave propagating the full length of the metal structure interior.

2.2 Computational Details for a Uniform, Cubic Lattice

2.2.1 System of Finite-Difference Equations

Using the MKS system of units, and assuming that the dielectric parameters, μ , ϵ , and σ , are independent of time, the following system of scalar equations is equivalent to Maxwell's equations in the rectangular coordinate system (x, y, z):

$$\frac{\partial H_{X}}{\partial t} = \frac{1}{\mu} \left(\frac{\partial E_{Y}}{\partial z} - \frac{\partial E_{Z}}{\partial y} \right) \tag{1a}$$

$$\frac{\partial H_y}{\partial t} = \frac{1}{u} \left(\frac{\partial E_z}{\partial x} - \frac{\partial E_x}{\partial z} \right) \tag{1b}$$

$$\frac{\partial H_z}{\partial t} = \frac{1}{u} \left(\frac{\partial E_x}{\partial v} - \frac{\partial E_y}{\partial x} \right) \tag{1c}$$

$$\frac{\partial E_{x}}{\partial t} = \frac{1}{\varepsilon} \left(\frac{\partial H_{z}}{\partial y} - \frac{\partial H_{y}}{\partial z} - \sigma E_{x} \right)$$
 (1d)

$$\frac{\partial E_y}{\partial t} = \frac{1}{\varepsilon} \left(\frac{\partial H_x}{\partial z} - \frac{\partial H_z}{\partial x} - \sigma E_y \right)$$
 (1e)

$$\frac{\partial E_z}{\partial t} = \frac{1}{\varepsilon} \left(\frac{\partial H_y}{\partial x} - \frac{\partial H_x}{\partial y} - \sigma E_z \right)$$
 (1f)

Yee [1] originally introducted a set of finite-difference equations for the system of Equations (la) - (lf). Following Yee's notation, we denote a space point in a cubic lattice as

$$(i,j,k) = (i\delta,j\delta,k\delta)$$
 (2)

and any function of space and time as

$$F^{n}(i,j,k) = F(i\delta,j\delta,k\delta,n\delta t), \qquad (3)$$

where $\delta = \delta x = \delta y = \delta z$ is the space increment, δt is the time increment, and i, j, k, and n are integers. Yee used centered finite-difference expressions for the space and time derivatives that are both simply programmed and second-order accurate in δ and in δt , respectively:

$$\frac{\partial F^{n}(i,j,k)}{\partial x} = \frac{F^{n}(i+\frac{1}{2},j,k) - F^{n}(i-\frac{1}{2},j,k)}{\delta} + O(\delta^{2})$$
 (4)

$$\frac{\partial F^{n}(i,j,k)}{\partial t} = \frac{\int_{0}^{n+\frac{1}{2}} \int_{0}^{n-\frac{1}{2}} \int$$

To achieve the accuracy of Equation (4), and to realize all of the space derivatives of Equations (la) - (lf), Yee positioned the components of \overline{E} and \overline{H} about a unit cell of the lattice as shown in Figure 1. To achieve the accuracy of Equation (5), he evaluated \overline{E} and \overline{H} at alternate half time steps. The result of these assumptions is the following general system of finite-difference equations for the system of Equations (la) - (lf):

$$\frac{n+\frac{1}{2}}{H_{X}(i,j+\frac{1}{2},k+\frac{1}{2})} = H_{X}(i,j+\frac{1}{2},k+\frac{1}{2}) + \frac{n}{X}(i,j+\frac{1}{2},k+\frac{1}{2}) + \frac{n}{X}(i,j+\frac{1}{2},$$

$$\frac{n+\frac{1}{2}}{H_{y}(i+\frac{1}{2},j,k+\frac{1}{2})} = H_{y}^{n-\frac{1}{2}} + H_{y}^{n}(i+\frac{1}{2},j,k+\frac{1}{2}) + \frac{n}{2}$$

$$\frac{\delta t}{\mu(i+\frac{1}{2},j,k+\frac{1}{2})\delta} \begin{bmatrix} n & n \\ E_{z}(i+1,j,k+\frac{1}{2}) - E_{z}(i,j,k+\frac{1}{2}) + E_{z}(i+\frac{1}{2},j,k+\frac{1}{2}) \\ n & E_{x}(i+\frac{1}{2},j,k) - E_{x}(i+\frac{1}{2},j,k+\frac{1}{2}) \end{bmatrix}$$
(6b)

$$H_{Z}^{n+\frac{1}{2}}H_{Z}^{n-\frac{1}{2}}H_{Z$$

$$\frac{n+1}{E_{y}(i,j+\frac{1}{2},k)} = \frac{\left[1 - \frac{\sigma(i,j+\frac{1}{2},k)\delta t}{2\varepsilon(i,j+\frac{1}{2},k)}\right]}{\left[1 + \frac{\sigma(i,j+\frac{1}{2},k)\delta t}{2\varepsilon(i,j+\frac{1}{2},k)}\right]} \cdot \frac{n}{E_{y}(i,j+\frac{1}{2},k)} + \frac{\sigma(i,j+\frac{1}{2},k)\delta t}{2\varepsilon(i,j+\frac{1}{2},k)\delta t} \\
\frac{\delta t}{\varepsilon(i,j+\frac{1}{2},k)\delta} \cdot \frac{1}{\left[1 + \frac{\sigma(i,j+\frac{1}{2},k)\delta t}{2\varepsilon(i,j+\frac{1}{2},k)}\right]} \cdot \frac{n+\frac{1}{2}}{H_{x}(i,j+\frac{1}{2},k+\frac{1}{2})} - H_{x}(i,j+\frac{1}{2},k-\frac{1}{2})} + \frac{n+\frac{1}{2}}{H_{x}(i,j+\frac{1}{2},k)} \\
\frac{n+1}{E_{z}(i,j,k+\frac{1}{2})} = \frac{\left[1 - \frac{\sigma(i,j,k+\frac{1}{2})\delta t}{2\varepsilon(i,j,k+\frac{1}{2})}\right]}{\left[1 + \frac{\sigma(i,j,k+\frac{1}{2})\delta t}{2\varepsilon(i,j,k+\frac{1}{2})}\right]} \cdot \frac{n}{E_{z}(i,j,k+\frac{1}{2})} + \frac{n}{E_{z}(i,j,k+\frac{1}{2})} + \frac{n+\frac{1}{2}}{H_{y}(i+\frac{1}{2},j,k+\frac{1}{2})} + \frac{n+\frac{1}{2}}{H_{y}(i,j+\frac{1}{2},k+\frac{1}{2})} + \frac{n+\frac{1}{2}}{H_{y}(i,j+\frac{1}{2},k+\frac{1}{2}$$

With the system of Equations (6a) - (6f), the new value of a field vector component at any lattice point depends only on its previous value and on the previous values of the components of the other field vector at adjacent points. Therefore, at any given time step, the computation of a field vector may proceed one point at a time.

Many electromagnetic interaction problems involve nonpermeable media and can be approached using a fixed time step and space increment. For such problems (including the cylinder and nose cone geometries specified for this research effort), the quantity $\delta t/\mu(i,j,k)\delta$ is constant for all (i,j,k) of the lattice, and the Yee system of Equations (6a) - (6f) can be simplified to reduce computer running time in the following manner. We define the constants:

$$R = \delta t/2\epsilon_{a} \tag{7a}$$

$$R_a = \delta t^2 / (\delta^2 \mu_0 \epsilon_0) \tag{7b}$$

$$R_{b} = \delta t/\mu_{0} \delta \tag{7c}$$

$$C_{\mathbf{a}}(m) = \frac{1 - R\sigma(m)/\varepsilon_{\mathbf{r}}(m)}{1 + R\sigma(m)/\varepsilon_{\mathbf{r}}(m)}$$
(7d)

$$C_{b}(m) = \frac{R_{a}}{\varepsilon_{r}(m) + R\sigma(m)}$$
 (7e)

where m is an integer denoting a particular dielectric or conducting medium in the space to be modeled. We also define the proportional electric-field vector

$$\tilde{E} = R_b \tilde{E}$$
 (8)

Using the definitions of Equations (7a) - (7e) and (8), we rewrite Equations (6a) - (6c) as:

$$\begin{array}{ll} n+\frac{1}{2} & n-\frac{1}{2} \\ H_{\chi}(i,j+\frac{1}{2},k+\frac{1}{2}) &= H_{\chi}(i,j+\frac{1}{2},k+\frac{1}{2}) + \widetilde{E}_{y}(i,j+\frac{1}{2},k+1) - \widetilde{E}_{y}(i,j+\frac{1}{2},k) + \\ & \widetilde{E}_{z}(i,j,k+\frac{1}{2}) - \widetilde{E}_{z}(i,j+1,k+\frac{1}{2}) \end{array} \tag{9a}$$

$$\begin{array}{rcl} n+\frac{1}{2} & n-\frac{1}{2} & n \\ H_{Z}(i+\frac{1}{2},j+\frac{1}{2},k) & = & H_{Z}(i+\frac{1}{2},j+\frac{1}{2},k) & + & \widetilde{E}_{X}(i+\frac{1}{2},j+\frac{1}{2},k) & - & \widetilde{E}_{X}(i+\frac{1}{2},j+\frac{1}{2},k) & + \\ & & \widetilde{E}_{y}(i,j+\frac{1}{2},k) & - & \widetilde{E}_{y}(i+\frac{1}{2},j+\frac{1}{2},k) & \end{array}$$

This modification eliminates the three multiplications needed by Yee in the $\bar{\rm H}$ part of the algorithm. Further, we rewrite Equations (6d) - (6f) as:

$$m = MEDIA(i+\frac{1}{2},j,k)$$

$$\tilde{E}_{x}(i+\frac{1}{2},j,k) = C_{a}(m)\tilde{E}_{x}(i+\frac{1}{2},j,k) + C_{b}(m)[H_{z}(i+\frac{1}{2},j+\frac{1}{2},k) - H_{z}(i+\frac{1}{2},j-\frac{1}{2},k) + C_{b}(m)[H_{z}(i+\frac{1}{2},j+\frac{1}{2},k) - H_{z}(i+\frac{1}{2},j-\frac{1}{2},k) + C_{b}(m)[H_{z}(i+\frac{1}{2},j+\frac{1}{2},k) - H_{z}(i+\frac{1}{2},j+\frac{1}{2},k) - H_{z}(i+\frac{1}{2},j+\frac{1}{2},k)]$$
(9d)
$$H_{y}(i+\frac{1}{2},j,k-\frac{1}{2}) - H_{y}(i+\frac{1}{2},j,k+\frac{1}{2})]$$

$$m = MEDIA(i,j+\frac{1}{2},k)$$

$$m = MEDIA(i,j,k+\frac{1}{2})$$

$$\begin{array}{lll} \tilde{E}_{z}(i,j,k+\frac{1}{2}) & = & C_{a}(m)\tilde{E}_{z}(i,j,k+\frac{1}{2}) + & C_{b}(m)[H_{y}(i+\frac{1}{2},j,k+\frac{1}{2}) - & H_{y}(i-\frac{1}{2},j,k+\frac{1}{2}) + \\ & & & n+\frac{1}{2} & n+\frac{1}{2} \\ & & & H_{x}(i,j-\frac{1}{2},k+\frac{1}{2}) - & H_{x}(i,j+\frac{1}{2},k+\frac{1}{2})] \end{array}$$

This modification eliminates the need for computer storage of separate ϵ and σ arrays. Now, only a MEDIA array which specifies the type-integer of the dielectric or conducting medium at the location of each electric field component in the lattice need be stored. In addition, the $\epsilon_{\mathbf{r}}$ and σ of each medium can now be changed without having to re-punch a large data card deck, if the basic structure geometry is unchanged. Such a change involves only the recalculation of the few values of $C_{\mathbf{a}}(\mathbf{m})$ and $C_{\mathbf{b}}(\mathbf{m})$.

2.2.2 Choice of Space and Time Increments

The choice of δ and δ t is motivated by the reasons of accuracy and algorithm stability, respectively. To insure the accuracy of the computed spatial derivatives of the electromagnetic fields, δ must be small compared to a wavelength (usually $\leq \lambda/10$). Further, to insure that the cubic lattice approximation to the surfaces of the structure modeled is not too coarse, δ must be small compared to the overall dimensions of the structure.

To insure the stability of the time-stepping algorithm of Equations (9a) - (9f), δt is chosen to satisfy the inequality

$$\delta t \leq \left(\frac{1}{\delta x^2} + \frac{1}{\delta y^2} + \frac{1}{\delta z^2}\right)^{-\frac{1}{2}} c_{\text{max}}^{-1}$$

$$\leq \frac{\delta}{c_{\text{max}}\sqrt{3}} \text{ (for a cubic lattice)}$$
(10)

where c_{max} is the maximum wave phase velocity within the model. The corresponding stability criterion set forth by Yee in Equations (7) and (8) of his paper is incorrect. The derivation of Equation (10) was outlined in Section 3.4.2 of Reference 8.

2.2.3 Lattice Truncation Conditions

A basic consideration with the FD-TD lattice is the treatment of the field vector components at the lattice truncation planes. Inspection of Equations (9a) - (9f) indicates that the values of such components cannot be determined from the system of finite-difference equations because of the centered nature of the spatial derivatives. Therefore, these values must be

computed using an auxiliary truncation condition. However, great care must be taken because this condition must not cause the spurious reflection of waves scattered outward from the structure modeled, as observed by Yee. The goal of formulating the truncation condition is to make the lattice truncation planes invisible to all possible waves propagating within the lattice, as shown in Figure 2.

A desirable truncation condition relates in a simple way the values of the field components at the truncation planes to field component values at points one or more δ within the lattice. We now consider examples of such a truncation for cases of FD-TD lattices in one and three dimensions.

One-Dimensional Case

For simplicity, we consider waves having only the E_z and H_x components and propagating in the $\pm y$ directions. The one-dimensional FD-TD lattice is simply a y-directed line of points having the E_z and H_x components interleaved and separated from each other by 0.5 δy . The lattice is assumed to extend from an E_z component at point y=0 to another E_z component at point $y=J\delta y$. A time step of $\delta t=\delta y/c$ is used; a value which is the maximum allowed by the stability condition of Equation (10) for this lattice ($\delta x=\delta z=\infty$).

Subject to these assumptions, the truncation condition at point y = 0,

$$\widetilde{E}_{z}^{n}(0) = \widetilde{E}_{z}^{n-1}(1) \tag{11a}$$

simulates the free space propagation of the magnitude of \tilde{E}_z from the point "1" to the truncation point "0" in one time step (the free-space propagation delay implied by the time-step relation). This is an exact truncation for this lattice in that all possible -y-directed waves are absorbed at 0 without reflection. If we wish to simulate the truncation of the lattice at point $y = J\delta$, the truncation condition

$$\widetilde{E}_{z}^{n} (J) = \widetilde{E}_{z}^{n-1} (J-1)$$
 (11b)

is exact for all possible +y-directed waves at this point.

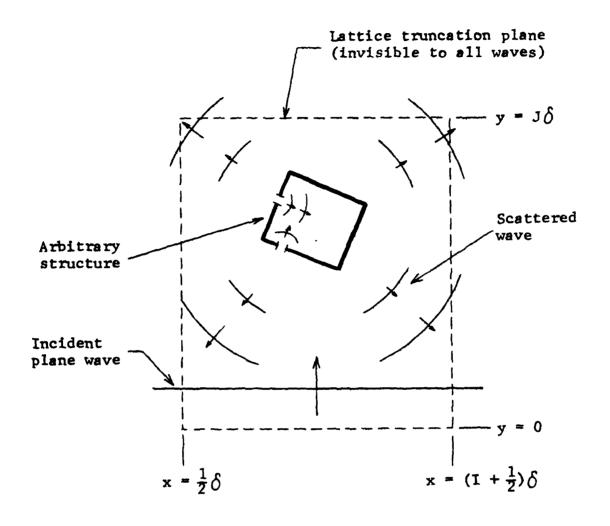


Fig. 2 IDEAL FD-TD LATTICE TRUNCATION CONDITIONS

Three-Dimensional Case

Here, we consider waves having all six field components and propagating in all possible directions. The lattice is assumed to extend from:

```
H_y and H_z components at x = \frac{1}{2}\delta to H_y and H_z components at x = (I + \frac{1}{2})\delta; E_x and E_z components at y = 0 to E_x and E_z components at y = J\delta; E_x and E_y components at z = 0 to E_x and E_y components at z = K\delta.
```

A time step of $\delta t = \delta/2c$ is used, a value which is about 13% lower than the maximum allowed ($\delta t = \delta/\sqrt{3} c$) by the stability condition of Equation (10) for this lattice ($\delta x = \delta y = \delta z = \delta$).

No simple, exact truncation condition, analogous to Equations (11a) and (11b), is apparent for this three-dimensional space lattice. This is because we cannot assume the outgoing waves to be plane and normally incident on one lattice boundary. At any truncation point, the local angle of incidence of these waves relative to the truncation plane is unknown. Further, several different waves having different local angles of incidence may arrive at the same time. No simple truncation condition can account for all of these possibilities. Therefore, we can arrive at only an approximate condiction that reduces the effective lattice boundary reflection coefficient to an acceptable level.

A set of simple, approximate truncation conditions that has been used with good results [8] is as follows.

$$\frac{\text{At } x = \frac{1}{2} \delta:}{n} = \frac{n-2}{H_y(\frac{1}{2}, j, k+\frac{1}{2})} = \frac{n-2}{H_y(\frac{1}{2}, j, k+\frac{1}{2})} + \frac{n-2}{H_y(\frac{1}{2}, j+\frac{1}{2}, k)} + \frac{n-2}{H_y(\frac{1}{2}, j+\frac{1}{2}, k)} + \frac{n-2}{H_y(\frac{1}{2}, j+\frac{1}{2}, k)} = \frac{n-2}{H_z(\frac{1}{2}, j+\frac{1}{2}, k)} + \frac{n-2}{H_z(\frac{1}$$

$$\frac{\text{At } x = (I + \frac{1}{2}) \delta}{n}: \frac{n-2}{n} = \frac{n-2}{H_y(I + \frac{1}{2}, j, k + \frac{1}{2})} = \frac{n-2}{H_y(I - \frac{1}{2}, j, k + \frac{1}{2})} + \frac{n-2}{H_y(I - \frac{1}{2}, j, k + \frac{1}{2})} + \frac{n-2}{H_y(I - \frac{1}{2}, j, k + \frac{1}{2})} + \frac{n-2}{H_y(I - \frac{1}{2}, j, k + \frac{1}{2})}$$

At y = 0:

$$\tilde{E}_{x}^{n}(i+\frac{1}{2},0,k) = \tilde{E}_{x}^{n-2}(i+\frac{1}{2},1,k)$$
(13a)

$$\tilde{E}_{2}^{n}(i,0,k+\frac{1}{2}) = \tilde{E}_{2}^{n-2}(i,1,k+\frac{1}{2})$$
(13b)

At $y = J \delta$:

$$\tilde{E}_{x}(i+\frac{1}{2},J,k) = \tilde{E}_{x}(i+\frac{1}{2},J-1,k)$$
 (13c)

$$\tilde{E}_{z}^{n}(i,J,k+\frac{1}{2}) = \tilde{E}_{z}^{n-2}(i,J-1,k+\frac{1}{2})$$
 (13d)

At z = 0:

$$\tilde{E}_{\chi}^{n}(i+\frac{1}{2},j,0) = [\tilde{E}_{\chi}^{n-2}(i-\frac{1}{2},j,1) + \tilde{E}_{\chi}^{n-2}(i+\frac{1}{2},j,1) + \tilde{E}_{\chi}^{n-2}(i+3/2,j,1)]/3$$
(14a)

$$\tilde{E}_{y}^{n}(i,j+\frac{1}{2},0) = [\tilde{E}_{y}^{n-2}(i-1,j+\frac{1}{2},1) + \tilde{E}_{y}^{n-2}(i,j+\frac{1}{2},1) + \tilde{E}_{y}^{n-2}(i+1,j+\frac{1}{2},1)]/3$$
(14b)

$$\frac{At \ z = K \ \delta}{n} = \prod_{\substack{n=2 \\ X \ (i+\frac{1}{2},j,K)}}^{n-2} = \left[\tilde{E}_{X} \ (i-\frac{1}{2},j,K-1) + \tilde{E}_{X} \ (i+\frac{1}{2},j,K-1) + \tilde{E}_{X} \ (i+\frac{1}{2},j,K-1)\right]/3}$$

$$\tilde{E}_{y} (i,j+\frac{1}{2},K) = \left[\tilde{E}_{y} \ (i-1,j+\frac{1}{2},K-1) + \tilde{E}_{y} \ (i,j+\frac{1}{2},K-1) + \tilde{E}_{y} \ (i+\frac{1}{2},j+\frac{1}{2},K-1)\right]/3}$$

Equations (12) - (14) allow the field value at any truncation point to rise to approach the field value of any outgoing wave, thus lowering the effective truncation plane reflection coefficient. This is done by modeling the propagation of an outgoing wave from the lattice plane adjacent to the truncation, in two time steps (the free-space propagation delay implied by the time-step relation). The averaging process is used to take into account the possible local angles of incidence of the outgoing wave at the truncation and possible multiple incidences.

Truncation conditions (12) - (14) are useful for an assumed +y-directed incident plane wave with field components E_z and H_x . For such a wave, Equation (13) represents exact truncations similar to Equation (11). In addition, Equations (12) and (14) have no effect on the propagation of such a wave, which lacks H_y , H_z , E_x , and E_y . Thus, this set of truncation conditions effectively makes the lattice boundary planes invisible to a +y-directed incident plane wave.

Use of Exterior-Region Anisotropy

One way of reducing spurious reflections at the lattice truncations is to introduce an anisotropic lossy medium outside of the modeled structure. Properly constituted, the medium would attenuate field components present only in the scattered wave, leaving the incident plane wave unaffected. For the three-dimensional case, this can be easily done by specifying an anisotropic conductivity, $\sigma_{\rm ext}$, in the free-space region exterior to the structure. Equation (9f), the finite-difference equation for \tilde{E}_z , requires $\sigma_{\rm ext}$ = 0 to insure that the incident wave is not attenuated. However, we may assume a small value of $\sigma_{\rm ext}$ for Equations (9d) and (9e), the finite-difference equations for \tilde{E}_x and \tilde{E}_y , without affecting the propagation of the incident wave or the penetrating wave within the structure. This assumption results in attenuation of the \tilde{E}_x and \tilde{E}_y components of the exterior diffracted wave, and thus, reduces z-directed wave reflections at the lattice truncations.

Effect on Algorithm Stability

The stability condition of Equation (10) is valid for the Yee, or null choice, of lattice truncation conditions. This is because Yee's set of truncation conditions causes total reflection of all lattice wave modes at the surface planes of the lattice, and thus, introduces no new wave modes. However, introduction of Equations (12) - (14) to the three-dimensional algorithm is found to increase the strictness of the stability condition. For the three-dimensional case, some care must be taken to avoid algorithm instability.

The nature of the instability of the three-dimensional algorithm is of importance. First, it is late in appearance, requiring more than five-hundred time steps for a 2×10^4 - cell lattice, and more than one-thousand time steps for a 6×10^4 - cell lattice. Second, its initial visibility is delayed by either increasing the size of the lattice, or by increasing the losses of the dielectric media of the lattice. This suggests the importance of wave propagation effects in the growth of the instability.

There are two likely solutions to the problem of algorithm instability. First, δt can be reduced. This, however, would complicate the programming of the truncation conditions because a wave would no longer propagate across a free-space unit cell of the lattice in an integral number of time steps.

The second solution is much simpler since it does not require programming for interpolating field values at the truncation planes between time steps. This solution is merely to set a lower bound of about 10^5 cells on the size of the FD-TD lattice used, thus delaying the onset of the instability for several thousand time steps. In most cases, such a delay would be sufficient for the computed solution to reach the sinusoidal steady state. For many problems, the use of 10^5 - cell lattice is not at all extravagant and allows the problem of algorithm instability to be essentially forgotten. The computer runs in RADC Contract F30602-77-C-0163 for the cylinder and the missile nose cone employed this solution. They used, respectively, 94,000 cells -- 800 time steps and 58,000 cells -- 900 time steps, without any apparent instability of the computed solution.

2.2.4 Plane Wave Source Condition

Another basic consideration with the FD-TD method is the simulation of the continuous, sinusoidal, incident plane wave. Yee specified the shape and direction of propagation of an incident wave pulse by inserting all of its field values as initial conditions over a portion of the lattice. However, the Yee approach is clearly inadequate for a continuous wave train because a very elongated lattice would be needed to contain the wave as an initial condition, wasting much computer storage.

In this subsection, we discuss the simulation of an incident, +y-directed plane wave using a source condition localized at only one lattice plane, and invisible to all scattered waves propagating within the lattice. This allows a compact lattice and maximum utilization of the available computer storage.

The most simple approach to this problem is to vary the electric field at all points along the lattice plane y = 0 in a sinusoidal manner. This plane would then radiate the desired plane wave. However, such a specification of field values at a lattice truncation plane, without consideration of the values of the fields of any possible outgoing, scattered waves, would cause undesired wave reflections.

A more desirable plane wave source condition would take into account the scattered fields at the source plane. For the three-dimensional case, a useful wave source condition at plane $y=j_{s}\delta$ (near y=0) is as follows:

$$E_{z}^{(i,j_{s},k+\frac{1}{2})} \leftarrow R_{b} \sin(2\pi f n \delta t) + E_{z}^{(i,j_{s},k+\frac{1}{2})}$$
 (15)

where f is the irradiation frequency and R_b is defined by Equation (7c). Equation (15) is a modification of the Maxwell's equations algorithm for all points on the lattice plane $y = j_s \delta$. At each point on this source plane, the computer first calculates \tilde{E}_z^n in the normal manner of the alogrithm, and stores the value in memory. Then, the value of the sinusoid is calculated and added to the stored value of \tilde{E}_z^n . Finally, this modified value of \tilde{E}_z^n is stored in memory. In effect, Equation (15) simulates the linear superposition of a +y-directed plane wave and the ambient field along the source plane. This

condition permits any scattered, outgoing wave to propagate right through the wave source plane without reflection, and reach the lattice truncation at y = 0 to be absorbed.

2.2.5 Symmetry Conditions

An important savings of computer memory and program execution time results if even symmetry of the modeled structure about one or two lattice planes can be assumed. In this subsection, we discuss the programming of this symmetry for the three-dimensional case.

For the three-dimensional case, the modeled structure is assumed to be evenly symmetric about lattice planes $x = (\overline{1} + \frac{1}{2})\delta$ and $z = \overline{K}\delta$:

$$\varepsilon, \sigma(I+\frac{1}{2}+h,j,k) = \varepsilon, \sigma(\overline{I}+\frac{1}{2}-h,j,k), \quad \mu = \mu_0$$
 (16a)

$$\varepsilon, \sigma(i,j,\overline{K}+h) = \varepsilon, \sigma(i,j,\overline{K}-h)$$
 (16b)

The incident radiation is assumed to be a +y-directed plane wave, with the field components E_Z and H_X naturally having even symmetry about any lattice plane x = constant or z = constant. Therefore, we conclude that the E_Z and H_X components of the total field possess even symmetry about the lattice planes $x = (\overline{I} + \frac{I_2}{2})\delta$ and $z = \overline{K}\delta$:

$$\tilde{E}_{2}^{n}(\overline{1+\frac{1}{2}}+h,j,k+\frac{1}{2}) = \tilde{E}_{2}(\overline{1+\frac{1}{2}}-h,j,k+\frac{1}{2})$$
(17a)

$$n+\frac{1}{2}$$
 H_{X} $(\overline{1}+\frac{1}{2}+h,j+\frac{1}{2},k+\frac{1}{2}) = H_{X}$ $(\overline{1}+\frac{1}{2}-h,j+\frac{1}{2},k+\frac{1}{2})$ (17b)

$$\tilde{E}_{z}^{n}(i,j,\overline{K}+h) = \tilde{E}_{z}^{n}(i,j,\overline{K}-h)$$
 (17c)

$$H_{X}^{n+\frac{1}{2}} = H_{X}^{n+\frac{1}{2}}, \overline{K}+h) = H_{X}^{n+\frac{1}{2}}, \overline{K}-h)$$
(17d)

To develop a convenient set of symmetry conditions, we follow a procedure that has been detailed in Section 3.4.5 of Reference 8. This results in

$$\begin{array}{lll}
 & n+\frac{1}{2} & n+\frac{1}{2} \\
 & (\overline{1}+\frac{1}{2},j,k) &= & H_y(\overline{1}+\frac{1}{2},j,k+\frac{1}{2}) &= & H_z(\overline{1}+\frac{1}{2},j+\frac{1}{2},k) &= & 0 \text{ for all } n; \\
 & (18a)
\end{array}$$

$$\begin{array}{lll}
 & \begin{array}{lll}
 & \begin{array}{lll}
 & & \\
 & & \\
 & & \\
 & & \\
 & & \\
 & & \\
 & & \\
 & & \\
 & & \\
 & & \\
 & & \\
 & & \\
 & & \\
 & & \\
 & & \\
 & & \\
 & & \\
 & & \\
 & & \\
 & & \\
 & & \\
 & & \\
 & & \\
 & & \\
 & & \\
 & & \\
 & & \\
 & & \\
 & & \\
 & & \\
 & & \\
 & & \\
 & & \\
 & & \\
 & & \\
 & & \\
 & & \\
 & & \\
 & & \\
 & & \\
 & & \\
 & & \\
 & & \\
 & & \\
 & & \\
 & & \\
 & & \\
 & & \\
 & & \\
 & & \\
 & & \\
 & & \\
 & & \\
 & & \\
 & & \\
 & & \\
 & & \\
 & & \\
 & & \\
 & & \\
 & & \\
 & & \\
 & & \\
 & & \\
 & & \\
 & & \\
 & & \\
 & & \\
 & & \\
 & & \\
 & & \\
 & & \\
 & & \\
 & & \\
 & & \\
 & & \\
 & & \\
 & & \\
 & & \\
 & & \\
 & & \\
 & & \\
 & & \\
 & & \\
 & & \\
 & & \\
 & & \\
 & & \\
 & & \\
 & & \\
 & & \\
 & & \\
 & & \\
 & & \\
 & & \\
 & & \\
 & & \\
 & & \\
 & & \\
 & & \\
 & & \\
 & & \\
 & & \\
 & & \\
 & & \\
 & & \\
 & & \\
 & & \\
 & & \\
 & & \\
 & & \\
 & & \\
 & & \\
 & & \\
 & & \\
 & & \\
 & & \\
 & & \\
 & & \\
 & & \\
 & & \\
 & & \\
 & & \\
 & & \\
 & & \\
 & & \\
 & & \\
 & & \\
 & & \\
 & & \\
 & & \\
 & & \\
 & & \\
 & & \\
 & & \\
 & & \\
 & & \\
 & & \\
 & & \\
 & & \\
 & & \\
 & & \\
 & & \\
 & & \\
 & & \\
 & & \\
 & & \\
 & & \\
 & & \\
 & & \\
 & & \\
 & & \\
 & & \\
 & & \\
 & & \\
 & & \\
 & & \\
 & & \\
 & & \\
 & & \\
 & & \\
 & & \\
 & & \\
 & & \\
 & & \\
 & & \\
 & & \\
 & & \\
 & & \\
 & & \\
 & & \\
 & & \\
 & & \\
 & & \\
 & & \\
 & & \\
 & & \\
 & & \\
 & & \\
 & & \\
 & & \\
 & & \\
 & & \\
 & & \\
 & & \\
 & & \\
 & & \\
 & & \\
 & & \\
 & & \\
 & & \\
 & & \\
 & & \\
 & & \\
 & & \\
 & & \\
 & & \\
 & & \\
 & & \\
 & & \\
 & & \\
 & & \\
 & & \\
 & & \\
 & & \\
 & & \\
 & & \\
 & & \\
 & & \\
 & & \\
 & & \\
 & & \\
 & & \\
 & & \\
 & & \\
 & & \\
 & & \\
 & & \\
 & & \\
 & & \\
 & & \\
 & & \\
 & & \\
 & & \\
 & & \\
 & & \\
 & & \\
 & & \\
 & & \\
 & & \\
 & & \\
 & & \\
 & & \\
 & & \\
 & & \\
 & & \\
 & & \\
 & & \\
 & & \\
 & & \\
 & & \\
 & & \\
 & & \\
 & & \\
 & & \\
 & & \\
 & & \\
 & & \\
 & & \\
 & & \\
 & & \\
 & & \\
 & & \\
 & & \\
 & & \\
 & & \\
 & & \\
 & & \\
 & & \\
 & & \\
 & & \\
 & & \\
 & & \\
 & & \\
 & & \\
 & & \\
 & & \\
 & & \\
 & & \\
 & & \\
 & & \\
 & & \\
 & & \\
 & & \\
 & & \\
 & & \\
 & & \\
 & & \\
 & & \\
 & & \\
 & & \\
 & & \\
 & & \\
 & & \\
 & & \\
 & & \\
 & & \\
 & & \\$$

Equations (18a) and (18b) are sufficient to truncate the FD-TD lattice at planes $x=(\overline{1}+\frac{1}{2})\delta$ and $z=\overline{K}\delta$, respectively, by permitting the calculation of the complete set of field components, with full specification of the assumed even symmetry.

2.3 Initial Evaluation of the FD-TD Method - Results of Previous RADC Contract F30602-77-C-0163

This section first summarizes the results of RADC Contract F30602-77-C-0163 previously carried out to evaluate the suitability of the FD-TD method to determine electromagnetic coupling through an aperture into an enclosed conducting container. This is then followed by a discussion of the basis of the present research to more fully evaluate the FD-TD method.

2.3.1 Objective

The FD-TD method allows, in principle, the computation of the internal EM fields of complex conducting geometries. However, prior to the work on RADC Contract F30602-77-C-0163, this method had not been utilized and evaluated for any conducting geometries. To build up confidence in the FD-TD method for future applications, it was desired to evaluate the usage of the method for certain simple, generic metal structures.

During the research program, two specific metal structures were used in this evaluation: the first, an aluminum cylinder with one open end; the second, the nose cone section of a missile. Each structure was modeled using the FD-TD method to compute the internal EM fields generated by an incident plane wave propagating along the structure axis. The results of the cylinder model were then compared to available theoretical and experimental data.

Final evaluation of the nose cone results will be possible when reliable experimental data for this geometry is obtained in a future research program.

The following describes each coupling-analysis problem considered.

2.3.2 Description of Coupling-Analysis Problems Considered

Task 1: Prediction of the Coupling
Into an Open-Ended Cylinder

The FD-TD technique was employed to solve the following electromagnetic coupling problem:

<u>Interacting structure</u> - Circular (19.0 cm diameter), 68.5 cm long, open-ended aluminum cylinder, as shown in Figure 8 of Final Report RADC-TR-78-142 [Reference 8];

<u>Incident wave</u> - 300 MHz plane wave propagating down the cylinder axis toward its open end;

<u>Desired fields</u> - Each component of total \overline{E} and total \overline{H} in the axial cross-section plane of the cylinder down to 40 cm from the open end. First, with the cross-section plane parallel to the incident \overline{E} , and again with the plane parallel to the incident \overline{H} ;

Resolution - 0.5 cm uniformly throughout the mapping planes;

<u>Plotted values</u> - In decibels relative to an incident \overline{E} of 1 volt/meter and an incident \overline{H} of 1/377 ampere/meter.

To solve this coupling problem, an existing FD-TD computer code was suitably modified to model the cylinder. Details of the model are given in Section 4.3.1 of Reference 8.

Task 2: Prediction of the Coupling Into a Missile Nose Cone

The FD-TD technique was employed to solve the following electromagnetic coupling problem:

<u>Interacting structure</u> - Aluminum nose cone (shown in Figure 9 of Reference 8) with two apertures: a circular one in the nose, and a sleeve fitting located 23-1/3 cm aft. Missile body geometry beyond sleeve fitting assumed to continue to infinity with constant cross-section

shape. Aperture cases investigated:

Trial 1 - Sleeve fitting open, nose aperture closed,

Trial 2 - Both apertures open;

<u>Incident wave</u> - 300 MHz plane wave propagating down the axis of the structure toward its nose aperture;

<u>Desired fields</u> - Each component of total \overline{E} and total \overline{H} in the axial cross-section plane of the nose cone. First, with the cross-section plane parallel to the incident \overline{E} , and again with the plane parallel to the incident \overline{H} ;

Resolution - 1/3 cm uniformly throughout the mapping planes;

<u>Plotted values</u> - In decibels relative to an incident \overline{E} of 1 volt/meter and an incident \overline{H} of 1/377 ampere/meter.

To solve this coupling problem, the computer code of Task 1 was utilized with a new set of data cards specifying the nose cone geometry. Details of the model are given in Section 4.4.1 of Reference 8.

2.3.3 Results and Discussion

Fields computed using the FD-TD technique closely approximated prior experimental and theoretical data (where available) for the cylinder of Task 1. Future work will be required to develop comparative experimental data for the more complex nose cone geometry of Task 2. Details of the results are given in Sections 4.3.3, 4.3.4, and 4.4.2 of Reference 8.

This research program demonstrated that the FD-TD method can be successfully applied to axial-incidence, electromagnetic coupling problems involving highly conducting structures with hole and sleeve-type apertures. Accuracy of the FD-TD results was very good relative to the uncertainties of available experimental and numerical-theory approaches. Convergence of the EM fields to the sinusoidal steady state occurred within about 2 cycles of the incident wave. This resulted in program running times of 3.5 minutes or less on the CDC STAR-100 for 10^5 - cell lattices.

The following questions concerning the FD-TD method remained unanswered at the conclusion of RADC Contract F30602-77-C-0163:

- 1. Can the FD-TD method accurately model EM coupling into a conducting structure for arbitrary angles of incidence and arbitrary wave polarization?
- 2. Can the FD-TD method accurately model a complex structure with both irregular-shaped apertures <u>and</u> dielectric or permeable materials within the interior?
- 3. Can the FD-TD method predict the voltage, current, or power that the coupled field may induce on wires or cable bundles inside of a metal structure?
- 4. What are the size limits of an object that can be modeled using the FD-TD method?
- 5. What is the capability of the FD-TD method to interface with other analysis techniques, such as "Method of Moments"?

These questions should be addressed systematically to permit better definition of the capabilities and limits of the FD-TD technique. Favorable conclusions on most or all of these questions would probably lead to eventual application of the FD-TD method to complex EM coupling problems of interest to RADC and the electromagnetic compatibility community.

The five questions above probe into the nature of the FD-TD modeling method in a fundamental manner. For example, Question 1 involves possibly modeling the longitudinal, resonant currents set up in an elongated metal structure by an incident TM wave. In the time domain, these currents may only slowly converge to the sinusoidal steady state. Answering Question 1 will tell us how much time is needed for convergence, and what measures, if any, can be used to speed convergence without sacrificing accuracy.

Question 2 involves the interaction of conducting and dielectric materials subject to an incident wave. In the time domain, the presence of dielectric materials within a conducting enclosure can modify the convergence of the fields within the enclosure to the sinusoidal steady state. Further, field patterns within the enclosure may be altered significantly by the presence of the dielectric media. Answering Question 2 will tell us the maximum level of complexity that the FD-TD method can attain without sacrificing accuracy, and without having lengthy running times.

Question 3 involves the ability of the FD-TD method to model conducting filaments (wires) instead of sheets. Further, this question will probe the modeling of wire terminations such as resistors, and the ability to translate computed field quantities such as \overline{E} and \overline{H} to circuit quantities such as V, I, and P.

Question 4 involves the interaction between the type of computer being used and the maximum size object that can be modeled using the FD-TD method. Here, considerations such as computer cycle time, computer magnetic-core memory size, computer architecture (pipeline structure, if used; word size; memory paging procedure, etc.), and overall modeling accuracy desired will be considered. This study will tell us if the FD-TD method can be successfully and efficiently adapted to available general purpose computers, in addition to large-scale processors such as the CDC STAR 100.

Lastly, Question 5 involves the feasibility of developing a hybrid approach where some appropriate technique (such as the Method of Moments) is used to develop data for the skin currents or aperture fields of a large structure, and the FD-TD method uses this data to compute the fields penetrating small apertures of the structure into complex interior cavities. In this way, each technique would be applied in the structure-size/complexity range that it is best suited for, allowing an overall solution that is accurate for large, simple structures with small, complex apertures or other fine details. Clearly, adaptation of the amplitude and phase data obtained from a frequency domain method such as MOM will require transformation to the time domain. Further, usage of the transformed data will require modification of the plane wave source condition normally employed for the FD-TD method.

The need to deal with the five questions raised above forms the basis of the research performed under the present contract, F30602-79-C-0039. The following five sections will discuss the results of the present research.

3.0 PROGRAM TASK 1: PREDICTION OF THE COUPLING INTO AN OPEN-ENDED CYLINDER

3.1 Broadside Incidence and Transverse Electric (TE) Wave Polarization

The FD-TD technique was employed to solve the following electromagnetic coupling problem:

<u>Interacting structure</u> - Circular (19.0 cm diameter), 68.5 cm long, open-ended aluminum cylinder as shown in Figures 3 and 4;

<u>Incident wave</u> - 300 MHz plane wave propagating perpendicular to the cylinder axis and polarized so that the wave electric field is perpendicular to the plane formed by the cylinder axis and the incident wavevector;

<u>Desired fields</u> - Each component of total \overline{E} and total \overline{H} in the axial cross-section plane of the cylinder down to 40 cm from the open end. First, with the cross-section plane parallel to the incident \overline{E} , and again with the plane parallel to the incident wavevector;

Resolution - 0.5 cm uniformly throughout the mapping planes;

<u>Plotted values</u> - In decibels relative to an incident \overline{E} of 1 volt/meter and an incident \overline{H} of 1/377 ampere/meter.

To solve this coupling problem, an existing FD-TD computer code was suitably modified to model the cylinder of Figure 3 and 4. The following steps were taken:

- a. A 160 x 63 x 24 cell lattice $(1.45 \cdot 10^6)$ unknown field components) was programmed, with even symmetry of the incident fields and cylinder assumed about lattice plane $z = 24\delta$.
- b. The cylinder geometry of Figures 3 and 4 was mapped into the finite-difference lattice for a unit cell diameter of δ = 0.5 cm.
- c. The FD-TD program was run for this geometry for 800 time steps (equivalent to 2.0 cycles of the incident wave) assuming a slight amount of isotropic loss (σ_{int} = 0.01 mho/m) for the air within the cylinder to increase the rate of convergence to the steady state. 2.5·10⁶ words of memory and 9.4 minutes of central processor time were required on the Control Data STAR-100.

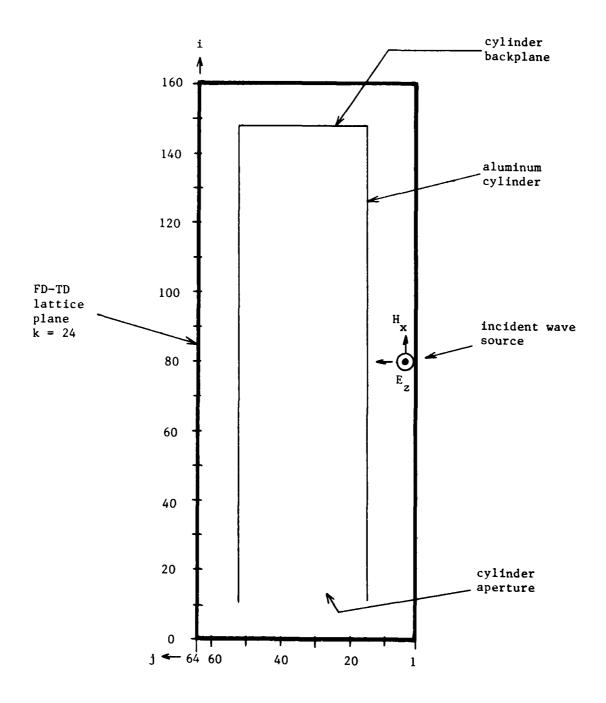


Fig. 3 HORIZONTAL SYMMETRY PLANE VIEW OF

OPEN-ENDED CYLINDER, TE/BROADSIDE CASE

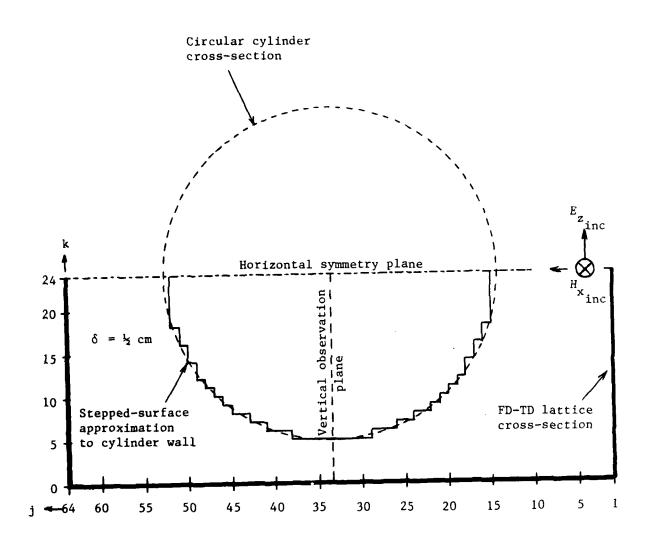


Fig. 4 CROSS-SECTION OF MODEL OF OPEN-ENDED ALUMINUM CYLINDER, TE/BROADSIDE CASE

d. The computed results for \overline{E} and \overline{H} were reduced to contour maps along the horizontal symmetry plane and the vertical observation plane.

Figure 5 plots the computed total electric field, $|E_z/E_{zinc}|$ in decibels along the cylinder axis for the cases n = 200, n = 400, n = 600, and n = 800 time steps. Each curve gives the computed field envelope during the 200 time-step period (0.5 cycle of the incident wave) before the specified value of n. In Figure 5, it should be noted that, at 200 time steps, the incident wave penetrated only about 40 cm into the cylinder, causing the sharp downward break of the n = 200 curve. For all other curves, the incident wave penetrated fully to the cylinder backplane.

Figure 5 indicates the rate of field convergence to the sinusoidal steady state under the condition of finite σ_{int} . Once the wave fields were established throughout the cylinder (curves n = 400, 600, and 800), the principal effect of an added 200 program time steps was the lengthening of the approximately linear decibel slope extending from the aperture, and a consequent deepening of the field null within the cylinder. Noting the break points of the curves from the linear decibel slope, each 200 time-step increase is seen to have lengthened the slope by about 10 cm and decreased the residual internal fields by about 10 dB.

Figure 6 compares the FD-TD computed $|H_X/H_{Xinc}|$ along the cylinder axis with computed results by D. Wilton and A. Glisson using a frequency-domain, body-of-revolution computer program [9]. The FD-TD results, shown as a solid curve, are after 800 time steps. The frequency-domain-program results are graphed as a dashed curve. Excellent agreement (within 0.5 dB) of the results of the two approaches is seen over the first 15 cm of field penetration into the cylinder. Over this span, the total H_X field decay is of the order of 50-55 dB. The rate of decay of H_X computed by either technique equals 3.29 dB/cm, which compares favorably with the 3.46 dB/cm rate predicted by simple waveguide mode theory for this beyond-cutoff case.

Using results of the FD-TD program (800 time steps, $\sigma_{\rm int}$ = 0.01 mho/m), Figures 7-9 graph contour maps of the three computed field components at the cylinder's horizontal symmetry plane. Figures 10 and 11 graph contour maps of the six computed field components at the cylinder's vertical observation

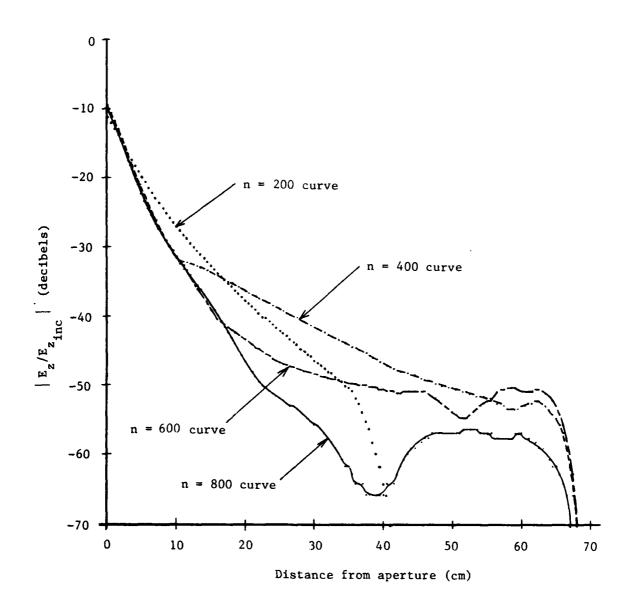


Fig. 5 CONVERGENCE OF THE COMPUTED ELECTRIC FIELD ALONG THE CYLINDER AXIS, TE/BROADSIDE CASE

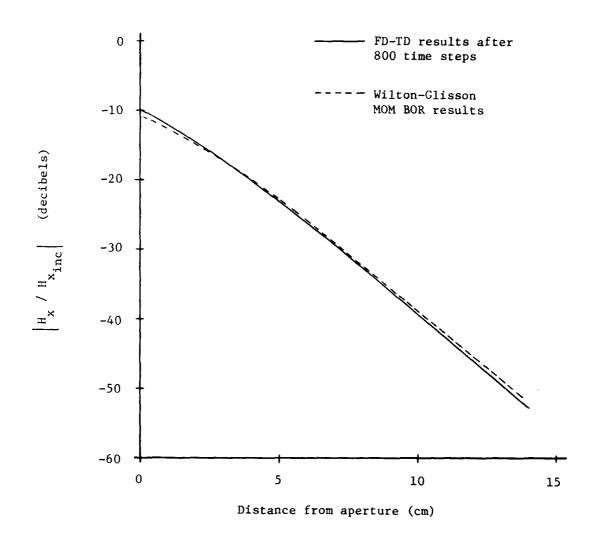


Fig. 6. COMPARISON OF RESULTS FOR THE AXIAL MAGNETIC FIELD WITHIN THE CYLINDER, TE/BROADSIDE CASE

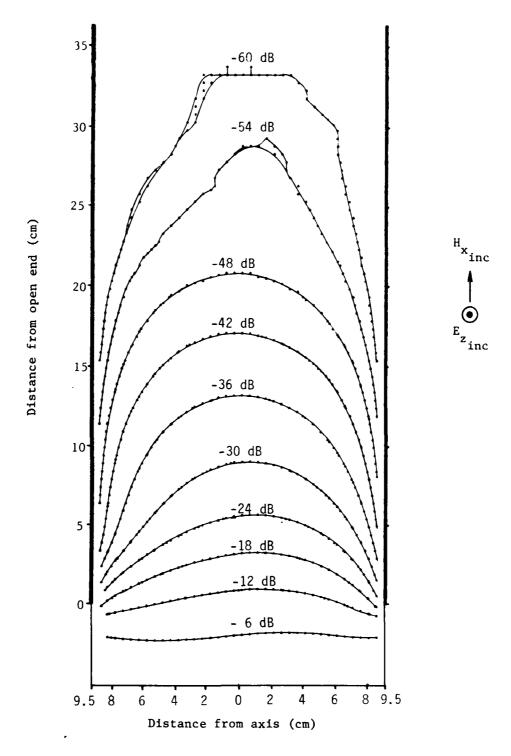


Fig. 7. COMPUTED E_Z CONTOURS IN CYLINDER HOR. SYMMETRY PLANE, TE/BROADSIDE CASE

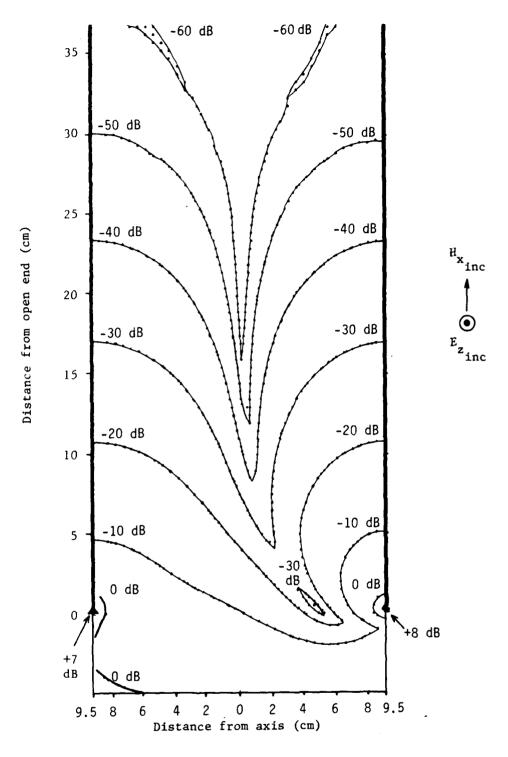


Fig. 8. COMPUTED $H_{\mathbf{x}}$ CONTOURS IN CYLINDER HOR. SYMMETRY PLANE, TE/BROADSIDE CASE

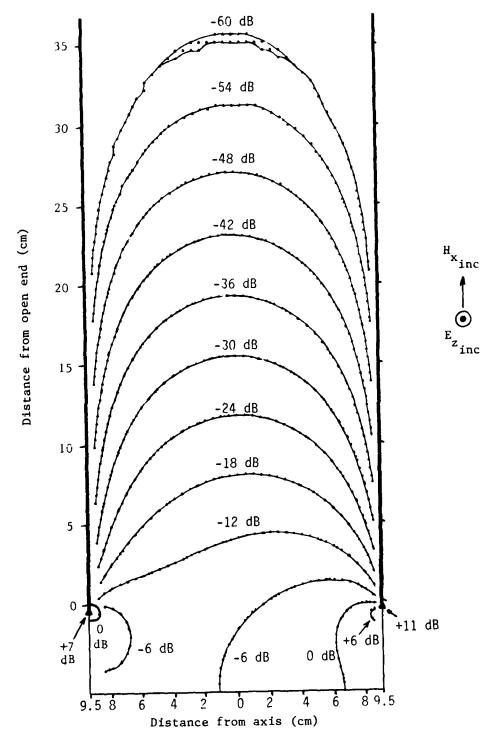


Fig. 9. COMPUTED H_y CONTOURS IN CYLINDER HOR. SYMMETRY PLANE, TE/BROADSIDE CASE

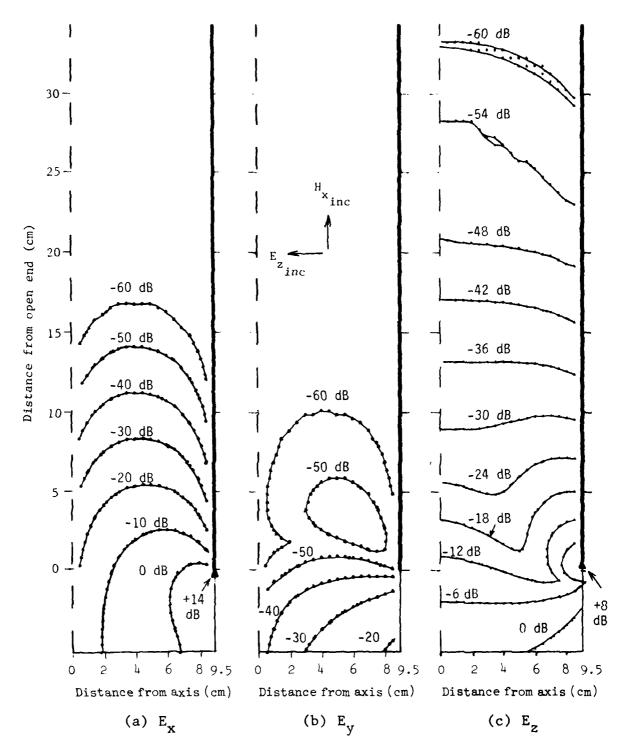


Fig. 10. COMPUTED ELECTRIC FIELD CONTOURS IN THE CYLINDER VERT. OBS. PLANE, TE/BROADSIDE CASE

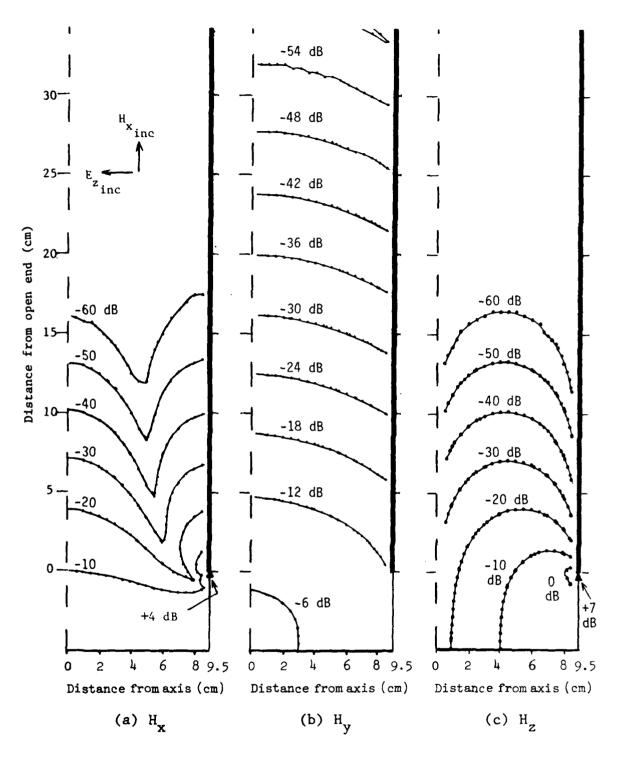


Fig.11. COMPUTED MAGNETIC FIELD CONTOURS IN THE CYLINDER VERT. OBS. PLANE, TE/BROADSIDE CASE

plane. For optimum clarity, contours are plotted at either 6 dB or 10 dB intervals in these figures. Contour points were generated by using a linear interpolation method to determine their locations between adjacent FD-TD field envelope points. Although the lattice cell size, δ , equals 0.5 cm, this interpolation method allows the generation of smooth curves in most cases without a 0.5 cm-period stair-case effect.

3.2 Broadside Incidence and Transverse Magnetic (TM) Wave Polarization

The FD-TD technique was employed to model the same broadside-incidence cylinder problem as that of Section 3.1 and Figures 3 and 4, except that the incident wave polarization was changed to align the wave magnetic field perpendicular to the plane formed by the cylinder axis and the incident wavevector. To solve this coupling problem, the FD-TD computer code of Section 3.1 was modified to accept the polarization change. Further, the code was improved to reduce central processing (CP) time by about 48%. This was accomplished by storing in memory an array of constant coefficients which previously had been re-computed each time step. For example, the TM case required only 4.9 minutes of STAR-100 CP time for 800 time steps of 1.45·10 unknown field components, as compared to 9.4 minutes of CP time for the corresponding TE case of Section 3.1. All FD-TD programs discussed subsequently in this report incorporate the improved code.

Figure 12 plots the FD-TD computed total radial magnetic field, $|H_Z/H_Z|$ (in decibels), along the cylinder axis for the cases n = 200, n = 400, n = 600, and n = 800 time steps. As such, Figure 12 indicates the rate of field convergence to the sinusoidal steady state. Comparing Figure 12 to Figure 5, it is seen that the internal field for the TM case converges more rapidly to the steady state than the field for the TE case. This is a somewhat surprising result since the TM polarization is expected to induce damped, oscillating, longitudinal current flow along the cylinder which might be expected to delay convergence to the steady state. Evidently, the particular cylinder electrical length and effective radiation resistance at 300 MHz combined to cause rapid damping of these oscillating currents, so that the

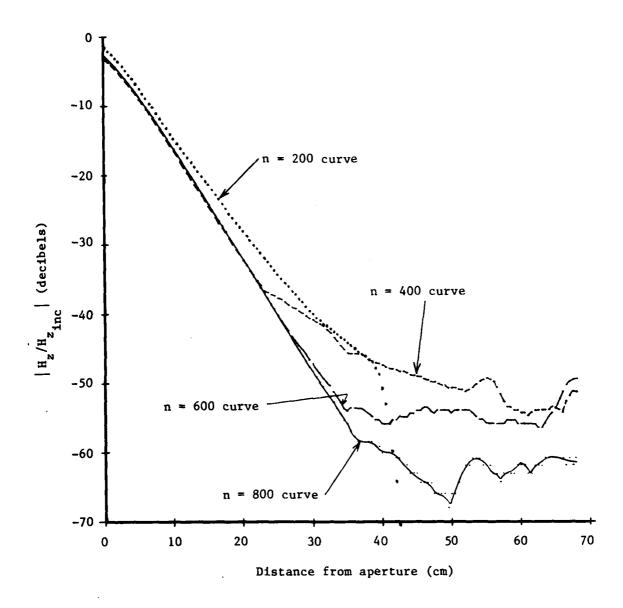


Fig. 12. CONVERGENCE OF THE COMPUTED MAGNETIC FIELD ALONG THE CYLINDER AXIS, TM/BROADSIDE CASE

internal fields could rapidly converge.

Figure 13 compares the FD-TD computed total axial electric field, $|E_{\chi}/E_{\chi}|$, along the cylinder axis with computed results by D. Wilton and A. Glisson using a frequency-domain, moment-method, body-of-revolution computer program [9]. The FD-TD results, shown as a solid curve, are after 800 time steps. The frequency-domain-program results are graphed as a dashed curve. Except near the aperture, good agreement (within 2.5 dB) of the results of the two approaches is seen over the first 25 cm of field penetration into the cylinder. Over this span, the total E_{χ} field decay is of the order of 50-55 dB. The rate of decay of E_{χ} computed by either technique equals 2.13 dB/cm, which is exactly the rate predicted by waveguide mode theory for this beyond-cutoff case.

Using results of the FD-TD program (800 time steps, $\sigma_{\rm int}$ = 0.01 mho/m), Figures 14-16 graph contour maps of the three computed field components at the cylinder's horizontal symmetry plane. Figures 17 and 18 graph contour maps of the six computed field components at the cylinder's vertical observation plane. For optimum clarity, contours are plotted at either 6 dB or 10 dB intervals in these figures.

3.3 Oblique Incidence and Transverse Magnetic (TM) Wave Polarization

As discussed in Section 7.0 of this report, it appears possible to accurately model aperture-excited structures via a hybrid method-of-moments/ FD-TD approach. This hybrid approach has the advantage of allowing arbitrary field excitation without requiring re-programming of the basic geometry of a particular interacting structure. Further, it allows small, highly-complex interior zones of large, simple structures to be analyzed.

As one of the test cases for the hybrid method, it was decided to model the field penetration within the open-ended cylinder of Section 3.1 and 3.2, but assuming that the incident wave propagates at an angle of 45° to the cylinder axis toward the open end. The wave was assumed to be polarized transverse magnetic (TM), i.e., the wave magnetic field was perpendicular to the plane formed by the cylinder axis and the incident wavevector. Results for this case are documented in Section 7.4. These results show a very good agreement between the hybrid method and conventional moment-method results,

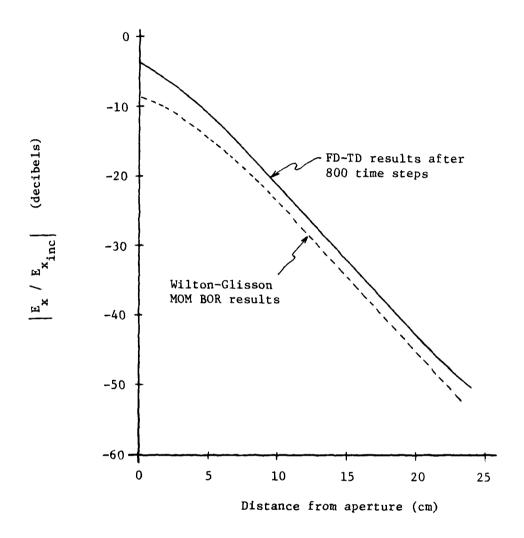


Fig. 13. COMPARISON OF RESULTS FOR THE AXIAL ELECTRIC FIELD WITHIN THE CYLINDER, TM/BROADSIDE CASE

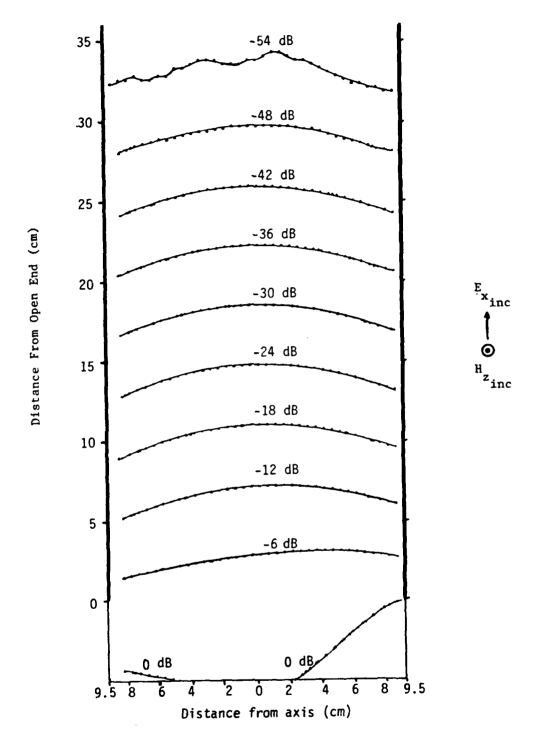


Fig. 14. COMPUTED $H_{\mathbf{Z}}$ CONTOURS IN CYLINDER HOR. SYMMETRY PLANE, TM/BROADSIDE CASE

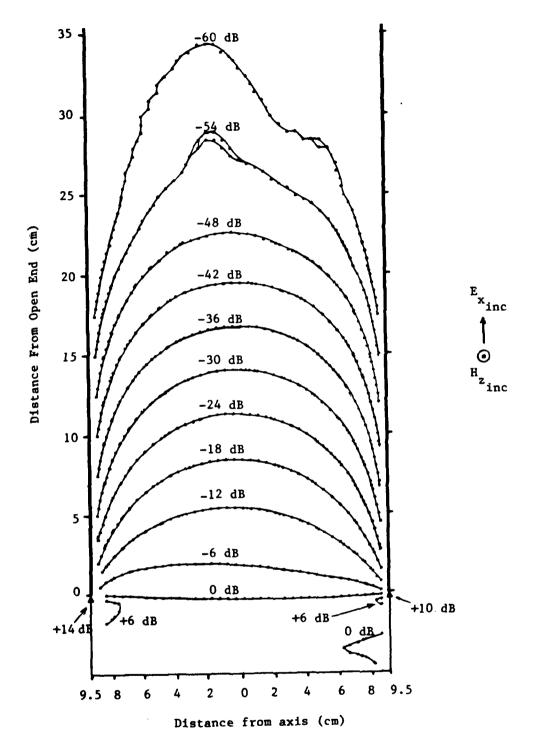


Fig.15. COMPUTED $E_{\mathbf{x}}$ CONTOURS IN CYLINDER HOR. SYMMETRY PLANE, TM/BROADSIDE CASE

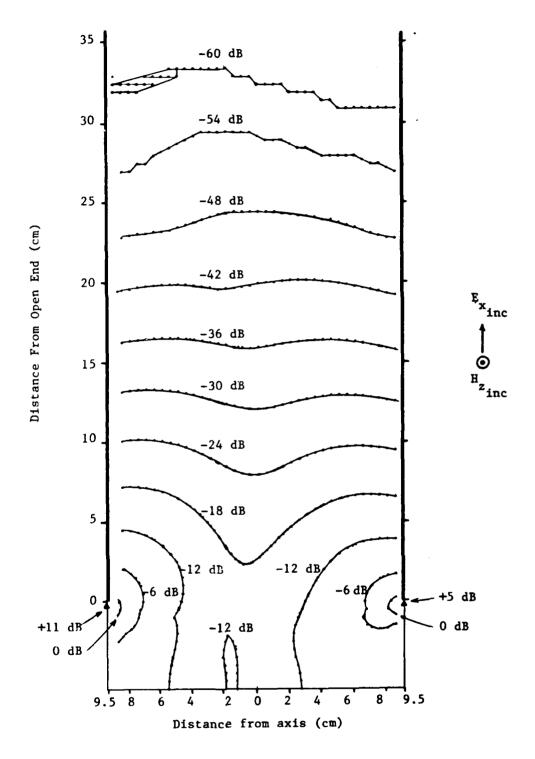


Fig. 16. COMPUTED E CONTOURS IN CYLINDER HOR. SYMMETRY PLANE, TM/BROADSIDE CASE

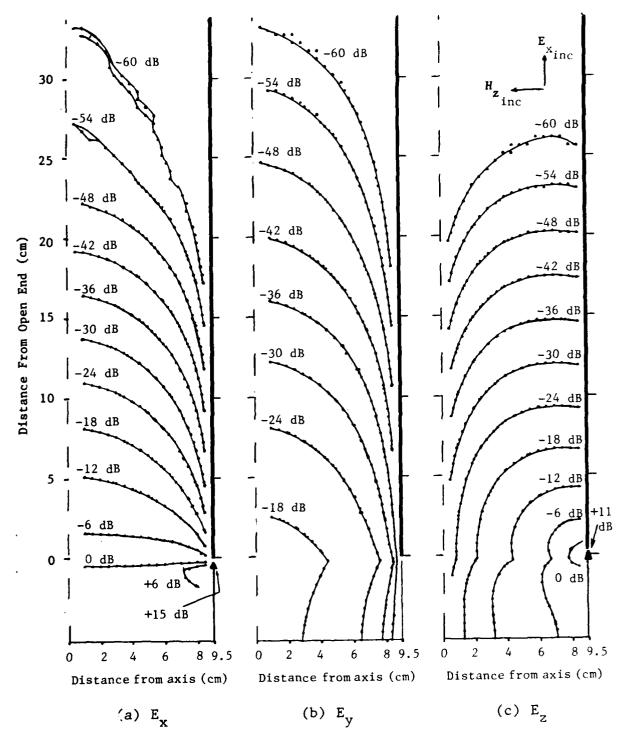


Fig. 17. COMPUTED ELECTRIC FIELD CONTOURS IN THE CYLINDER VERT. OBS. PLANE, TM/BROADSIDE CASE

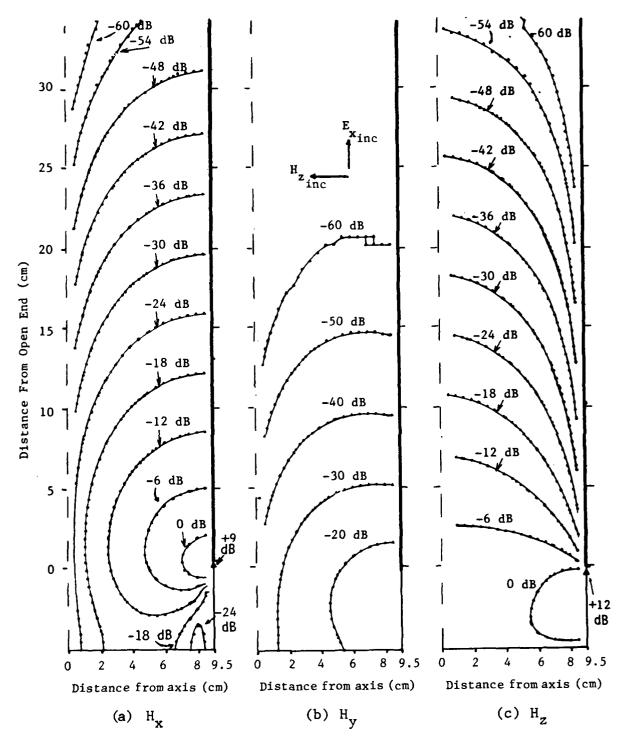


Fig. 13. COMPUTED MAGNETIC FIELD CONTOURS IN THE CYLINDER VERT. OBS. PLANE, TM/BROADSIDE CASE

indicating the feasibility of modeling structures for arbitrary angles of wave incidence.

3.4 Conclusions

Completion of Program Task 1 demonstrates the capability of the FD-TD method to accurately model the electromagnetic fields coupled into a structure which is illuminated with an electromagnetic plane wave having an arbitrary polarization. Elements of Task 5 will demonstrate this modeling capability for an arbitrary wave angle of incidence, as well.

4.0 PROGRAM TASK 2: PREDICTION OF THE COUPLING INTO A MISSILE GUIDANCE SECTION

4.1 Model 1 - Includes the Interior Dielectric Material

The FD-TD technique was employed to solve the following electromagnetic coupling problem:

<u>Interacting structure</u> - Empty shell of missile guidance section, shown in Figures 19-21, with two apertures: a circular one in the nose, and a sleeve fitting located 23-1/3 cm aft. Missile body geometry beyond sleeve fitting assumed to continue to infinity with constant cross-section shape. Dielectric materials are located as shown in Figures 19 and 20. Assumed electrical parameters for the media comprising the model:

Medium	Rel. Permittivity, ε'r	Conductivity, σ (mhos/m)	
Aluminum	1.0	3.7 ⋅10 ⁷	
Fiberglas	5.5	2.4 · 10 ⁻³	
Phenolic	4.5	8.0 · 10 ⁻⁴	
Magnesium fluoride	5.3	0.0	

For the fiberglas, phenolic, and magnesium fluoride, the effective conductivity, σ , is given by

$$\sigma = \omega \varepsilon'' = (2\pi \cdot 3 \cdot 10^8) \cdot (\varepsilon_r' \cdot \varepsilon_o \cdot \tan \delta)$$

$$= 0.0167 \varepsilon_r' \tan \delta \text{ mhos/m}$$

where tan δ is the loss tangent.

<u>Incident wave</u> - 300 MHz plane wave propagating down the axis of the structure toward its nose aperture;

<u>Desired fields</u> - Each component of total \overline{E} and total \overline{H} in two axial cross-section planes of the structure. First, with the cross-section plane parallel to the incident \overline{E} , and again with the plane parallel to the incident \overline{H} ;

Resolution - 1/3 cm uniformly throughout the mapping planes;

<u>Plotted values</u> - In decibels relative to an incident \overline{E} of 1 volt/meter and an incident \overline{H} of 1/377 ampere/meter.

To solve this coupling problem, the following steps were taken:

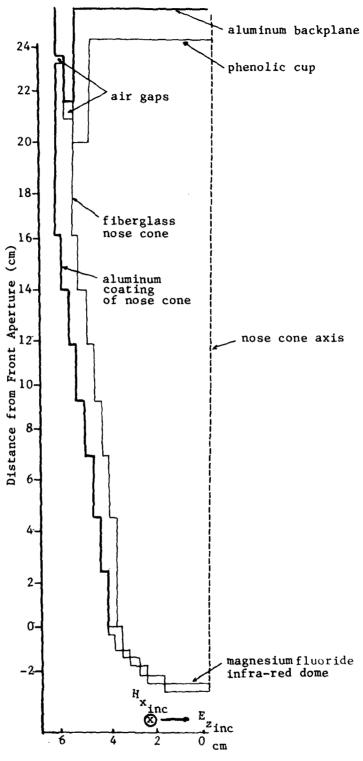


Fig.19. GEOMETRY OF NOSE CONE MODEL AT VERTICAL SYMMETRY PLANE, SHOWING COMPONENT MATERIALS.

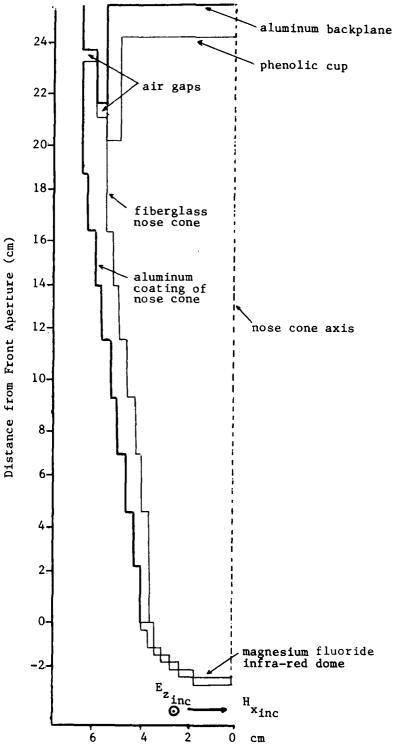


Fig.20. GEOMETRY OF NOSE CONE MODEL AT HORIZONTAL SYMMETRY PLANE, SHOWING COMPONENT MATERIALS.

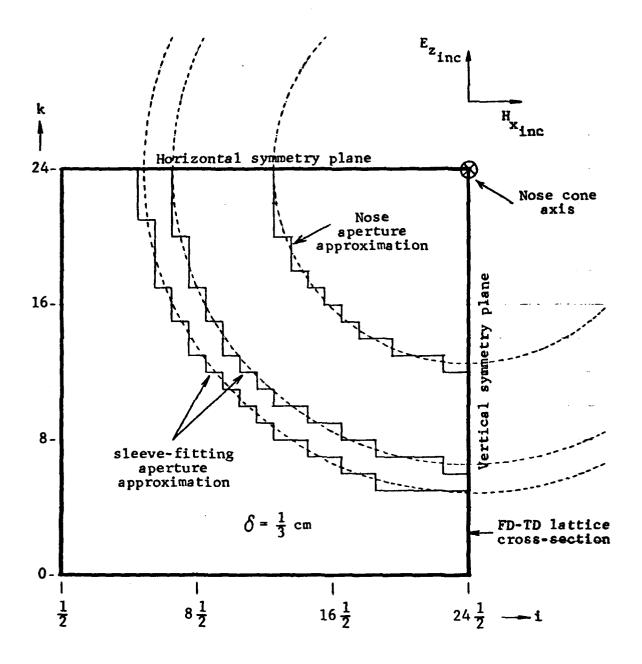


Fig. 21. KEY CROSS-SECTIONS OF NOSE-CONE MODEL

- a. The FD-TD computer program modeling the metal-only guidance section shell of RADC Contract F30602-77-C-0163 [Reference 8] was re-written to incorporate the algorithm speed-up provisions discussed in Section 3.2.
- b. A new data card deck (approximately 700 cards) was constructed to specify the metal and dielectric structure of Figures 19-21.
- c. The FD-TD program was run for 1800 time steps (equivalent to 3.0 cycles of the incident wave), assuming a slight amount of isotropic loss (σ_{int} = 0.025 mho/m) for the air within the cylinder to speed the rate of convergence. 7.8 x 10⁵ words of memory and 3.7 minutes of STAR-100 central processor time were required.
- d. The computed results for \overline{E} and \overline{H} were reduced to contour maps along the symmetry planes.

Figure 22 plots the computed contours for the 3 field components in the vertical symmetry plane, while Figure 23 plots the contours for the 3 field components in the horizontal symmetry plane. These figures can be directly compared with Figures 23 and 24, respectively, of Reference 8, which graph the FD-TD computed field contours for the missile guidance section shell without dielectrics. An intriguing observation is that the presence of the fiberglas in the circumferential sleeve fitting serves to increase the interior field level toward the rear of the guidance section shell by an average of about 15 dB. The general shape of the contours is unchanged, however.

This increase at first seems to be anomalous, since one would ordinarily expect that loading an aperture with a high-permittivity dielectric such as fiberglas would tend to reduce the transmitted fields. However, two reasonable physical mechanisms could explain the apparent anomaly:

1. The fiberglas-loaded sleeve fitting may form a nearly resonant aperture at 300 MHz. This is because the wavelength in fiberglas at this frequency is 42.6 cm (assuming a fiberglas relative permittivity of 5.5), very nearly equal to the 40.2-cm physical circumference of the sleeve fitting. Thus, any radial excitation of the sleeve-fitting gap would tend to be reinforced in phase along the

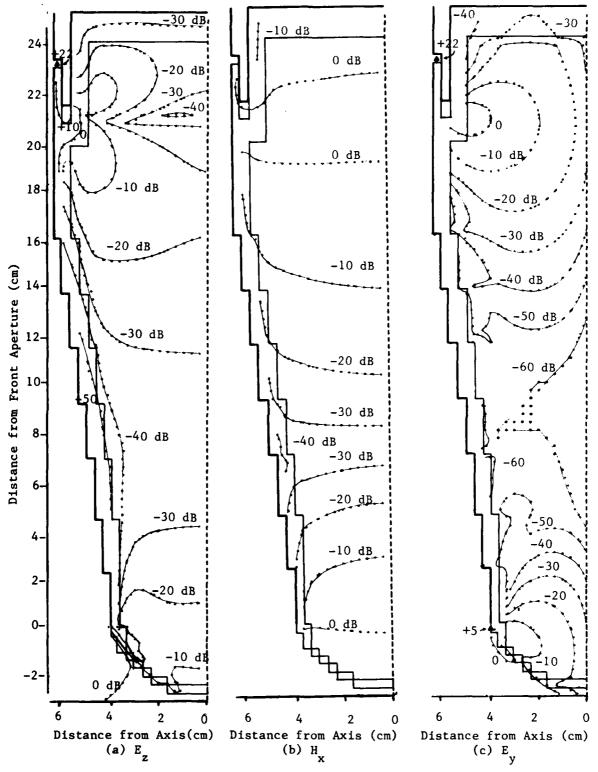
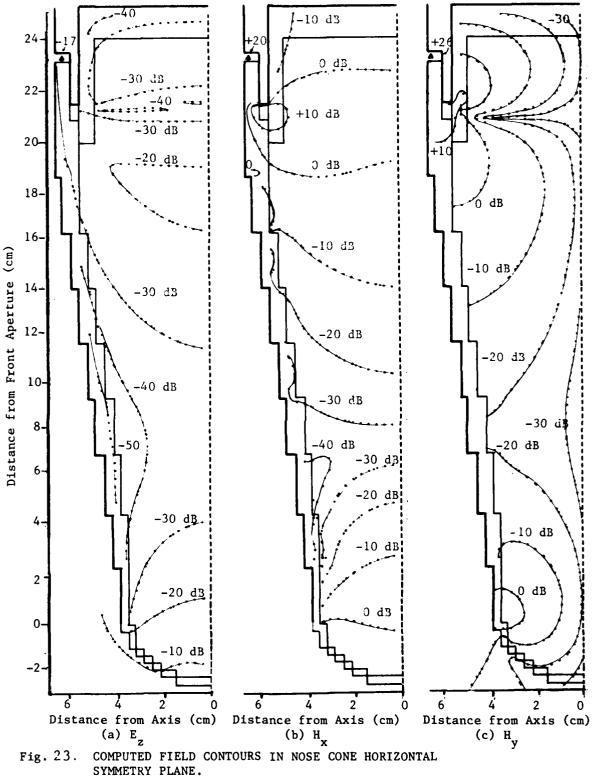


Fig. 22. COMPUTED FIELD CONTOURS IN NOSE CONE VERTICAL SYMMETRY PLANE



circumference of the sleeve fitting.

2. The fields excited radially in the fiberglas-loaded sleeve fitting may be channeled into the interior of the guidance section via the fiberglas itself, which might form a surface wave-guiding action in conjunction with the metal surrounding it.

The possible existence of the resonant-aperture phenomenon could be tested numerically by re-running the FD-TD model for several frequencies above and below 300 MHz. If the resonance exists, field penetration should be maximum at one frequency and fall off to either side.

4.2 Model 2 - Includes the Key Interior Metal Components as Well as the Dielectric Material

The FD-TD technique was employed to solve the following electromagnetic coupling problem:

<u>Interacting structure</u> - Identical to that of Model 1 (Figures 19-21), with the addition of the following metal and dielectric interior components:

- Head coil assembly (assumed solid metal);
- Cooled detector unit CDU (assumed solid metal);
- 3) Phenolic ring around the CDU;
- 4) Preamp can (metal);
- 5) Wire connecting the CDU to the preamp can;
- 6) Wire connecting the preamp can to the metal backplane; and
- 7) Longitudinal metal support rods.

These additional components are located as shown in Figures 24-26.

Incident wave - Axially directed 300 MHz, as in Model 1;

<u>Desired fields</u> - Total \overline{E} and total \overline{H} in two axial cross-section planes, as in Model).

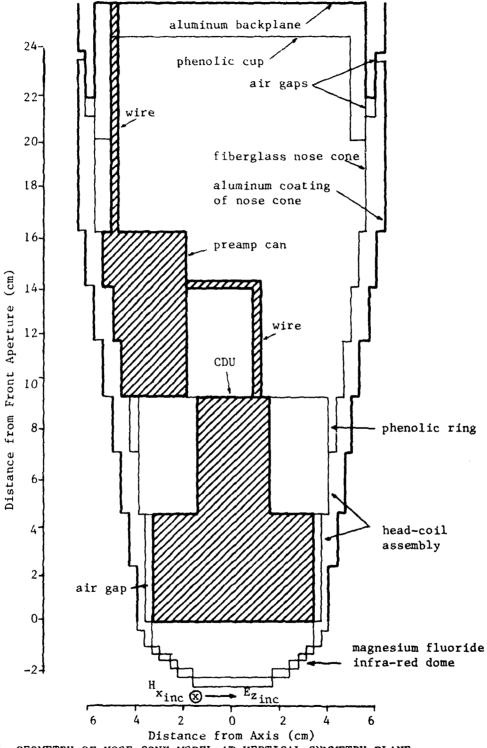


Fig. 24. GEOMETRY OF NOSE CONE MODEL AT VERTICAL SYMMETRY PLANE, SHOWING COMPONENT MATERIALS.

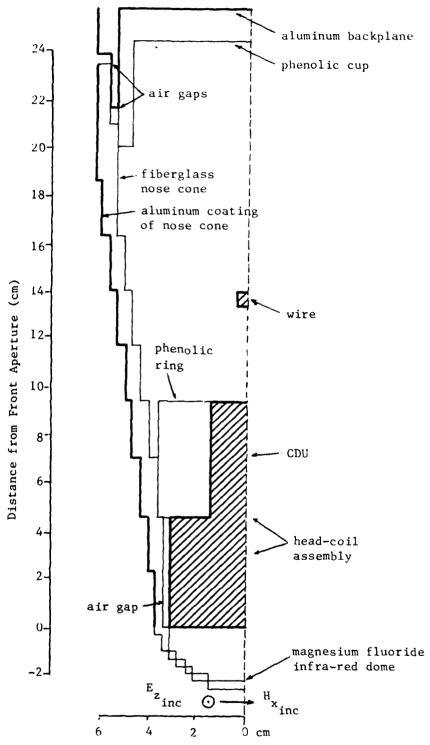


Fig.25. GEOMETRY OF NOSE CONE MODEL AT HORIZONTAL OBSERVATION PLANE, SHOWING COMPONENT MATERIALS.

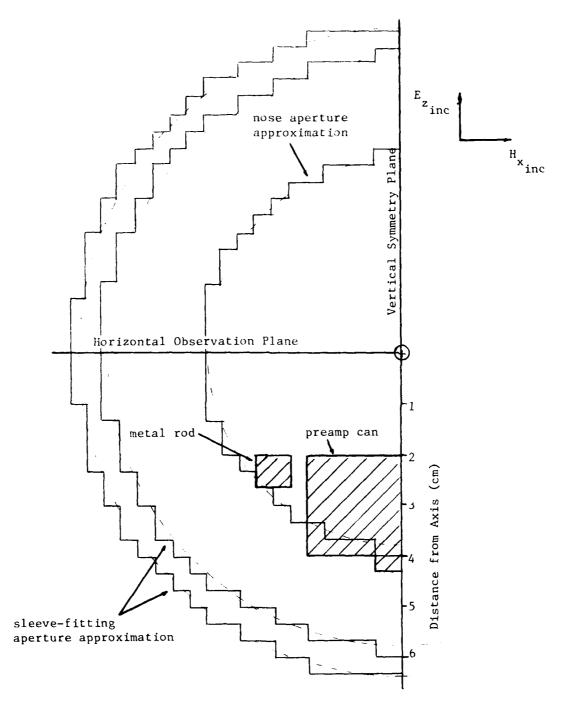


Fig. 26. KEY CROSS-SECTIONS OF NOSE CONE MODEL. HEAD-COIL ASSEMBLY AND COOLED DETECTOR UNIT NOT SHOWN.

Resolution - 1/3 cm, as in Model 1.

<u>Plotted values</u> - In decibels relative to incident \overline{E} and incident \overline{H} , as in Model 1.

To solve this coupling problem, the following steps were taken:

- a. The FD-TD computer program for Model 1 of the missile guidance section was re-written to eliminate the horizontal symmetry plane, since the interior metal components do not have this symmetry.
- b. Drawings of the missile guidance section were studied to determine the interior geometry. A new data card deck (approximately 700 cards) was constructed to specify the geometry.
- c. The FD-TD program was run for 1800 time steps (equivalent to 3.0 cycles of the incident wave), assuming a slight amount of isotropic loss (σ_{int} = 0.025 mho/m) for the air within the cylinder to speed the rate of convergence. 1.6·10⁶ words of memory and 7.0 minutes of STAR-100 central processor time were required.
- d. The computed results for \overline{E} and \overline{H} were reduced to contour maps along the symmetry planes.

Figures 27-29 plot the computed contours for the 3 field components in the vertical symmetry plane, while Figures 30 and 31 plot the contours for the 6 field components in the horizontal observation plane. These figures can be directly compared with Figures 22 and 23 for Model 1. It is seen that the metal components and wires serve to significantly disturb the field contours from the empty-shell case. Further, greatly increased fields penetrate into the interior of the guidance section near the metal components and wires. An important observation is that the wires connecting the cooled detector unit, preamp can, and metal backplane are paralleled by high-level magnetic field contours (as evidenced in Figures 28, 31a, and 31b). This is indicative of substantial, uniform current flow along these wires, and will be discussed in more detail in the next section.

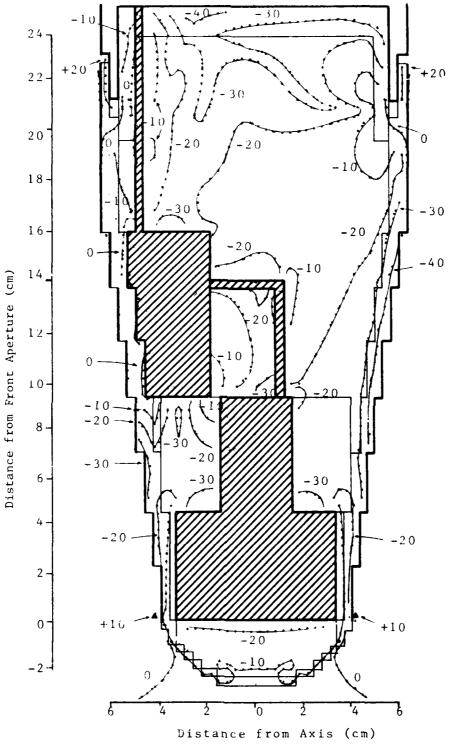


Fig.27. COMPUTED $\mathbf{E}_{\mathbf{z}}$ FIELD CONTOURS IN NOSE CONE VERTICAL SYMMETRY PLANE (IN DB)

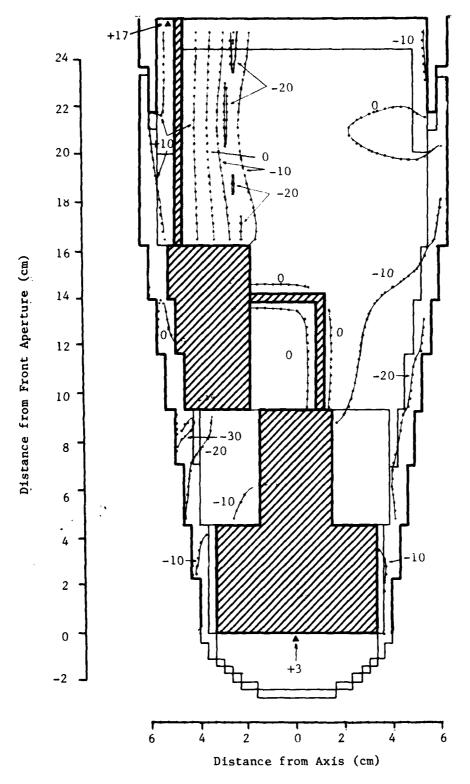


Fig.28. COMPUTED $H_{\mathbf{x}}$ CONTOURS IN NOSE CONE VERTICAL SYMMETRY PLANE (IN DB)

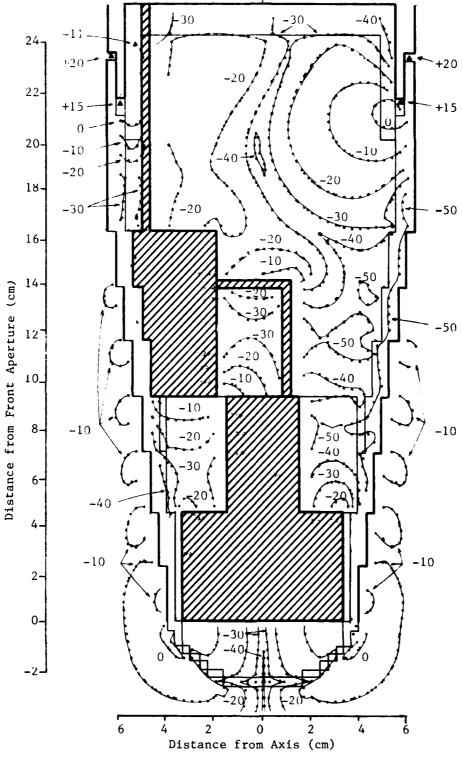


Fig. 29. COMPUTED E $_{\mathbf{y}}$ FIELD CONTOURS IN NOSE CONE VERTICAL SYMMETRY PLANE (IN DB)

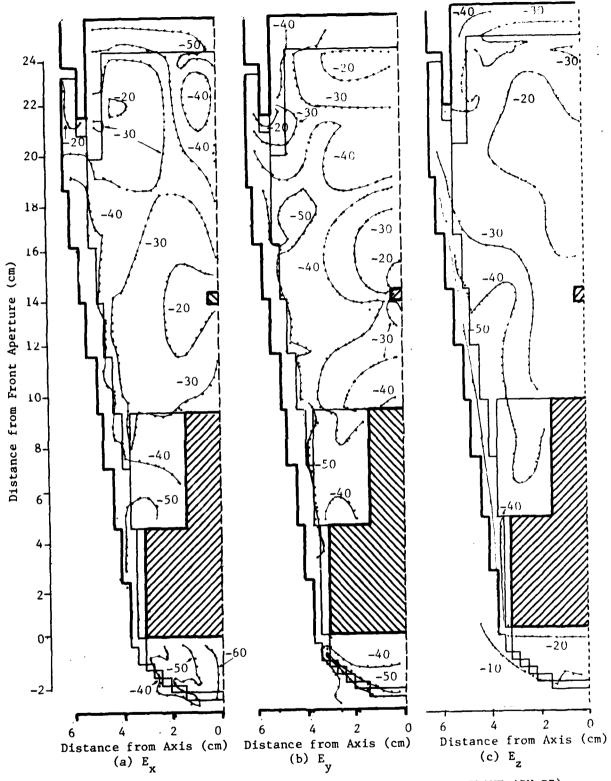
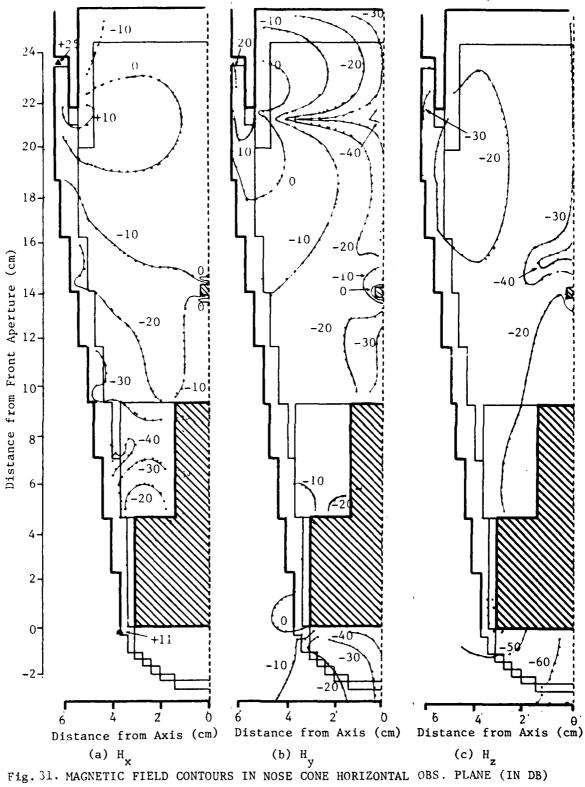


Fig. 30. ELECTRIC FIELD CONTOURS IN NOSE CONE HORIZONTAL OBS. PLANE (IN DB)



4.3 Conclusions

Completion of Program Task 2 demonstrates the capability of the FD-TD method to map fields coupled into a complex structure that has both irregular shaped apertures and interior dielectric and metallic materials. Determination of the accuracy bound for this method, as applied to complex structures, awaits the results of future experimental programs since other numerical approaches cannot deal directly with this level of complexity. No comparative data is available at this time.

5.0 PROGRAM TASK 3: PREDICTION OF THE COUPLING TO WIRES OR CABLE BUNDLES

A study of the ability of the FD-TD method to predict electromagnetic coupling to a wire or cable bundle was made using Model 2 of the missile guidance section (detailed in Section 4.2). As stated in that section of the report, the model included two connecting wires: 1) Wire 1 - between the cooled detector unit and the preamp can; and 2) Wire 2 - between the preamp can and the metal backplane. These wires were really idealizations of a more complex situation in which two multiconductor wire bundles extended between the structures mentioned. Some wires of the bundles terminated in electronic components; some were small-diameter cables with grounded shields. The goal was to model the direct metal-to-metal current path through the missile guidance section. Therefore, using a simple single-wire model for each bundle, only the ground-path current and equivalent common-mode current of each bundle was modeled using the FD-TD method.

5.1 Wire Model

Modeling of a connecting wire using the FD-TD method can be done best in a direct manner by specifying the wire model as a filamentary conducting path of realistic location relative to other components of the model. In this manner, certain transmission line properties of the wire, such as capacitance and external inductance, that arise due to its location relative to other structures are automatically accounted for in the time-domain solution of Maxwell's equations for the whole model, which includes the interaction of the wire and all adjacent structures. The transmission-line properties of the wire that arise due to internal impedance are accounted for by adjusting the model wire conductivity so that these properties match those of the actual conductor. This procedure is now discussed for the wire model of Section 4.2.

For the single-wire equivalent of each wire bundle, it was decided to select a round copper wire having an American (B & S) gauge of 15. The internal impedance of this wire at high frequencies [10] was

$$Z_{j}_{wire} = \frac{R_{s} (1 + j)}{2\pi r_{o}}$$

$$= \frac{(2.61 \cdot 10^{-7} \sqrt{f}) \cdot (1 + j)}{(2\pi) \cdot (0.000725)}$$

$$= 0.992 \cdot (1 + j) \text{ ohms/meter}$$
(19a)

where R_s = wire's copper surface resistivity (in ohms);

f = 300 MHz;

 r_0 = wire radius = 0.000725 meters.

For this choice, the internal resistance at 300 MHz was

$$R_{iwire} \simeq 1.0 \text{ ohm/meter}$$

and the internal reactance was

$$x_{i_{wire}} \simeq +1.0 \text{ ohm/meter.}$$

For the FD-TD model of the above wire, a conducting filament having a square cross section defined by a single lattice unit cell (1/3 cm) was used. By choosing the conductivity of the model wire medium to equal σ = 0.66 \cdot 10⁷ mhos/meter, the model wire could be defined to have the same internal impedance as the above 15 gauge copper wire:

$$Z_{i \text{ model}} = R_{s \text{ model}} \frac{\cdot (1 + j)}{(\text{model wire circumference})}$$

$$= \sqrt{\frac{\pi f \mu_0}{\frac{\sigma_{\text{model wire}}}{4} \cdot (\frac{0.01}{2})}}$$
 (19b)

=
$$1.0 \cdot (1 + j)$$
 ohms/meter

where μ_0 = vacuum permeability = $4\pi \cdot 10^{-7}$ henrys/meter f = 300 MHz $\sigma_{model\ wire}$ = 0.66·10 7 mhos/meter.

5.2 Results

In Figure 28 of Section 4.2, note how the computed 0 dB contour of H_{χ} nearly parallels the model ground wire connecting the cooled detector unit to the pre-amp can. This behavior, combined with computed data showing that the longitudinal electric field at the wire is small, is indicative of a transverse electromagnetic (TEM) wave mode propagating along the ground wire. In effect, current flow through the wire generates locally a magnetic field looping around the wire, which when "cut" by the vertical symmetry plane, shows up as parallel field contours spaced equally on each side of the wire. For this case, Ampere's generalized law reduces to the situation illustrated in Figure 32:

$$\oint_{L} \bar{H} \cdot d\bar{L} = \int_{S} \bar{I} \cdot d\bar{S} + \frac{\partial}{\partial t} \int_{S} \bar{D} \cdot d\bar{S} \qquad (20a)$$

$$H \cdot 2\pi r_{0} \simeq I_{wire} + 0 \qquad (20b)$$

In this manner, $I_{\rm wire}$ can be estimated by knowledge of the magnitude and location of the parallel, adjacent, magnetic field contours. This applies equally well to the ground wire connecting the pre-amp can to the backplane, which is seen to have parallel + 10 dB H $_{\rm v}$ contours on either side.

Table I lists the predicted values of I_1 (current in the wire from the cooled detector unit to the pre-amp can) and I_2 (current in the wire from the pre-amp can to the backplane). For the case of I_1 , it is assumed that $H=H_{inc}$ and $r_0=1.5$ $\delta=0.005$ m. For the case of I_2 , it is assumed that H=3.16 H_{inc} and $r_0=1.5$ $\delta=0.005$ m.

Table 1
PREDICTED GROUND WIRE CURRENTS

E _{inc} (v/m)	H _{inc} (A/m)	Pinc (µW/cm ²)	I _l (µA)	Ι ₂ (μΑ)	
0.1	2.65.10-4	2.65.10-3	8.3	26.3	
1.0	2.65·10 ⁻³	0.265	83	263	
10.0	2.65 [.] 10 ⁻²	26.5	830	2630	
L				3	

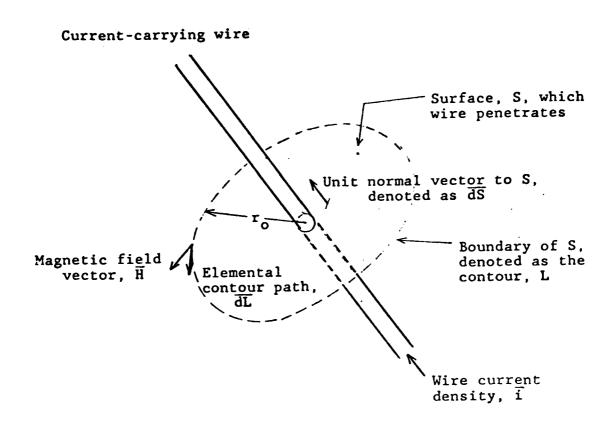


Fig. 32. GEOMETRY OF AMPERE'S LAW

5.3 Conclusions

Completion of Program Task 3 demonstrates the ability of the FD-TD technique to directly predict the current that the coupled fields may induce on a wire or bundle of wires which is located inside a complicated structure (such as a missile guidance section). Here, the observed parallelism of the computed magnetic field contours near the modeled wire(s) is employed in combination with Ampere's law to translate FD-TD-computed magnetic fields to wire current magnitudes. Confirmation of the FD-TD computed wire currents is required in a future experimental program.

6.0 PROGRAM TASK 4: DETERMINATION OF THE SIZE LIMITS OF AN OBJECT THAT CAN BE MODELED BY THE FD-TD METHOD

6.1 General Considerations

Like many other electromagnetic-analysis computer methods, the FD-TD approach requires significant quantities of computer memory and processing time to model realistic problems. In general, the computer resources needed by the FD-TD method increase for larger structures and finer spatial resolutions, since more memory and processing time is required to account for higher levels of geometric detail. Clearly, arbitrarily-large objects cannot be modeled using this method.

The purpose of this section is to allow an estimate of the maximum size of an object that can be modeled using the FD-TD method, given limitations of the available computer system. It will be shown that the most important limiting factors of any computer system in implementing the FD-TD method are:

- Quantity of available fast-access central memory, such as magnetic core and semiconductor arrays;
- 2. Data transmission speed of on-line mass storage memory, such as magnetic disc; and
- 3. Floating-point operation speed.

6.2 Required Computer Memory

At each time step of the FD-TD algorithm, the following twelve data quantities are stored in computer memory for each unit cell of the space lattice: 1) Three vector components of \overline{E} ; 2) Three vector components of \overline{H} ; and 3) Six constant coefficients. Additional computer memory is needed to implement the lattice truncation conditions at the outermost cells of the lattice. Overall, it has been found that the following is an accurate estimate of the total computer memory requirement, M, for a FD-TD lattice containing N cells:

 $M \simeq 13.6N$ words of memory.

(21a)

The N cells are arranged in a three-dimensional cubic lattice to permit the maximum flexibility in specifying an arbitrary object. Denoting the maximum span of the object in three perpendicular directions as D_1 , D_2 , D_3 meters, respectively; the lattice cell size as δ meters; and the number of perpendicular symmetry planes of the object/electromagnetic excitation as s = 0, 1, or 2, M is computed to be

$$M \approx 13.6N$$

$$\approx 13.6 \times (\frac{D_1}{\xi}) \times (\frac{D_2}{\xi}) \times (\frac{D_3}{\delta})$$

$$\approx 13.6 D_1 D_2 D_3$$

$$\frac{2^5 \delta^3}{\delta^3} \text{ words of memory.}$$
(21b)

Equation 21b specifies the memory requirement for plane wave excitations having arbitrary polarization and angle of incidence. Further, using the hybrid computation approach developed in Section 7 of this report, Equation 21b holds for both compact, isolated objects as well as sub-zones or cavities of extended objects which can be treated via the aperture electric current equivalence theorem. In the former case, D_1 , D_2 , and D_3 are simply the maximum spans of the isolated object. In the latter case, D_1 , D_2 , and D_3 are the maximum spans of only the sub-zone or cavity, rather than the object as a whole. Thus, the hybrid approach allows excellent resolution of distinct zones or cavities of objects that may have overall much larger dimensions, as will be shown in Section 7.0.

6.3 Required Computer Processing Time

6.3.1 Central Processing Time

At each time step of the FD-TD algorithm, the following arithmetic operations are performed for each unit cell of the space lattice (assuming permeability, μ , equal to μ_0 everywhere in the lattice): 1) 6 floating-point multiplications; and 2) 24 floating-point additions or subtractions. Additional operations are needed to implement the lattice truncation conditions and the envelope computations. Overall, however, it has been found that the central processing time is dominated by the basic time-stepping operations.

Scalar Processing Machines

Denoting the computation time for one single-precision floating-point multiplication as τ_m , and the computation time for one single-precision floating-point addition as τ_a , the following is an estimate of the central processing time, CP_1 , for one time step of the FD-TD algorithm over N cells:

$$CP_1 \simeq (6 \tau_m + 24 \tau_a) \times N \frac{\text{seconds}}{\text{time step}}$$
 (22a)

Assuming that R cycles of the excitation frequency, f, must be time-stepped to attain the sinusoidal steady state, the number of FD-TD algorithm time steps needed is

$$\frac{n_{\text{max}}}{\delta t} = \frac{\left(\frac{R}{f}\right)}{\left(\frac{\delta}{2c}\right)} = \frac{2cR}{f\delta} \quad \text{time steps}$$
(22b)

where δt is the time-step size of the FD-TD algorithm, δ is the lattice-cell size, and c is the speed of light in vacuum. Therefore, from Equations 22a and 22b, the total central processing time, CP, is estimated as

$$CP \simeq CP_1 \times n_{max}$$

$$\simeq (6\tau_m + 24\tau_a) \times N \times \frac{2cR}{f\delta}$$

$$\simeq (6\tau_m + 24\tau_a) \times (\frac{D_1}{2^S} \frac{D_2}{\delta^3}) \times \frac{2cR}{f\delta}$$

$$\simeq \frac{(6\tau_m + 24\tau_a) D_1}{f\delta^4} \frac{D_2}{\delta^3} \frac{D_3}{\delta^3} \frac{2^{1-s}}{\delta^3} = \frac{C}{\delta^4}$$
 seconds (23)

where D_1 , D_2 , and D_3 are the maximum spans of the object, and s=0, 1, or 2, as discussed in the previous sub-section.

From Equation 23, it is seen that the central processing time is inversely proportional to the frequency, f, and to the fourth power of the lattice cell size, δ , assuming a fixed number, R, of cycles required to attain the sinusoidal steady state. The major implications of this are twofold:

- Low-frequency solutions require more CP time than high frequency solutions, all other parameters being fixed; and
- 2. Major savings of CP time can be achieved by only minor increases of δ , the effective spatial resolution.

Vector Array Processing Machines

Some recent computers have the capability to perform arithmetic operations on whole arrays, or vectors, of numbers in a highly parallel manner. Two examples of such machines available as a utility service are the Cyber 203* (Control Data Corporation Cybernet) and the Cray 1 (United Computing Systems, Inc.). Such a capability is ideal for implementation of the FD-TD method since virtually all of its operations are fully explicit and are performed on very large arrays of numbers.

In estimating the central processing time for the FD-TD method on an array processing computer such as the Cyber 203 or the Cray 1, the key computer parameter is the machine cycle time, $\tau_{\rm C}$, since one floating point multiplication or addition can be performed by such machines each $\tau_{\rm C}$. For this case, Equation 23 is slightly modified to

$$CP \simeq \frac{30 \tau_c D_1 D_2 D_3 2^{1-s} c R}{f \delta^4}$$
 seconds. (24)

 τ_{c} is approximately 12.5 nsec for the machines mentioned.

6.3.2 Peripheral Processing Time

At each time step of the FD-TD algorithm, the following twelve data quantities are retrieved from computer memory for each unit cell of the space lattice: 1) Three vector components of \overline{E} ; 2) Three vector components of \overline{H} ; and 3) Six constant coefficients. Further, the following six data quantities are returned to computer memory: 1) Three vector components of \overline{E} ; and 2) Three vector components of \overline{H} . For large modeling problems involving a memory requirement that is larger than the maximum central memory available to the user, it becomes necessary to use the available high-speed mass storage, such as magnetic disc files.

^{*}successor to the STAR-100

In this case, the central memory is used only as a scratchpad or buffer to iteratively access portions of the mars memory, perform the necessary arithmetic operations, and return the upd. ced electromagnetic field quantities to the mass memory. Data transfer can be programmed either in an explicit fashion or, on machines with virtual memory, can be performed automatically by the computer.

The transfer of large quantities of data each time step from mass storage to central memory and back to mass storage requires a finite length of time that is usually placed under the category of peripheral processing (PP) time. Here, the key factor in determining PP time is the rate of data transmission, $\mathbf{r_d}$ words/second, to and from the mass storage device. Using the same nomenclature as in the previous subsections, the peripheral processing time for one time step, PP_1 , is estimated as

$$PP_1 \simeq \frac{18N}{r_d} \frac{\text{seconds}}{\text{time step}}$$
 (25a)

The peripheral processing time for the modeling of the entire problem is, from Equations 25a and 22b,

$$PP \simeq PP_{1} \times n_{max}$$

$$\simeq \frac{18N}{r_{d}} \times \frac{2cR}{f\delta}$$

$$\simeq \frac{18}{r_{d}} \times \left(\frac{D_{1} D_{2} D_{3}}{2^{S} \delta^{3}}\right) \times \frac{2cR}{f\delta}$$

$$\simeq \frac{18 D_{1} D_{2} D_{3} 2^{1-S} cR}{r_{d} f\delta^{4}} \text{ seconds.}$$

$$(25b)$$

Like the CP time, the PP time is inversely proportional to the frequency, f, and to the fourth power of the lattice cell size, δ . Again, increasing δ only slightly helps to significantly reduce processing time.

6.4 Impact of Requirements for Computer Memory, CP Time, and PP Time

During the present research effort, many large FD-TD programs involving $N > 10^5$ cells and $M > 10^6$ words were run on the Control Data STAR-100 and Cyber 203 computers. As a result of this experience, the following conclusions have been reached relative to the impact of requirements for computer memory, CP time, and PP time in large FD-TD models.

- 1. Limiting M to <u>less</u> than the central memory limit of the computer, so that no spill-over onto mass storage occurs, results in relatively very small amounts of PP time. Here, the total program running time ("wall clock time") is essentially equal to the CP time, which is in the range of a few minutes for the Control Data STAR-100 or Cyber 203.
- 2. If <u>any</u> mass storage is used, the program running time increases significantly to the range of a few hours. Here, the CP time remains very low for the STAR-100 or Cyber 203, but the PP time becomes dominant. Program provisions for re-start at the last completed time step should be included to avoid having to re-run the entire program from the very first time step if the computer system should "go down" during the lengthy program running period.
- 3. Usage of slower machines than the STAR-100 or Cyber 203 would effect mainly the CP time. Thus, large FD-TD models that employ mass storage could be run on conventional scalar machines such as the Cyber 76, Univac 1100, or Honeywell 6000 series with "wall clock" times similar to those obtained on vector processors such as the STAR-100. In fact, efficient programming of the accessing of high speed disc storage devices could serve to reduce "wall clock time" for such conventional machines and provide a program re-start capability.

Overall, in determining the size limits of an object that can be modeled using the FD-TD method, one must consider the following points:

- 1. Will mass storage be used? If mass storage is used, there is no real limit to M of Equation 21b, so that arbitrarily large objects can be modeled, in principle. However, in practice, the object size is limited by the maximum "wall clock time" of the program which is acceptable to both the user of the program and the operator of the computing center. This is given as a function of the spatial dimensions of the object, the lattice cell size, and the characteristics of the computer by the CP time of Equation 23 plus the PP time of Equation 25b.
- 2. If mass storage is not used, the value of M of Equation 21b is limited to the user-accessible part of the computer central memory. Now, the object size is limited sharply by Equation 21b because larger objects (or ones with higher spatial resolution) simply cannot be fitted into the computer central memory. Here, the question of increasing the lattice cell size, δ , becomes important because of the strong third-power dependence of M upon δ .

7.0 PROGRAM TASK 5: INVESTIGATION OF INTERFACING THE FD-TD METHOD WITH OTHER ANALYSIS TECHNIQUES

7.1 Introduction

The analysis of the electromagnetic excitation of an aperture on an arbitrarily shaped object is a complex problem [11]. This problem has been given special attention in the broad area of EMP penetration and simulation studies [12], with great efforts being applied to assess coupling to objects present behind apertures on finite, metallic, hollow scattering bodies.

The problem of the penetration and coupling of electromagnetic energy through an aperture has been studied extensively by many investigators using analytical and method-of-moments (MOM) numerical approaches [13] to characterize the behavior of simple aperture shapes in a conducting screen [14] - [18] or in a finite, scattering body [19], [20]. However, the analysis becomes very complex if there are other scattering objects in the vicinity which are coupled to the aperture [11], [21], [22] wherein the mutual interaction must be fully taken into account. A powerful alternate approach is the pure FD-TD method, discussed in detail in the previous sections of this report, which allows computation of the penetrated internal electromagnetic fields by direct modeling of the object of interest, including apertures and internal contents.

In order to treat coupling problems more effectively, a new hybrid MOM/FD-TD technique has been developed based on a novel use of the so-called "field equivalence theorem" due to Schelkunoff [23]. This hybrid technique and its applications, described in this section, is basically an equivalent aperture excitation method. This allows analysis of the coupling problem in two distinct steps:

Step 1 - Analysis of the relatively simple exterior problem using the method of moments (or some other appropriate technique) to determine the equivalent excitation currents and/or fields in the aperture regions. This can be done independent of any knowledge of the interior contents of the object of interest. Step 2 - Use of the FD-TD method to analyze the relatively complex interior problem, assuming as an excitation the equivalent currents or fields found in Step 1.

In this way, each analysis technique is applied in the structure size and complexity range that it is best suited for, allowing an overall solution that is accurate for large, simple structures with small, complex apertures or other fine interior details. The specific details of adaptation of the data obtained from the MOM frequency-domain method to the FD-TD time-domain method will be discussed later in the section covering hybrid method applications.

7.2 Basis of the Hybrid Technique

In this sub-section, the hybrid technique based on the use of the field equivalence theorem by Schelkunoff [23] (often referred to as Schelkunoff's third equivalence theorem, as in his original paper) is explained in a systematic manner to analyze aperture field penetration and coupling into structures by interfacing the MOM technique (for the exterior-region analysis) with the FD-TD technique (for the interior-region analysis). The general idea behind the hybrid approach is not new, since Schuman and Warren applied the Schelkunoff third theorem to interface the MOM technique with MOM to separately analyze the exterior and interior regions of an open-ended cylinder and a nose-cone structure with a nose aperture and a thin circumferential gap aperture [20]. Both the cylinder and nose-cone structures were treated as bodies of revolution. Their analysis was restricted only to empty interior regions or cavities. If the interior region is complicated by the addition of interacting material bodies, the MOM/MOM hybriding becomes very complicated and difficult. For such a situation, a MOM/FD-TD hybriding remains possible, as will be shown, even for interior material bodies strongly coupled to the apertures.

7.2.1 MOM / MOM Hybrid Technique

Figure 33 illustrates the classical problem of a perfectly conducting scatterer, S_C , with an aperture, S_A . External to the scatterer in Region 1, an incident field $(\overline{E}^i, \overline{H}^i)$ illuminates the aperture, and part of the energy penetrates into the cavity (Region 2) through the aperture. To compute the

REGION () $(\vec{E}_{|}, \vec{H}_{|})$

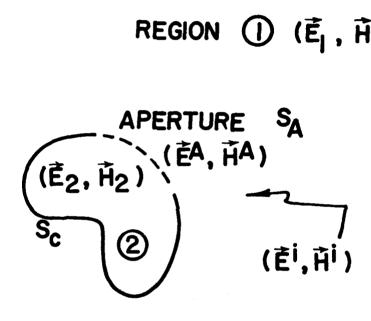


Fig. 33. PERFECTLY CONDUCTING SCATTERER WITH APERTURE

total field $(\overline{E}_2, \overline{H}_2)$ in Region 2, many analytical and MOM numerical approaches studied in the literature have employed integral-equation formulations treating Regions 1 and 2 simultaneously. These approaches characterize either S_A or S_C in terms of tangential fields or equivalent surface currents [13].

Recently, Schuman and Warren [20] have developed a hybrid technique to treat the Region 1 problem and the Region 2 problem separately, and compute coupling through arbitrarily-shaped apertures in conducting bodies of revolution. In this manner, rotationally-symmetric cavities with arbitrary contours can be modeled. Further, the sensitivity and accuracy of field computation is greatly improved for cases when the aperture coupling is small and/or points deep within the cavity are sought. The latter is realized because the hybrid method avoids any substraction of nearly-equal impressed and scattered fields to compute the total field within Region 2. Thus, error due to residual subtraction noise is eliminated. The hybrid approach of Schuman and Warren is illustrated in Figure 34, and is summarized below as a five-step computation.

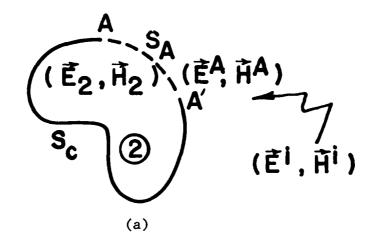
Region 1: MOM Technique

- (a) The aperture region, S_A , is short-circuited, and the straight-forward exterior problem is solved [24], [25] to obtain the induced electric current distribution, \overline{J}_0^A , in the short-circuited aperture region (Figure 34b).
- (b) The short-circuit current, \overline{J}_0^A , is now placed in the open circuited aperture region with a sign change (Figure 34c) to account for the continuity of the fields in the aperture region [23]. The electric current, $-\overline{J}_0^A$, fictitiously placed in the open-circuited aperture region acts as an equivalent source for the interior fields in Region 2.

Region 2: MOM Technique

(c) Based on the generalized multiport approach [13], referring to Region 2, an equivalent electric field excitation, \overline{E}^A , existing only in the aperture region (Figure 34d) is determined which will produce the electric current, $-\overline{J}_0^A$, with the aperture short-circuited.

REGION (\vec{E}_1, \vec{H}_1)



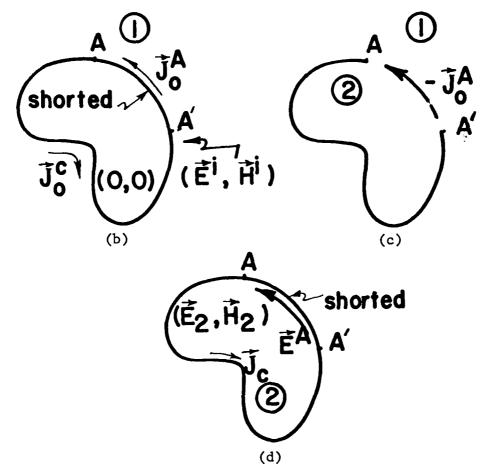


Fig. 34. MOM/MOM HYBRID TECHNIQUE

- (d) The electric current distribution, \overline{J}^C , is obtained on the interior surface of the conducting body with \overline{E}^A as the source equivalent electric field (Figure 34d).
- (e) The interior fields $(\overline{E}_2, \overline{H}_2)$ are now computed based on \overline{J}^C and \overline{E}^A or $-\overline{J}_0^A$.

The mathematical formulation of the hybrid MOM / MOM technique [20], [24], [25] is beyond the scope of this report and is not treated here. However, one point should be repeated from the original paper of Schuman and Warren [20]. Namely, any loading within the cavity region (Region 2) changes the aperture equivalent electric field excitation, \overline{E}^A , of Step (c) above. Therefore, the generalized multiport approach of Step (c) must take into account any loading within the cavity by either metal or dielectric objects. This requirement introduces considerable complexity, and perhaps explains why the MOM / MOM hybrid approach has not been more widely used as a means of modeling realistic problems. This cavity loading effect is discussed in more detail in Section 7.3, where it is shown that MOM / MOM hybriding is very complicated even for the simple case of aperture loading by a thin wire in the cavity region. On the other hand, a hybrid formulation employing MOM / FD-TD does <u>not</u> require computation of \overline{E}^A , and totally avoids the complicating effect of loading within the cavity.

7.2.2 MOM / FD-TD Hybrid Technique

In order to determine the applicability of the FD-TD method (a time-domain approach) to interface effectively with other numerical procedures such as the method of moments (a frequency-domain approach), the hybrid MOM / FD-TD technique has been successfully developed and implemented to compute aperture coupling and field penetration. Again, the hybrid formulation allows one to treat the exterior (Region 1) problem and the interior (Region 2) problems separately in two distinct steps. In Figure 35, the hybrid MOM / FD-TD technique is illustrated schematically, and is summarized below as a four-step computation.

REGION (\hat{E}_1, \hat{H}_1)

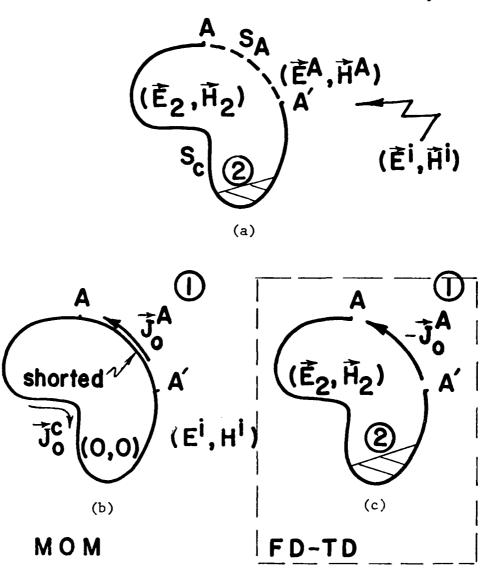


Fig. 35. MOM / FD-TD HYBRID TECHNIQUE

Region 1: MOM Technique

- (a) Identical to Step (a) of Section 7.2.1, the aperture region, S_A , is short-circuited, and the straightforward exterior problem is solved to obtain the induced electric current distribution, \overline{J}_0^A , in the short-circuited aperture region (Figure 35b). In Appendix A, a brief summary of the analytical [24], [25] and numerical formulation [11], [15], [26] needed to compute \overline{J}_0^A on a perfectly-conducting body of revolution is discussed.
- (b) Identical to Step (b) of Section 7.2.1, the short-circuit current, \overline{J}_0^A , is now placed in the open-circuited aperture region with a sign change (Figure 35c) to account for the continuity of the fields in the aperture region. The electric current, $-\overline{J}_0^A$, fictitiously placed in the open-circuited aperture region acts as an equivalent source for the interior fields in Region 2.

Region 2: FD-TD Technique

- (c) We note that the MOM technique gives the equivalent current source distribution, $-\overline{J}_0^A$, in the frequency domain as a spatial distribution of phasor quantities having both magnitude (relative to the incident fields) and phase (relative to some phase reference, normally at the origin of the coordinate system). With the FD-TD method being a time-domain technique, the phase distribution of $-\overline{J}_0^A$ is interpreted as a time-delay distribution with respect to the original phase reference location. The magnitude distribution is taken intact without interpretation or modification. In this manner, the FD-TD aperture equivalent current source distribution assumes sinusoidal steady-state quantities starting at the very beginning of time-stepping, with the proper time delay to account for phase shift.
- (d) Using the FD-TD approach, the interior fields $(\overline{E}_2, \overline{H}_2)$ are computed directly by using $-\overline{J}_0^A$ as a source term distribution in the ∇ X \overline{H} difference equations. No additional complication is involved if the cavity is loaded in any manner, since this loading is modeled directly on the FD-TD lattice. Thus, there

is no penalty for modeling the cavity interior to as fine an extent as possible.

7.3 Canonical Case Studies: MOM / MOM Hybrid Technique

In this section, some studies are reported regarding the validity of applying Schelkunoff's third equivalence principle for apertures having wires closely coupled to them. Additional results are also reported concerning the need to model the entire interaction geometry when applying the equivalence principle, instead of modeling just the cavity of interest. These studies were conducted using the MOM / MOM hybrid technique applied to the canonical geometry of a thin wire scatterer placed behind a narrow-slot perforated conducting screen, as shown in Figure 36. Two different cases were examined:

Case A - Direct straightforward MOM solution of the entire problem; and

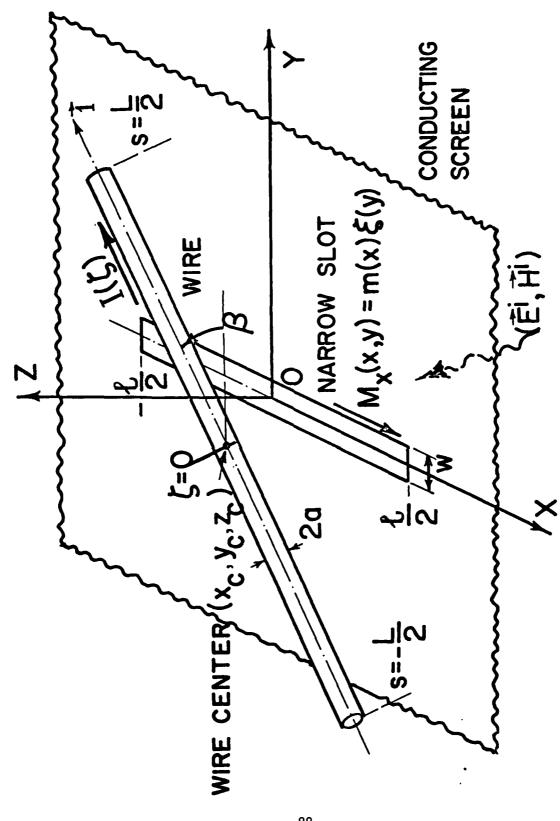
Case B - Hybrid MOM / MOM technique.

These will now be discussed.

Case A: Direct straightforward method-of-moments solution

The general theory of aperture coupling and transient characterization of conducting bodies placed behind an arbitrary shaped aperture in a screen has been treated in Reference 11. Specifically, the present canonical problem (Figure 36) was reported in Reference 27 with numerical results derived via the direct method of moments solution. Basically, a coupled set of integro-differential equations [11], [27], [28] was derived by treating the aperture electric field distribution and the wire electric current distribution as unknowns by enforcing appropriate boundary conditions at the aperture and on the wire. The coupled equations were solved by expanding the unknown distributions in terms of standard pulse functions and then testing the resulting equations using piecewise triangular functions [13]. A brief summary of the coupled integral equations for this problem is given in Appendix B.

For the geometry of the narrow slot/thin wire shown in Figure 36, we define the following parameters:



GEOMETRY OF WIRE SCATTERER BEHIND NARROW SLOT Fig. 36.

 ℓ = length of narrow slot = 0.5 λ

w = width of narrow slot = 0.5 λ

L = length of wire scatterer = 0.5λ

a = radius of wire scatterer = 0.001λ

 (x_c, y_c, z_c) = location of the center of wire scatterer in upper half space (z > 0) = $(0, 0, 0.25 \lambda)$

 β = angle of wire relative to y axis = 0°

Further, the narrow slot is oriented along the axis, and the plane wave $(\stackrel{\rightarrow}{E_y}^i,\stackrel{\rightarrow}{H_X}^i)$ excites the slot region in the lower half space (z < 0).

Figures 37 and 38 show the results of the direct method-of moments solution. Both the slot and the wire are assumed to have 0.5 m resonant lengths, and the wire is placed at a distance 0.25 m directly above the slot. The slot is excited by a 300 MHz plane wave in the lower half space (z < 0) at normal incidence to the conducting screen. The electric field, E_y , in the slot is characterized in terms of an equivalent magnetic current distribution [27] M_x , in the shadow side

$$\hat{y} E_{v} = \hat{x} M_{x} \times \hat{z}$$
 (26)

$$M_{y} = m(x) \xi (y) \tag{27}$$

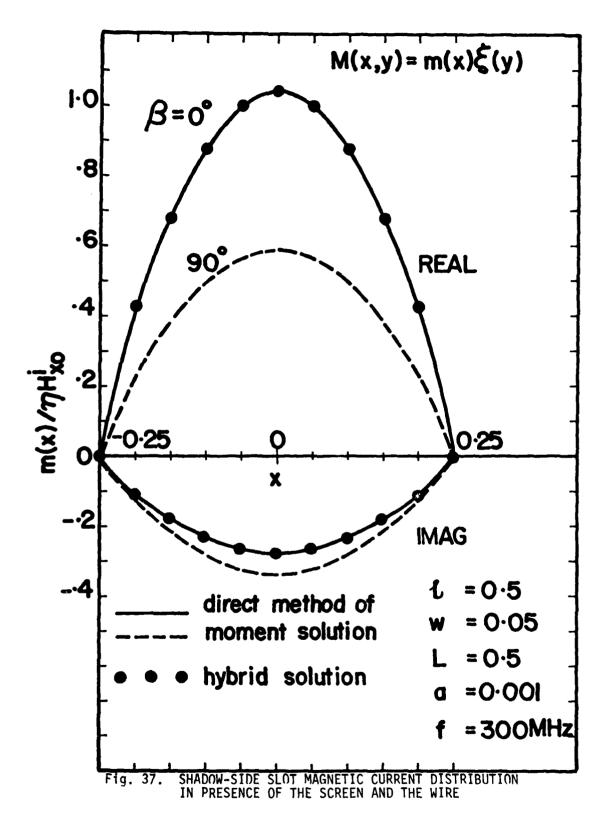
where

m(x) = axial distribution of the equivalent magnetic current in the slot

 $\xi(y)$ = transverse distribution of the equivalent magnetic current in the slot

$$= \frac{1}{\pi} \left[\left(\frac{\mathsf{w}}{2} \right)^2 - \mathsf{y}^2 \right]^{-\frac{1}{2}} \tag{28}$$

In Figure 37, the shadow side (z=0+) slot axial magnetic current distribution m(x) in the presence of the screen and the wire is plotted for $\beta=0$. This angle corresponds to the wire axis being physically perpendicular to the slot axis, which is the orientation for maximum coupling and interaction between the slot and wire. Both real and imaginary parts of m(x) are plotted. Figure 38 plots the corresponding distribution of the induced



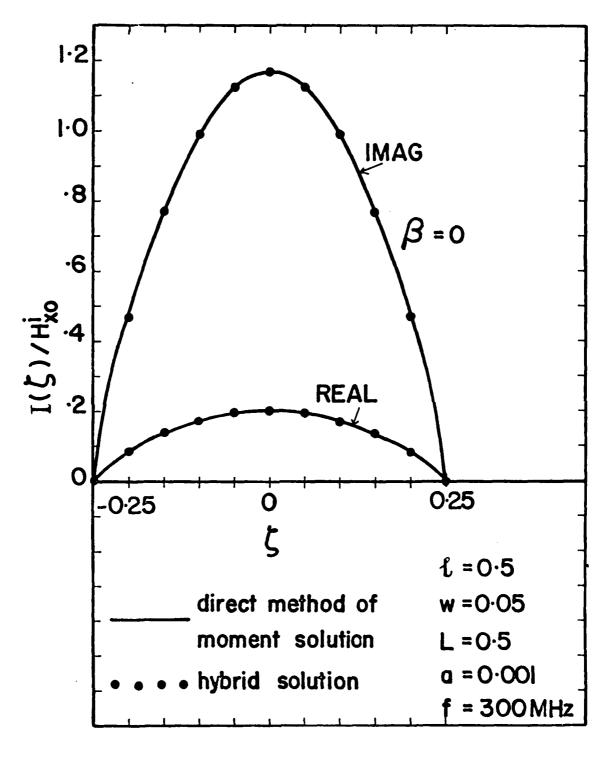


Fig. 38. WIRE ELECTRIC CURRENT DISTRIBUTION IN THE PRESENCE OF THE SCREEN AND THE NARROW SLOT

electric current on the wire.*

Case B: Hybrid MOM / MOM technique

The limitation of Case A (which involves formulation of a coupled set of integro-differential equations and solution via the straight method of moments) is that one has to analyze the complete problem in a simultaneous solution. As stated in Section 7.2.1, an alternative is to decompose the problem according to the MOM / MOM hybrid technique. This involves the successful application of the Schelkunoff third equivalence theorem [23].

To apply this technique, the slot in the canonical geometry shown in Figure 36 is first short-circuited by replacing the slot by a perfectly conducting material identical to the screen itself. Next, the lower half space, z < 0, is analyzed as a pure boundary value problem. The induced electric current, \vec{J}_0 , on the shorted region of the slot is determined for the given incident excitation. For a plane wave incident normally on the screen with \vec{H}_X^i and \vec{E}_y^i oriented along x and -y coordinate axes, the equivalent current excitation is given by

$$\vec{J}_0 = -2H_x^{\dagger} \hat{y}. \tag{29a}$$

Next, we go back to the original problem and place in the open-circuited slotted region an equivalent aperture electric current excitation of

$$\vec{J}^{A} = -\vec{J}_{O}$$

$$= 2H_{V}^{i} \hat{y} . \tag{29b}$$

For β = 90°, the induced electric current on the wire is zero, representing complete uncoupling of the wire and slot.

^{*}For β = 90°, the slot and wire are completely uncoupled, and the penetrating field is unaffected by the presence of the thin wire. Here, the m(x) distribution has been verified, since it is the Babinet equivalent of a narrow strip. Further, the narrow strip distribution can be verified with respect to a thin wire of diameter equal to half the strip width.

The sign change in Equation 29b is in accordance with the boundary condition requirements. This completes the first stage in implementing the hybrid technique.

The second stage in implementing the hybrid technique is initiated by computing an equivalent aperture electric field excitation, \overline{E}^A , which will produce the electric current, $-\overline{J}_0^A$, with the aperture short-circuited. When the slot and wire are uncoupled (β = 90°), \overline{E}^A is found by treating the slot as a multiport generalized system [13], [20] and then inverting the system equation:

$$[\bar{J}^{A}] = [\bar{\bar{Y}}^{A}] [\bar{E}^{A}] \tag{30a}$$

where

 $[\bar{\bar{Y}}^A]$ = slot generalized admittance matrix.

When the wire is oriented such that $\beta \neq 90^{\circ}$, there is significant interaction between the wire and slot. For this interesting case, the multiport generalized system matrix of Equation 30a must be modified [13], [20], [28] according to Figure 39, yielding

$$[\bar{J}^{A}] = \left[[\bar{\bar{Y}}^{A}] + [\bar{\bar{Y}}^{A}_{w}] \right] [\bar{E}^{A}_{w}]$$
(30b)

where

 $[\bar{Y}_{W}^{A}]$ = mutual generalized admittance matrix at the slot due to the presence of the wire (accounts for wire coupling; also known as the wire admittance loading matrix or transfer admittance matrix [28]).

and

 $[\tilde{E}_{w}^{A}]$ = slot equivalent electric field excitation in the presence of the wire scatterer.

For the simple canonical slot-wire geometry the calculation of the $\begin{bmatrix} \bar{Y}_{\mathbf{W}}^{\mathbf{A}} \end{bmatrix}$ is straightforward [13] and in fact can be written in a closed form for very long wire scatterers [28].

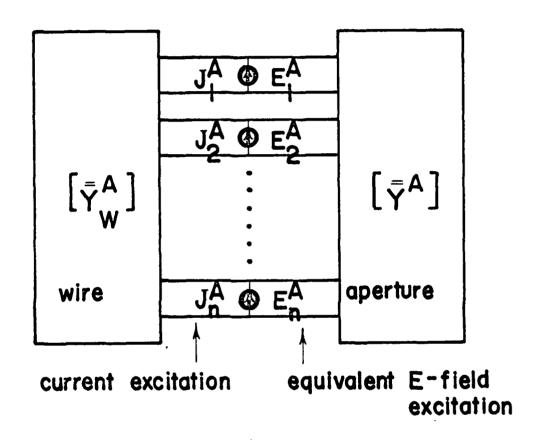


Fig. 39. MULTIPORT GENERALIZED NETWORK REPRESENTATION FOR HYBRIDING THE METHOD OF MOMENTS TECHNIQUE

The hybrid matrix Equation 30b has been solved for $\beta=0^\circ$ in the canonical geometry of Figure 36, and the computed results for the slot distribution are plotted in Figure 37. Excellent agreement with the direct method-of-moments solution is seen. The equivalent aperture electric field excitation radiates in the presence of the screen, and electric currents I (ζ) are induced on the wire by mutual coupling interaction. In Figure 38, the computed electric current induced on the wire (based on the hybrid formulation)) is plotted. Again, excellent agreement with the results obtained for the direct method-of-moments case is seen.

Therefore, it is concluded that it is valid to apply Schelkunoff's third equivalence theorem [23] for apertures having wires closely coupled to them. It has been demonstrated that the MOM / MOM hybrid approach is capable of dealing with such loaded apertures if the mutual interaction between the wire and the aperture is rigorously taken into account. The next section will present results that strongly indicate that the MOM / FD-TD hybrid technique is also valid and, in fact, even <u>much more useful</u> for complex, loaded cavities than MOM / MOM because there is no need to set up and solve for mutual interactions of the cavity contents and the apertures, as in Equation 30b.

7.4 Case Studies: MOM / FD-TD Hybrid Technique

In this section, three case studies are reported regarding the validity of the MOM / FD-TD hybrid technique: 1) Open-ended cylinder, axial incidence; 2) Open-ended cylinder, oblique (θ = 45°, ϕ = 0°) incidence, TM polarization; and 3) Loaded missile guidance section, axial incidence. The results clearly indicate that this hybrid technique is valid and useful for these and similar structures.

7.4.1 Case 1: Open-Ended Cylinder, Axial Incidence

The MOM / FD-TD hybrid model for the axial-incidence, open-ended aluminum cylinder (19 cm diameter and 68.5 cm long, as shown in Figures 40 and 41) was run for 800 time steps (2.0 cycles of the incident wave at $f=300\ \text{MHz}$). The excitation consisted of moment-method data derived by D. Wilton and A. Glisson ([9] and Appendix A) for the electric currents over the aperture locus when shorted, as specified by Schelkunoff's third theorem. The results were contour-mapped and compared to previous purely FD-TD results obtained in RADC

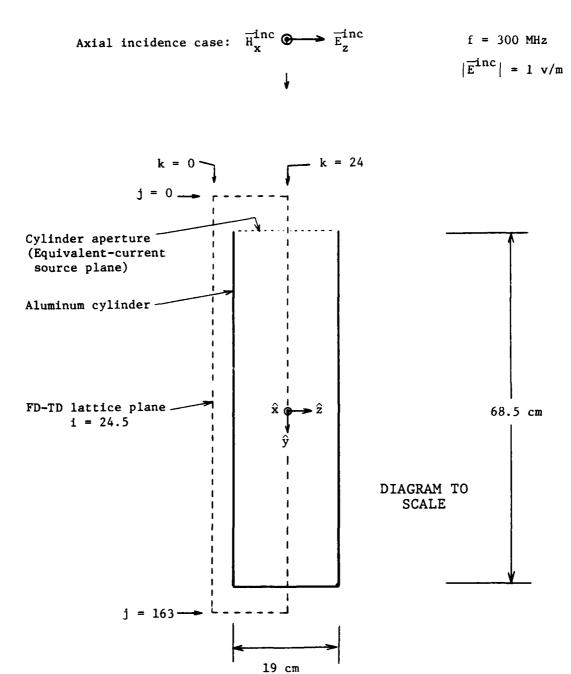


Fig. 40. VIEW OF MOM/FD-TD HYBRID CYLINDER MODEL AT FD-TD LATTICE PLANE i = 24.5 FOR AXIAL INCIDENCE CASE (CASE NO. 1)

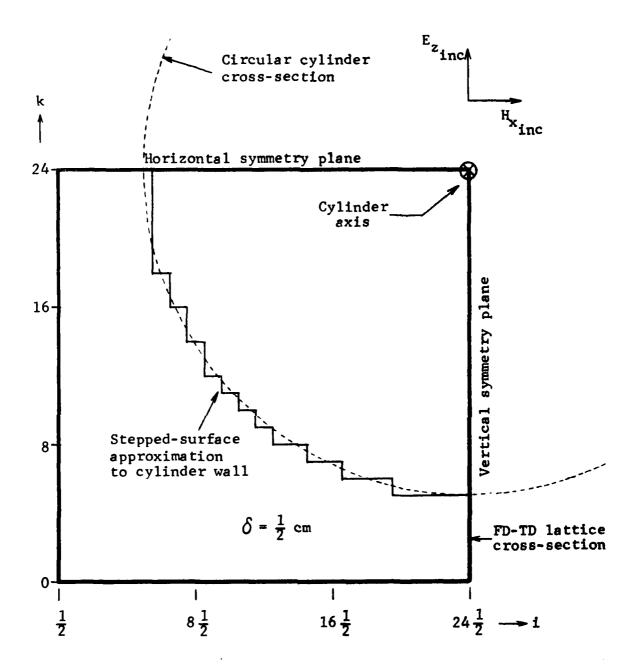


Fig. 41. CROSS-SECTION OF CYLINDER MODEL FOR MOM/FD-TD HYBRID CASE NO. 1

Contract F30602-77-C-0163.

Figure 42 plots the comparison of the pure FD-TD results for the radial electric field along the cylinder axis with the pure moment-method results of D. Wilton and A. Glisson [9]. It is seen that the results agree within 1 dB up to 20 cm back from the aperture. Beyond this point, the FD-TD results had not quite converged after 800 time steps.

Figure 43 plots the comparison of the pure FD-TD results for the radial electric field along the cylinder axis with the hybrid MOM / FD-TD program. It is seen that the results agree within 2 dB up to 40 cm back from the aperture.

Figures 44 to 49 compare the computed field contours in the cylinder horizontal and vertical symmetry planes (as defined by Figure 41) within 11 cm of the aperture. Excellent agreement is seen for all contours in the horizontal plane, and for the H_X contours in the horizontal plane. Some contour distortion and displacement is seen for the E_Z and E_Y contours of the vertical plane.

Figure 50 and 51 plot the field contours computed by the hybrid program within 35 cm of the aperture. These may be compared to Figures 18 and 17, respectively, of Report RADC-TR-78-142 obtained by the pure FD-TD approach.

The result of these comparisons is the conclusion that the MOM / FD-TD hybrid approach yields data for this case (a 0.19 λ circular aperture in an elongated cylinder) that are consistent with previous data derived from both pure MOM and pure FD-TD methods. This is a significant agreement of three computational techniques based upon very different first principles.

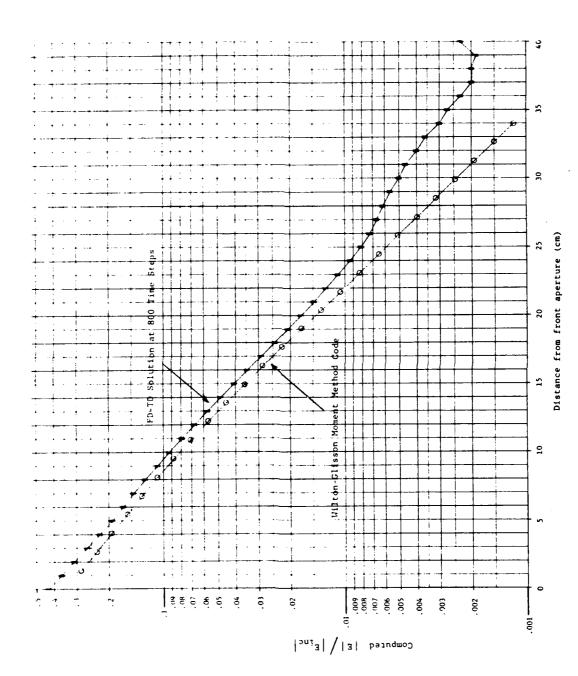


Fig. 42, COMPARISON OF COMPUTED RADIAL ELECTRIC FIELD DISTRIBUTION ALONG AXIS OF CYLINDER

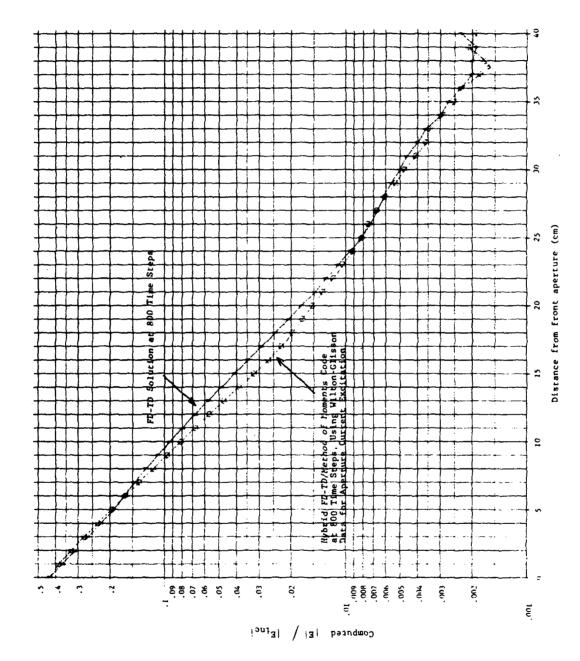


Fig. 43. COMPARISON OF COMPUTED RADIAL ELECTRIC FIELD DISTRIBUTION ALONG AXIS OF CYLINDER

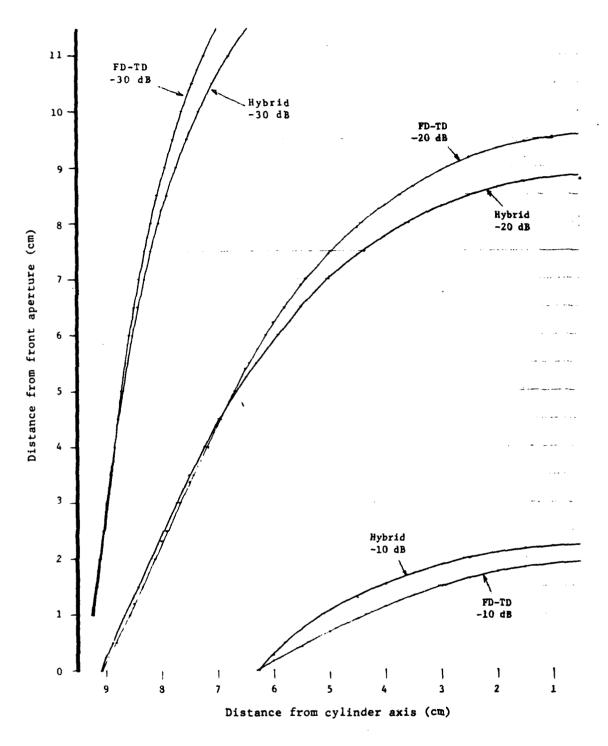


Fig. 44. COMPARISON OF COMPUTED $\mathbf{E}_{\mathbf{Z}}$ CONTOURS IN HORIZONTAL SYMMETRY PLANE

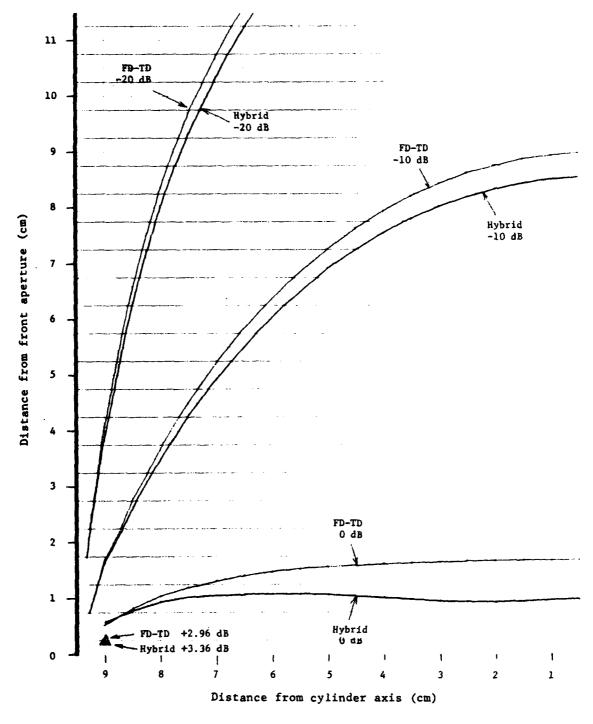


Fig. 45. COMPARISON OF COMPUTED H_x CONTOURS IN HORIZONTAL SYMMETRY PLANE

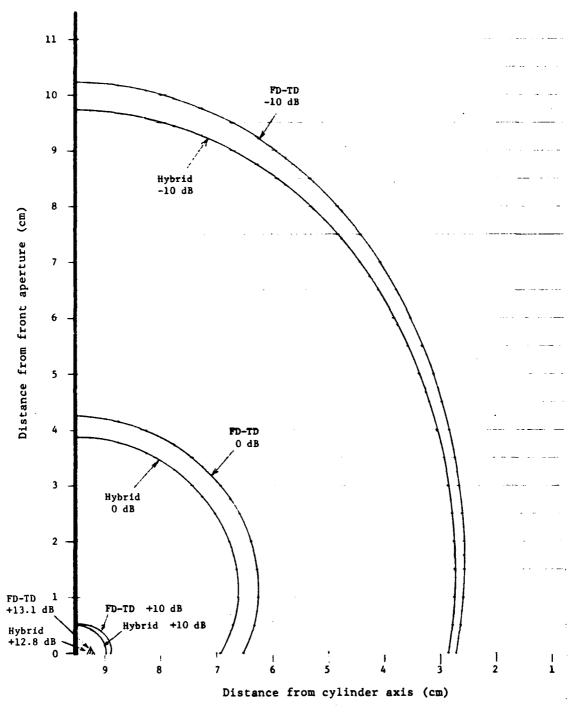


Fig. 46. COMPARISON OF COMPUTED H_y CONTOURS IN HORIZONTAL SYMMETRY PLANE

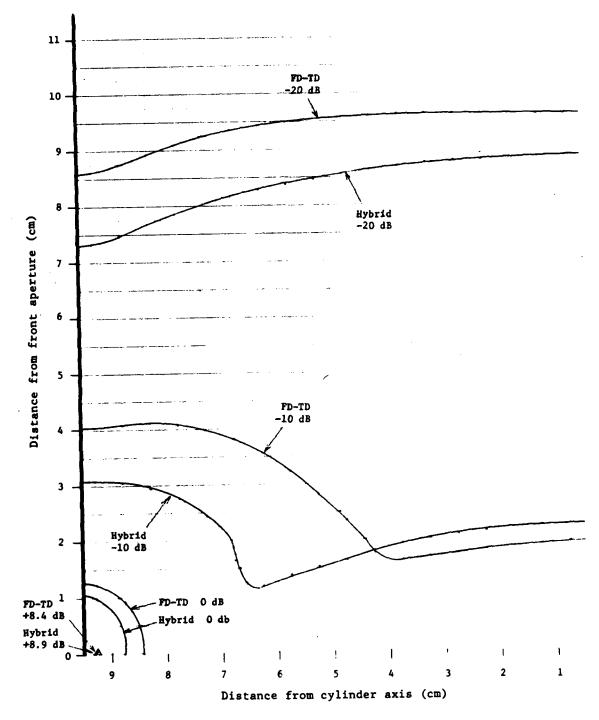


Fig. 47. COMPARISON OF COMPUTED E₂ CONTOURS IN VERTICAL SYMMETRY PLANE

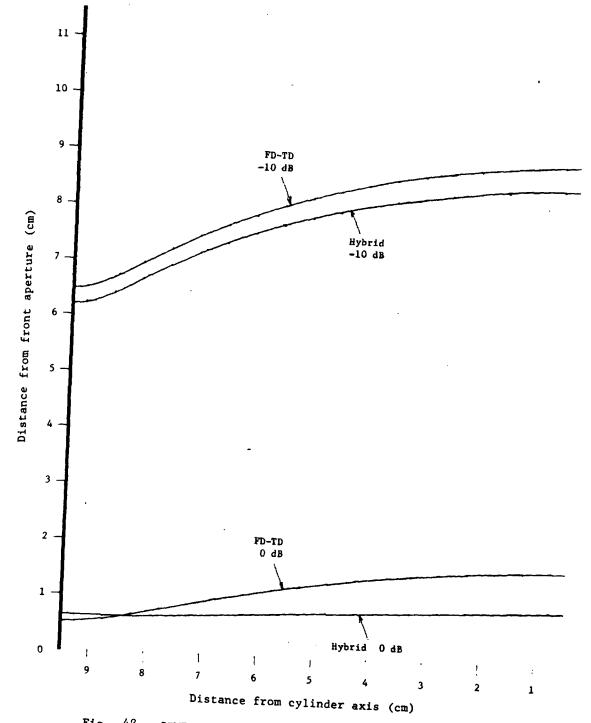


Fig. 48. COMPARISON OF COMPUTED $H_{\mathbf{x}}$ CONTOURS IN VERTICAL SYMMETRY PLANE

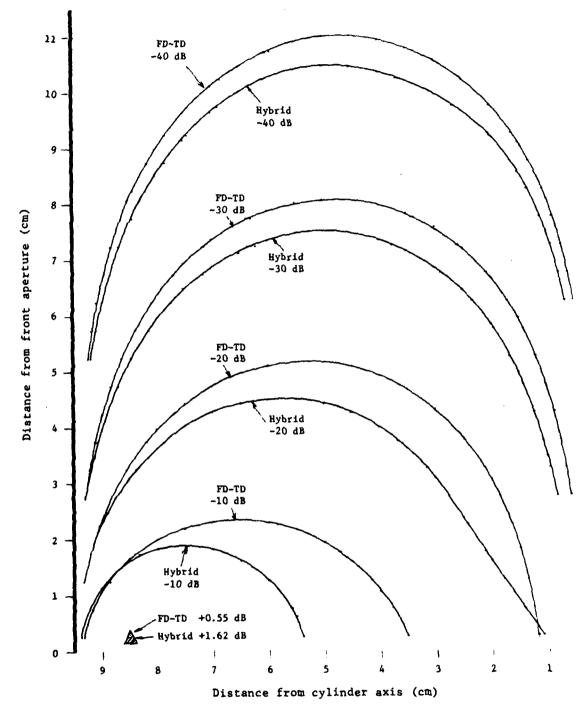


Fig. 49. COMPARISON OF COMPUTED E_y CONTOURS IN VERTICAL SYMMETRY PLANE

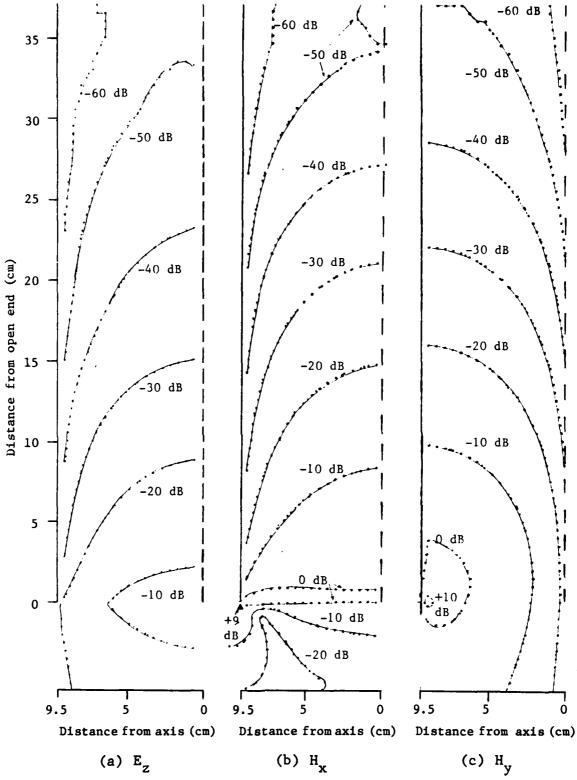


Fig. 50. COMPUTED FIELD CONTOURS IN CYLINDER HOR. SYMMETRY PLANE

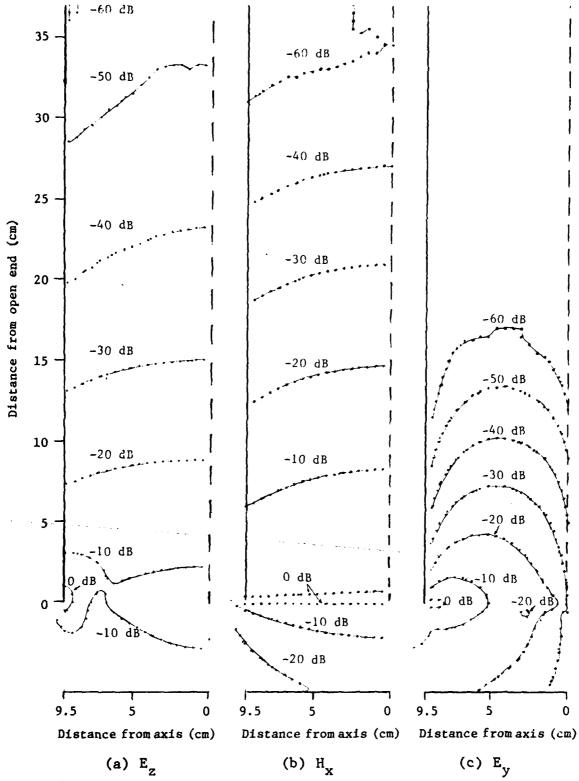


Fig. 51. COMPUTED FIELD CONTOURS IN CYLINDER VERT. SYMMETRY PLANE

7.4.2 Case 2: Open-Ended Cylinder, Oblique Incidence, TM Polarization

The MOM / FD-TD hybrid model for the oblique-incidence (45°), TM polarized case of the open-ended aluminum cylinder (as shown in Figures 52 and 53) was run for 800 time steps (2.0 cycles of the incident wave at f = 300 MHz). The excitation consisted of moment-method data derived by D. Wilton and A. Glisson ([9] and Appendix a) for the electric currents over the aperture locus when shorted, as specified by Schelkunoff's third theorem. The results were compared to pure MOM results in an attempt to establish validity of the MOM / FD-TD hybrid model for this case.

Figure 54 plots the comparison of the hybrid MOM / FD-TD results for the axial electric field within the cylinder along the cylinder axis with the pure moment-method results of D. Wilton and A. Glisson [9]. It is seen that the results agree within 2.5 dB in the span 3 cm - 25 cm back of the aperture. This is nearly the same level of agreement observed in Figures 42 and 43 for the axial-incidence case. This implies that arbitrary angles of wave incidence could be treated using the hybrid MOM / FD-TD method simply by specifying the proper aperture equivalent current excitation, without having to change the FD-TD geometry of the cylinder (a considerably more complicated task).

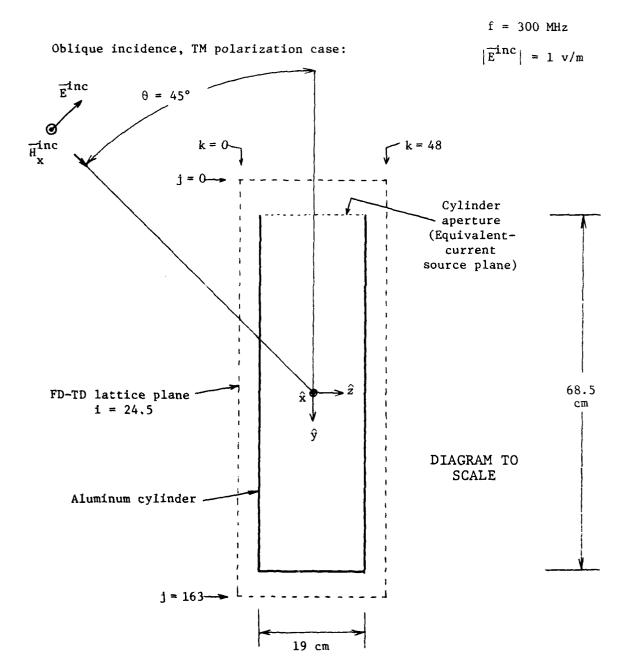


Fig. 52. VIEW OF MOM/FD-TD HYBRID CYLINDER MODEL AT FD-TD LATTICE PLANE i = 24.5 FOR OBLIQUE INCIDENCE,
TM POLARIZATION CASE (CASE NO. 2)

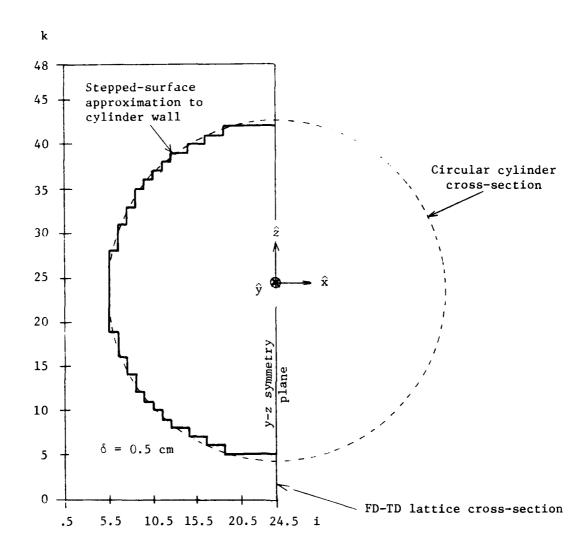


Fig. 53. CROSS-SECTION OF CYLINDER MODEL FOR MOM/FD-TD HYBRID CASE NO. 2

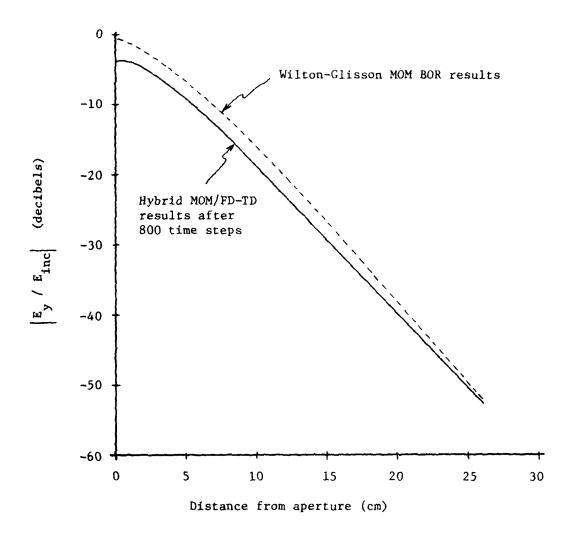


Fig. 54. COMPARISON OF RESULTS FOR THE AXIAL ELECTRIC FIELD WITHIN THE CYLINDER, 45°/TM INCIDENCE CASE

7.4.3 Case 3: Loaded Missile Guidance Section, Axial Incidence

The MOM / FD-TD hybrid model for the axial-incidence case of the loaded guidance section (as shown in Figures 55 and 24-26) was run for 1800 time steps (3.0 cycles of the incident wave at f=300~MHz). The excitation consisted of moment-method data derived by D. Wilton and A. Glisson ([9] and Appendix A) for the electric currents over the aperture and sleeve-fitting loci when shorted, as specified by Schelkunoff's third theorem. The results were compared to pure FD-TD results presented in Section 4.2 of this report in an attempt to establish the consistency of the MOM / FD-TD hybrid model for this case.

Figure 56 plots the comparison of the hybrid MOM-FD-TD results for the H field contours in the vertical symmetry plane with the pure FD-TD results already presented in Figure 28. It is seen that, for both methods stepped to 1800 time steps, there is an excellent agreement of the 0 dB contours near the wire connecting the cooled detector unit to the pre-amp can. For this contour, the maximum spatial shift is only about 0.16 cm in a direction further out from the wire. Further, there is observed to be excellent agreement of the +10 dB contour near the wire connecting the pre-amp can to the metal backplane. For this contour, the maximum spatial shift is only about 0.1 cm in a direction further out from the wire. This implies that the currents in these two major wires are predicted to be almost the same by both the pure FD-TD method and the hybrid MOM / FD-TD method, following the discussion of Section 5 of this report.

Figures 57 and 58 plot the comparison of the hybrid NCM / FD-TD results for the $\rm H_X$ and $\rm E_Z$ fields along a vertical cut through the center of the guidance section at a point 21 cm in back of the nose aperture (about 2 cm in front of the sleeve fitting, at the point where the circumferential slot opens into the interior of the nose cone). The hybrid run results are after 1500 time steps, while the pure FD-TD results are after 1800 time steps. For this case, a very high level of agreement is observed between the two sets. Of data at all points of comparison. The worst-case difference between the results is only 1 dB, with most results consistent within only fractions of

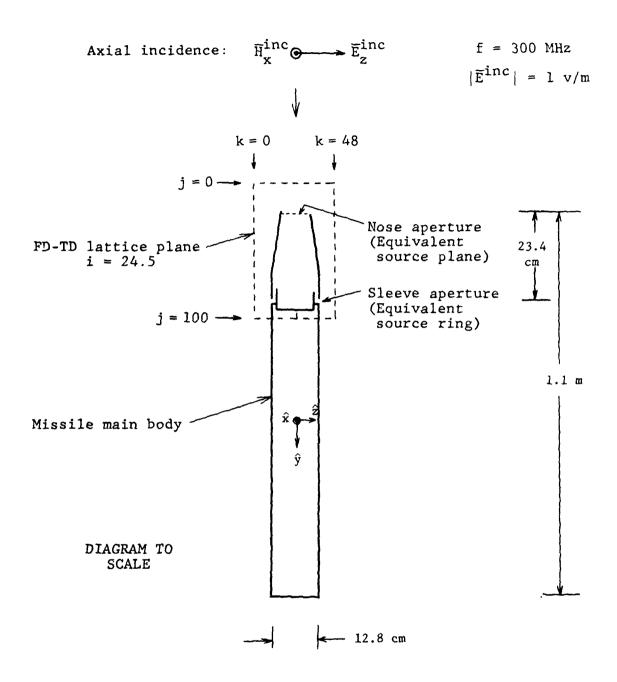


Fig. 55. VIEW OF MOM/FD-TD MISSILE GUIDANCE SECTION MODEL
AT FD-TD LATTICE PLANE i = 24.5 FOR AXIAL
INCIDENCE (CASE NO. 3)

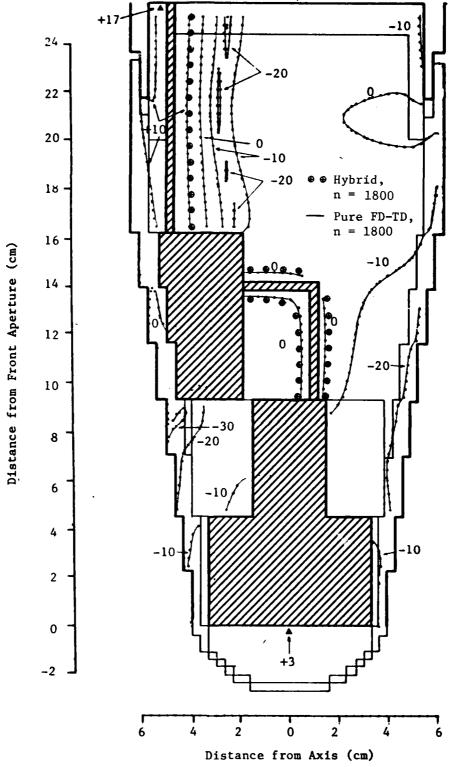


Fig. 56. COMPARISON OF COMPUTED $H_{\mathbf{x}}$ CONTOURS IN NOSE CONE VERTICAL SYM. PLANE

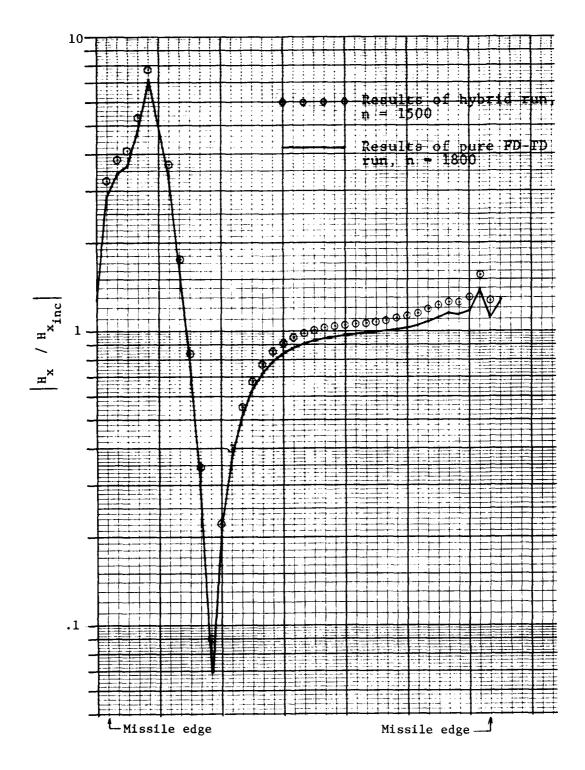


Fig. 57. COMPARISON OF COMPUTED $H_{\mathbf{x}}$ FIELD ALONG A VERTICAL CUT THROUGH THE NOSE CONE AT THE SLEEVE FITTING

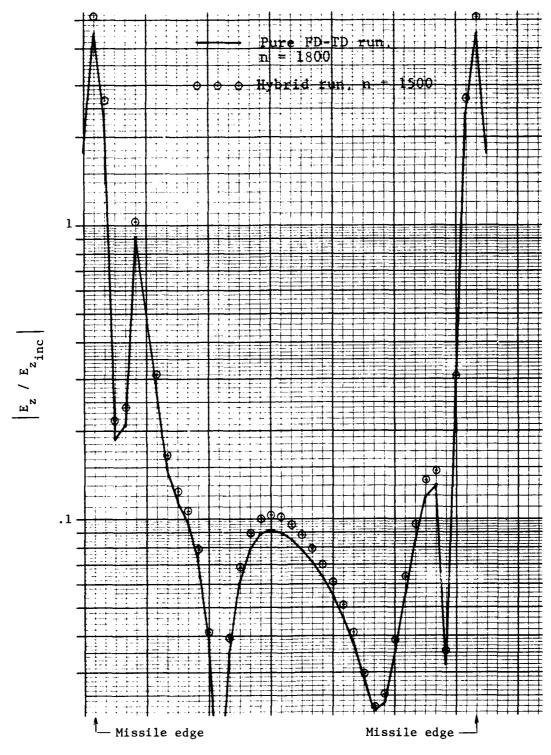


Fig. 58. COMPARISON OF COMPUTED $\mathbf{E_{Z}}$ FIELD ALONG A VERTICAL CUT THROUGH THE NOSE CONE AT THE SLEEVE FITTING

of a decibel. (Comparison of the data sets for the 1800 time-step case for each set results in slightly lessened agreement, such that the worst-case difference is about 1.7 dB. This may result from the hybrid program progressing to the sinusoidal steady state at a slightly faster rate than the pure FD-TD program, since a sinusoidal steady-state equivalent aperture current excitation is employed from the very beginning of the hybrid program, rather than an aperture excitation which must build to the steady state.)

This case study leads to the following observations and conclusions:

- The hybrid MOM / FD-TD approach yields results for the missile guidance section wire currents and electromagnetic fields which are consistent with the pure FD-TD data.
- 2. For the axial-incidence case, the assumption in Section 4 of this report that the finite length of the missile has little effect on the guidance section fields is shown to be valid, since the hybrid case aperture excitation does take into account the missile length, and its results are consistent with those of Section 4.
- 3. A wire passing very close to an aperture, and strongly coupled to that aperture (as for the case of the pre-amp can-to-backplane wire near the sleeve-fitting aperture) can be consistently modeled using the pure FD-TD approach and the hybrid MOM / FD-TD approach. In the latter, it must be remembered that the MOM-derived equivalent aperture excitation takes into account <u>none</u> of the interior details of the structure.
- 4. Complex sub-sections of elongated simply-shaped structures are prime candidates for detailed modeling of the interior penetrating fields via the hybrid MOM / FD-TD method.
- 5. MOM-derived sinusoidal steady-state equivalent aperture excitations can be easily interpreted to provide input data for the FD-TD method.

8.0 DISCUSSION AND CONCLUSIONS

This research program demonstrated that the FD-TD method can be successfully applied to electromagnetic coupling problems involving highly-conducting structures with hole and sleeve-type apertures illuminated by a plane wave having an arbitrary polarization and angle of incidence. Further, the FD-TD method can be applied to complex cavity-like structures having internal metal and dielectric materials, as well as connecting wires. Accuracy of the FD-TD results was very good relative to the uncertainties of avilable experimental and numerical-theory approaches. Convergence of the electromagnetic fields to the sinusoidal steady state occurred within about 3 cycles of the incident wave when a slight value of isotropic conductivity was assigned to the interior of the structures modeled. This resulted in program central processor times of less than 5 minutes for FD-TD lattices containing as many as 1.5 million unknowns time-stepped to $n_{\text{max}} = 800$ using the Control Data STAR-100 and Cyber 203 computers.

This research program also established the feasibility of a hybrid MOM / FD-TD analysis technique based upon the use of Schelkunoff's equivalent current theorem at apertures of a cavity. This hybrid technique was shown to give consistent results for structures illuminated at both oblique and axial incidence by plane waves. Further, this technique was shown to give consistent results for apertures strongly coupled to internal wires or other metal and dielectric structures.

The pure FD-TD and hybrid MOM / FD-TD methods appear to have great promise for applications involving complex conducting and dielectric structures illuminated by plane waves at arbitrary angles of incidence and polarization. Further, great promise is shown for those structures that are simultaneously electrically large compared to a wavelength and penetrated by locally complex cavity-backed apertures having dimensions comparable to a wavelength. Such structures requiring resolution of both large and small details at the same time have not been well treated by any one previous analytical or numerical approach.

REFERENCES

- [1] K. S. Yee, "numerical Solution of Initial Boundary Value Problems Involving Maxwell's Equations in Isotropic Media," <u>IEEE Trans.</u>

 Antennas Prop., vol. AP-14, pp. 302-307, May 1966.
- [2] E. K. Miller and A. J. Poggio, "Moment-Method Techniques in Electromagnetics from an Applications Viewpoint," Chapter 9 in Electromagnetic Scattering, P.L.E. Uslenghi, ed., Academic Press, New York, 1978.
- [3] C. D. Taylor, D.-H. Lam, and T. H. Shumpert, "Electromagnetic Pulse Scattering in Time-Varying Inhomogeneous Media," <u>IEEE Trans. Antennas Prop.</u>, vol. AP-17, pp. 585-589, Sept. 1969.
- [4] D. E. Merewether, "Transient Currents Induced on a Metallic Body of Revolution by an Electromagnetic Pulse," IEEE Trans. Electromag. Compat., vol. EMC-13, pp. 41-44, May 1971.
- [5] R. Holland, "Threde: A Free-Field EMP Coupling and Scattering Code," IEEE Trans. Nuclear Science, vol. NS-24, pp. 2416-2421, December 1977.
- [6] A. Taflove and M. E. Brodwin, "Numerical Solution of Steady-State Electromagnetic Scattering Problems Using the Time-Dependent Maxwell's Equations," IEEE Trans. Microwave Theory Tech., vol. MTT-23, pp. 623-630, August 1975.
- [7] A. Taflove and M. E. Brodwin, "Computation of the Electromagnetic Fields and Induced Temperatures Within a Model of the Microwave-Irradiated Human Eye," <u>IEEE Trans. Microwave Theory Tech.</u>, vol. MTT-23, pp. 888-896, November 1975.
- [8] A. Taflove, "Time Domain Solutions for Electromagnetic Coupling," Final Rep. RADC-TR-78-142, Contract No. F30602-77-C-0163, Rome Air Development Center, Griffiss AFB, Rome, NY, with IIT Research Institute, Chicago, IL, June 1978, AD# A040 772.
- [9] D. Wilton and A. Glisson, Consulting services to IIT Research Institute on Contract F30602-79-C-0039, Sept. 1979 to Feb. 1980.
- [10] S. Ramo, J. R. Whinnery, and T. Van Duzer, Fields and Waves in Communication Electronics, Sections 5.13 5.18. Wiley, New York, 1965.
- [11] K. R. Umashankar and C. E. Baum, "Transient Electromagnetic Characterization of Arbitrary Conducting Bodies Through an Aperture Perforated Conducting Screen," Interaction Note 343, March 1978.

- [12] C. E. Baum, "EMP Simulators for Various Types of Nuclear EMP Environments: An Interim Categorization," Sensor and Simulation Note 151, July 1972.
- [13] R. F. Harrington, <u>Field Computation by Moment Methods</u>, MacMillan, New York, 1968.
- [14] C. J. Bouwkamp, "Theoretical and Numerical Treatment of Diffraction Through a Circular Aperture," <u>IEEE Trans. on Antennas and Propagation</u>, AP-18, No. 2, March 1970.
- [15] K. R. Umashankar and C. M. Butler, "A Numerical Solution Procedure for Small Aperture Integral Equations," Interaction Note 212, July 1974.
- [16] D. R. Wilton and O. C. Dunaway, "Electromagnetic Penetration Through Apertures of Arbitrary Shape: Formulation and Numerical Solution Procedure," Interaction Note 214, July 1974.
- [17] D. R. Wilton, C. M. Butler, and K. R. Umashankar, "Penetration of Electromagnetic Fields Through Small Apertures in Planar Screens: Selected Data," Interaction Note 213, September 1974.
- [18] C. M. Butler and K. R. Umashankar, "Electromagnetic Penetration Through an Aperture in an Infinite Planar Screen Separating Two Half Spaces of Different Electromagnetic Properties," <u>Radio Science</u>, Vol. II, No. 7, July 1976.
- [19] T.B.A. Senior and G. A. Desjardins, "Field Penetration into a Spherical Cavity," Interaction Note 142, August 1973.
- [20] H. K. Schumann and D. E. Warren, "Aperture Coupling in Bodies of Revolution," <u>IEEE Transactions on Antennas and Propagation</u>, Vol. AP-26, No. 6, November 1978.
- [21] K. R. Umashankar and J. R. Wait, "Electromagnetic Coupling in an Infinite Cable Placed Behind a Slot Perforated Screen," Interaction Note 330, June 1977.
- [22] C. M. Butler and K. R. Umashankar, "Electromagnetic Excitation of a Wire Through an Aperture Perforated Conducting Screen," Interaction Note 251, July 1975.
- [23] S. A. Schelkunoff, "Field Equivalence Theorems," <u>Comm. Pure Appl.</u> Math., Vol. 4, pp. 43-59, June 1951.
- [24] R. F. Harrington and J. R. Mautz, "Green's Functions for Surfaces of Revolution," Radio Science, Vol. 7, No. 5, pp. 603-611, May 1972.

- [25] J. R. Mautz and R. F. Harrington, "Radiation and Scattering from Bodies of Revolution," Appl. Sci. Res., No. 20, pp. 405-435, 1969.
- [26] A. W. Glission and D. R. Wilton, "Simple and Efficient Numerical Techniques for Treating Bodies of Revolution," RADC-TR-79-22 report, March 1979, AD# 067 361.
- [27] C. M. Butler and K. R. Umashankar, "Electromagnetic Excitation of a Wire Through an Aperture Perforated Conducting Screen," IEEE Transactions on Antennas and Propagation, Vol. 24, No. 4, pp. 456-462, July 1976.
- [28] K. R. Umashankar and J. R. Wait, "Electromagnetic Coupling in an Infinite Cable Placed Behind a Slot Perforated Screen," IEEE Transactions on Electromagnetic Compatibility, Vol. EMC 20, No. 3, pp. 406-411, August, 1978.

APPENDIX A

Analytical and Numerical Formulation of the Perfectly Conducting Body of Revolution

This appendix summarizes the analytical formulation and the MOM numerical procedure to treat scattering by perfectly conducting bodies of revolution [24] - [26]. Due to the symmetry of such structures, the incident plane-wave excitation and corresponding induced electric current distribution are expanded in terms of a sum of Fourier modes to reduce the coupled integrodifferential equation to a simpler modal generalized matrix. This matrix can then be solved for every mode excited on the body of revolution.

I. Integral Equation: Coupled Form

The geometry of a perfectly conducting body of revolution is shown in Figure A-1. It is placed in a homogeneous free space medium of permeability, μ_0 , permittivity, ϵ_0 , and conductivity, σ_0 = 0. The z coordinate axis of the $(\rho,\,\phi,\,z)$ coordinate system coincides with the axis of the body of revolution. P' is a point $(\rho',\,\phi',\,z')$ on the surface of the body of revolution with \hat{t}' and \hat{n}' unit tangential and normal vectors. The unit tangential vector, \hat{t}' , makes an angle, γ' , with the z axis. Throughout the analysis, $\hat{\phi}$ = \hat{t} x \hat{n} (right hand system) is assumed.

Let $[E^{i}(\vec{r}), H^{i}(\vec{r})] = \text{external incident plane wave}$ $\overrightarrow{J(r)} = \text{induced surface electric current}$ $\overrightarrow{distribution}$ $[E^{S}(\vec{r}), H^{S}(\vec{r})] = \text{scattered electric field}$

On the surface of the body of revolution S, the following boundary condition is satisfied,

$$\hat{n} \times \hat{E}^{\dagger}(\hat{r}) = -\hat{n} \times \hat{E}^{S}(\hat{r}), \quad \hat{r} \in \text{on } S$$
 (A-1)

Further, the scattered electric and magnetic fields are given by

$$\vec{E}^{S}(\vec{r}) = -j\omega \vec{A}(\vec{r}) - \nabla \Phi(\vec{r})$$
 (A-2a)

$$\overrightarrow{H}^{S}(\overrightarrow{r}) = \frac{1}{\mu_{0}} \nabla \times \overrightarrow{A}(\overrightarrow{r})$$
 (A-2b)

where the magnetic vector potential $\vec{A}(\vec{r})$ and the scalar potential $\phi(\vec{r})$ can be expressed in terms of the surface electric currents and charges on the body of revolution:

$$\stackrel{\rightarrow}{A}(\vec{r}) = \frac{\mu_0}{4\pi} \iint_S \vec{r}' \vec{r}' G(\vec{r}, \vec{r}') ds' \qquad (A-3a)$$

$$\phi(\vec{r}) = \frac{1}{4\pi\epsilon_0} \iint_S \rho^e(\vec{r}') G(\vec{r}, \vec{r}') ds'$$
 (A-3b)

where the free-space Green's function is

$$G(\vec{r}, \vec{r}') = \underline{e^{-jkR}}$$
(A-3c)

$$R = [\rho^{2} + \rho'^{2} - 2 \rho \rho' \cos (\phi - \phi') + (z - z')^{2}]^{\frac{1}{2}}$$
 (A-3d)

$$k = \omega(\mu_0 \varepsilon_0)^{\frac{1}{2}}.$$
 (A-3e)

In Equation A-3c, k is the propagation constant in the free space medium, and ω is the frequency of the incident excitation in radians/sec. In obtaining Equations A-2 and A-3, the field quantities are assumed to have an $e^{j\omega t}$ time dependence. Hence, on substituting Equations A-2 and A-3 into the boundary condition of Equation A-1, the following integro-differential equation is obtained:

$$\hat{\mathbf{n}} \times \vec{\mathbf{E}}^{\dagger}(\vec{\mathbf{r}}) = \hat{\mathbf{n}} \times \begin{bmatrix} \mathbf{j}\omega\mu_{0} \\ 4\pi \end{bmatrix} \int_{S} \vec{\mathbf{J}}(\vec{\mathbf{r}}') G(\vec{\mathbf{r}}, \vec{\mathbf{r}}') ds' + \frac{\mathbf{j}}{4\pi\omega\epsilon_{0}} \nabla \iint_{S} \rho^{e}(\vec{\mathbf{r}}') G(\vec{\mathbf{r}}, \vec{\mathbf{r}}') ds' \end{bmatrix},$$

in which we can replace the charge distribution by

$$\rho^{\mathbf{e}(\vec{r}')} = \frac{\mathbf{j}}{\omega} \left[\nabla_{\mathbf{s}}' . \mathbf{J}(\vec{r}') \right] \tag{A-5}$$

(A-4)

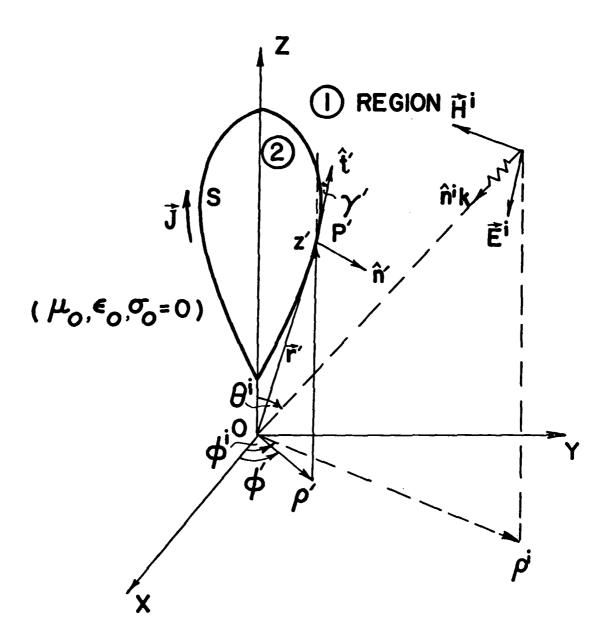


Fig. A-1. GEOMETRY OF PERFECTLY CONDUCTING BODY OF REVOLUTION

In Equation A-4, the unknown electric current distribution $J(\vec{r})$, can be split into two orthogonal components along \hat{t} and $\hat{\phi}$ to utilize the symmetry of the structure in the ϕ coordinate variable. Similarly, the incident field can be resolved into two orthogonal components. This gives:

$$\hat{n} \times \vec{J}(\vec{r}) = \hat{t} J_{t}(\vec{r}) + \hat{\phi} J_{\phi}(\vec{r})$$
 (A-6a)

$$\hat{\mathbf{n}} \times \hat{\mathbf{E}}^{\dot{\mathbf{i}}}(\hat{\mathbf{r}}) = \hat{\mathbf{t}} \, \mathbf{E}_{\dot{\mathbf{t}}}^{\dot{\mathbf{i}}}(\hat{\mathbf{r}}) + \hat{\boldsymbol{\phi}} \, \mathbf{E}_{\dot{\boldsymbol{\phi}}}^{\dot{\mathbf{i}}}(\hat{\mathbf{r}}) \tag{A-6b}$$

where the unit vectors are given by

$$\hat{t} = \sin \gamma \cos \phi \hat{x} + \sin \gamma \sin \phi \hat{y} + \cos \gamma \hat{z}$$
 (A-7a)

$$\hat{n} = \cos \gamma \cos \phi \hat{x} + \cos \gamma \sin \phi \hat{y} - \sin \gamma \hat{z}$$
 (A-7b)

$$\hat{\phi} = -\sin \phi \hat{x} + \cos \phi \hat{y}$$
 (A-7c)

Hence, separating the \hat{t} and $\hat{\phi}$ components of Equation A-4 gives the following two coupled integral equations:

$$E_{t}^{i}(\vec{r}) = L_{11} (J_{t}) + L_{12} (J_{\phi})$$
 (A-8a)

$$E_{t}^{i}(\vec{r}) = L_{21} (J_{t}) + L_{22} (J_{\phi})$$
 (A-8b)

where L_{mn} is an operator given by the integral expressions

$$L_{11} (J_{t}) = \frac{j\omega\mu_{0}}{4\pi} \iint_{S} J_{t}(\vec{r}') [\hat{t}\cdot\hat{t}'] G(\vec{r}, \vec{r}') ds'$$

$$+ \frac{j}{4\pi\omega\epsilon_{0}} \frac{\partial}{\partial t} \iint_{S} \left\{ \frac{1}{\rho'} \frac{\partial}{\partial t'} [\rho'J_{t}(\vec{r}')] \right\} G(\vec{r}, \vec{r}') ds' \qquad (A-8c)$$

$$L_{12}(J_{\phi}) = \frac{j\omega\mu_0}{4\pi} \iint_{S} J_{\phi}(\vec{r}') [\hat{t} \cdot \hat{\phi}] G(\vec{r}, \vec{r}') ds'$$

$$+ \frac{j}{4\pi\omega\epsilon_0} \frac{\partial}{\partial t} \iiint_{S} \left[\frac{1}{\rho'} \frac{\partial}{\partial \phi'} \left[J_{\phi}(\vec{r}') \right] \right] G(\vec{r}, \vec{r}') ds'$$
 (A-8d)

$$L_{21} (J_{t}) = \frac{j\omega\mu_{0}}{4\pi} \iint_{S} J_{t} (\vec{r}') \left[\hat{\phi} \cdot \hat{t}'\right] G(\vec{r}, \vec{r}') ds'$$

$$+ \frac{j}{4\pi\omega\epsilon_{0}\rho} \frac{\partial}{\partial\phi} \iint_{S} \left[\hat{\rho}' \frac{\partial}{\partial t'} \left[\rho' J_{t}(\vec{r}')\right]\right] G(\vec{r}, \vec{r}') ds' \qquad (A-8e)$$

$$L_{22} (J_{\phi}) = \frac{j\omega\mu_{0}}{4\pi} \iint_{S} J_{\phi}(\vec{r}') \left[\hat{\phi} \cdot \hat{\phi}'\right] G(\vec{r}, \vec{r}') ds'$$

$$+ \frac{j}{4\pi\omega\epsilon_{0}\rho} \frac{\partial}{\partial\phi} \iint_{S} \left[\hat{\rho}' \frac{\partial}{\partial\phi'} \left[J_{\phi}(\vec{r}, \vec{r}')\right]\right] G(\vec{r}, \vec{r}') ds' \qquad (A-8f)$$

where

$$\hat{t} \cdot \hat{t} = \sin \gamma \sin \gamma' \cos (\phi' - \phi) + \cos \gamma \cos \gamma'$$
 (A-8g)

$$\hat{t} \cdot \hat{t} - \sin \gamma \sin (\phi' - \phi)$$
 (A-8h)

$$\hat{\phi} \cdot \hat{\mathbf{t}}' = \sin \gamma' \sin (\phi' - \phi) \tag{A-8i}$$

$$\hat{\phi} \cdot \hat{\phi}' = \cos(\phi' - \phi) \tag{A-8j}$$

II. Modal Form of Equations

The ϕ symmetry of the body of revolution can be utilized to reduce the double integral of Equations A-8c to A-8f to single integrals by performing first the integration with respect to the ϕ' variable. For this, the kernel function $G(\vec{r}, \vec{r}')$ is expanded in a Fourier series as follows:

$$G(\phi - \phi') = \frac{1}{2\pi} \sum_{m=-\infty}^{\infty} G_m e^{jm(\phi - \phi')}$$
(A-9a)

where

$$G_{m} = G_{-m} = \int_{-\pi}^{\pi} G(\xi) \cos(m\xi) d\xi \qquad (A-9b)$$

in which $G(\xi)$ is evaluated on the surface S,

$$G(\xi) = \frac{e^{-jkR_0}}{R_0}$$
 (A-9c)

$$R_{0} = [\rho^{2} + \rho'^{2} - 2\rho\rho' \cos \xi + (z-z')^{2}]^{\frac{1}{2}}$$
 (A-9d)

Further, Equation A-9a yields

$$\cos (\phi - \phi') G(\phi - \phi') = \sum_{m=-\infty}^{\infty} G_m^c e^{jm(\phi - \phi')}$$
(A-9e)

$$\sin (\phi - \phi') G(\phi - \phi') = \sum_{m=-\infty}^{\infty} G_m^s e^{jm(\phi - \phi')}$$
 (A-9f)

where

$$G_{m}^{c} = \left[\frac{G_{m-1}}{2} + \frac{G_{m+1}}{2}\right]$$
 (A-9g)

$$G_{m}^{S} = \left[\frac{G_{m-1}}{2j} - \frac{G_{m+1}}{2j}\right]$$
 (A-9h)

The Fourier expansions of Equations A-9a, A-9e, and A-9f are now substituted into the integrals of Equations A-8a and A-8b. These equations are then tested on both sides with respect to the ϕ -coordinate variable on the body of revolution by multiplying throughout by $e^{-jp\varphi}$ and integrating between the limits $-\pi$ to π . The following integral equations are obtained, with the orthogonality relationship that the integrals exist only for m=p:

$$\int_{-\pi}^{\pi} E_{t}^{i}(t, \phi) e^{-jm\phi} d\phi = L'_{11}(J_{t}) + L'_{12}(J_{\phi})$$
 (A-10a)

$$\int_{-\pi}^{\pi} E_{\phi}^{i}(t, \phi) e^{-jm\phi} d\phi = L'_{21} (J_{t}) + L'_{22} (J_{\phi})$$
 (A-10b)

where

$$\begin{split} L_{11}^{'} \; (J_{t}) &= \frac{j\omega\mu_{o}}{4\pi} \int_{t^{'}} \int_{\varphi^{'}} J_{t} \; (t^{'},\,\varphi^{'}) \; D_{m} \; e^{-jm\varphi^{'}} \; (\rho^{'}dt^{'}d\varphi^{'}) \\ &+ \frac{j}{4\pi\omega\varepsilon_{o}} \frac{\partial}{\partial t} \int_{t^{'}} \int_{\varphi^{'}} \frac{\partial}{\partial t^{'}} \left[\rho^{'}J_{t}(t^{'},\,\varphi^{'}) \right] \; G_{m}e^{-jm\varphi^{'}} \; (dt^{'}d\varphi^{'}) \\ L_{12}^{'} \; (J_{\varphi}) &= \frac{j\omega\mu_{o}}{4\pi} \int_{t^{'}} \int_{\varphi^{'}} J_{\varphi} \; (t^{'},\,\varphi^{'}) \; E_{m} \; e^{-jm\varphi^{'}} \; (\rho^{'}dt^{'}d\varphi^{'}) \\ &+ \frac{j}{4\pi\omega\varepsilon_{o}} \frac{\partial}{\partial t} \int_{t^{'}} \int_{\varphi^{'}} \frac{\partial}{\partial \varphi^{'}} \left[J_{\varphi}(t^{'},\,\varphi^{'}) \right] \; G_{m}e^{-jm\varphi^{'}} \; (dt^{'}d\varphi^{'}) \\ L_{21}^{'} \; (J_{t}) &= \frac{j\omega\mu_{o}}{4\pi\omega\varepsilon_{o}\rho} \int_{t^{'}} \int_{\varphi^{'}} \frac{\partial}{\partial t^{'}} \left[\rho^{'}J_{t}(t^{'},\,\varphi^{'}) \right] \; (jm) \; G_{m}e^{-jm\varphi^{'}} \; (dt^{'}d\varphi^{'}) \\ &+ \frac{j}{4\pi\omega\varepsilon_{o}\rho} \int_{t^{'}} \int_{\varphi^{'}} \frac{\partial}{\partial t^{'}} \left[\rho^{'}J_{t}(t^{'},\,\varphi^{'}) \right] \; (jm) \; G_{m}e^{-jm\varphi^{'}} \; (dt^{'}d\varphi^{'}) \\ &+ \frac{j}{4\pi\omega\varepsilon_{o}\rho} \int_{t^{'}} \int_{\varphi^{'}} \int_{\varphi^{'}} \frac{\partial}{\partial \varphi^{'}} \left[J_{\varphi}(t^{'},\,\varphi^{'}) \right] \; (jm) \; G_{m}e^{-jm\varphi^{'}} \; (dt^{'}d\varphi^{'}) \\ &+ \frac{j}{4\pi\omega\varepsilon_{o}\rho} \int_{t^{'}} \int_{\varphi^{'}} \frac{\partial}{\partial \varphi^{'}} \left[J_{\varphi}(t^{'},\,\varphi^{'}) \right] \; (jm) \; G_{m}e^{-jm\varphi^{'}} \; (dt^{'}d\varphi^{'}) \\ &+ \frac{j}{4\pi\omega\varepsilon_{o}\rho} \int_{t^{'}} \int_{\varphi^{'}} \frac{\partial}{\partial \varphi^{'}} \left[J_{\varphi}(t^{'},\,\varphi^{'}) \right] \; (jm) \; G_{m}e^{-jm\varphi^{'}} \; (dt^{'}d\varphi^{'}) \\ &+ \frac{j}{4\pi\omega\varepsilon_{o}\rho} \int_{t^{'}} \int_{\varphi^{'}} \frac{\partial}{\partial \varphi^{'}} \left[J_{\varphi}(t^{'},\,\varphi^{'}) \right] \; (jm) \; G_{m}e^{-jm\varphi^{'}} \; (dt^{'}d\varphi^{'}) \\ &+ \frac{j}{4\pi\omega\varepsilon_{o}\rho} \int_{t^{'}} \int_{\varphi^{'}} \frac{\partial}{\partial \varphi^{'}} \left[J_{\varphi}(t^{'},\,\varphi^{'}) \right] \; (jm) \; G_{m}e^{-jm\varphi^{'}} \; (dt^{'}d\varphi^{'}) \\ &+ \frac{j}{4\pi\omega\varepsilon_{o}\rho} \int_{t^{'}} \int_{\varphi^{'}} \frac{\partial}{\partial \varphi^{'}} \left[J_{\varphi}(t^{'},\,\varphi^{'}) \right] \; (jm) \; G_{m}e^{-jm\varphi^{'}} \; (dt^{'}d\varphi^{'}) \\ &+ \frac{j}{4\pi\omega\varepsilon_{o}\rho} \int_{t^{'}} \frac{\partial}{\partial \varphi^{'}} \left[J_{\varphi}(t^{'},\,\varphi^{'}) \right] \; (jm) \; G_{m}e^{-jm\varphi^{'}} \; (dt^{'}d\varphi^{'}) \\ &+ \frac{j}{4\pi\omega\varepsilon_{o}\rho} \int_{t^{'}} \frac{\partial}{\partial \varphi^{'}} \left[J_{\varphi}(t^{'},\,\varphi^{'}) \right] \; (jm) \; G_{m}e^{-jm\varphi^{'}} \; (dt^{'}d\varphi^{'})$$

where

$$D_{m} = \sin \gamma \sin \gamma' G_{m}^{C} + \cos \gamma \cos \gamma' G_{m}$$
 (A-10g)

$$E_{m} = \sin \gamma G_{m}^{S} \tag{A-10h}$$

$$F_m = -\sin \gamma' G_m^S$$
 (A-10i)

$$H_{m} = G_{m}^{C} \tag{A-10j}$$

The surface electric current distribution directed along \hat{t} and $\hat{\phi}$ can also be expanded in terms of Fourier modes, as follows:

$$J_{t}(t', \phi') = \frac{1}{2\pi\rho'} \sum_{n=-\infty}^{\infty} J_{t}^{n}(t') e^{jn\phi'}$$
(A-11a)

$$J_{\phi}(t',\phi') = \sum_{n=-\infty}^{\infty} J_{\phi}^{n}(t') e^{jn\phi'}$$
 (A-11b)

Since the G_m coefficients in Equation A-10 depend only on $(t,\,t',\,z,\,z')$, the above current expansions can be substituted into the integrals of Equations A-10c to A-10f. Again invoking the orthogonality relationship that the integrals exist only for m=n with respect to the ϕ' integration, we further obtain the following coupled integral equations in terms of only J_t^m (t') and J_{φ}^m (t') along a particular generating arc of the body of revolution:

$$\int_{-\pi}^{\pi} E_{t}^{i}(t, \phi) e^{-jm\phi} d\phi = \underline{L}_{11}''(J_{t}) + \underline{L}_{12}''(J_{\phi})$$
 (A-12a)

$$\int_{-\pi}^{\pi} E_{\phi}^{i}(t, \phi) e^{-jm\phi} d\phi = \underline{L}_{21}''(J_{t}) + \underline{L}_{22}''(J_{\phi})$$
 (A-12b)

where

$$L''_{11} (J_t) = \frac{j\omega\mu_0}{4\pi} \int_{t'} J_t^m (t') D_m dt'$$

$$+ \frac{j}{4\pi\omega\epsilon_0} \frac{\partial}{\partial t} \int_{t'} \frac{\partial}{\partial t'} [J_t^m (t')] G_m dt' \qquad (A-12c)$$

$$L''_{12} (J_{\phi}) = \frac{j\omega\mu_{0}}{2} \int_{t'} J_{\phi}^{m} (t') E_{m} \rho' dt'$$

$$+ \frac{j}{2\omega\epsilon_{0}} \frac{\partial}{\partial t} \int_{t'} J_{\phi}^{m} (t') (jm) G_{m} dt'$$

$$L''_{21} (J_{t}) = \frac{j\omega\mu_{0}}{4\pi} \int_{t'} J_{t}^{m} (t') F_{m} dt'$$

$$+ \frac{j}{4\pi\omega\epsilon_{0}\rho} \int_{t'} \frac{\partial}{\partial t'} [J_{t}^{m} (t')] (jm) G_{m} dt'$$

$$+ \frac{j}{2\omega\epsilon_{0}\rho} \int_{t'} J_{\phi}^{m} (t') H_{m} \rho' dt'$$

$$+ \frac{j}{2\omega\epsilon_{0}\rho} \int_{t'} J_{\phi}^{m} (t') (jm)^{2} G_{m} dt'$$

$$(A-12e)$$

III. Reduction to Modal Matrix Form

The smooth generating arc is now approximated by small linear segments as shown in Figure A-2. In Equations A-12a and A-12b, the unknown currents, J_{t}^{m} (t') and J_{φ}^{m} (t'), are expanded by piecewise pulse functions shown in Figures A-2a and A-2b:

$$J_{t}^{m}(t') = \sum_{n=1}^{N} I_{t}^{mn} P_{1}^{n}(t')$$
 (A-13a)

$$P_1^n(t') = \{ \begin{cases} 1 & t_{n-\frac{1}{2}} \le t' \le t_{n+\frac{1}{2}} \end{cases}$$
 (A-13b)

$$J_{\phi}^{m}(t') = \sum_{k=1}^{L+1} I_{\phi}^{m\ell} P_{2}^{\ell}(t')$$
 (A-13c)

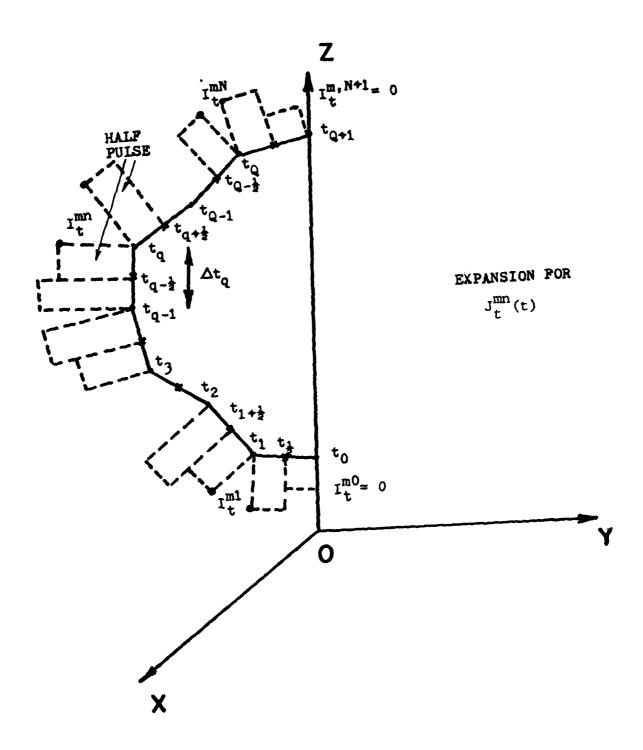


Fig. A-2a. GENERATING ARC AT ϕ = 0 OF THE BODY OF REVOLUTION

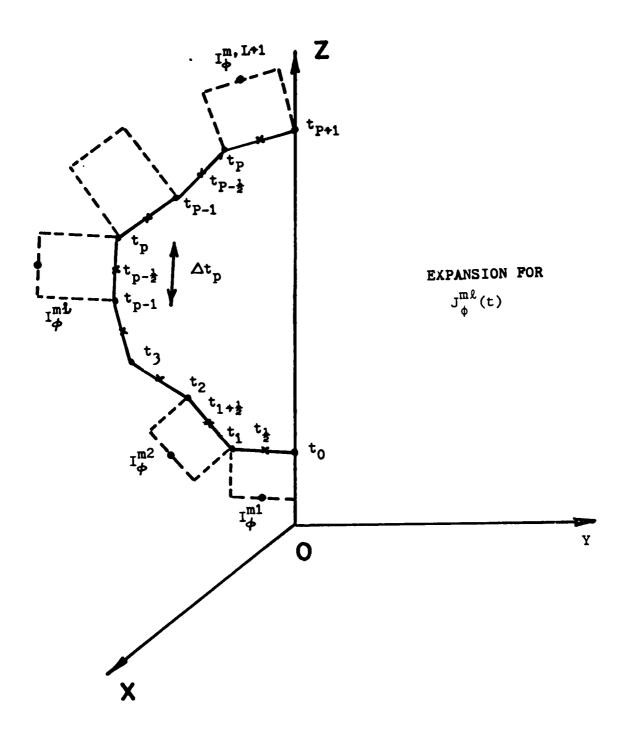


Fig. A-2b. GENERATING ARC AT ϕ = 0 OF THE BODY OF REVOLUTION

$$P_2^{\ell}(t') = \{ \frac{1}{0} t_{\ell-1} \le t' \le t_{\ell+1} \}$$
 (A-13d)

and the distribution

$$\frac{\partial}{\partial t'} \left[\rho' \ J_t^m \left(t' \right) \right] = \sum_{n=1}^{N+1} \left[\frac{I_t^{mn} - I_t^m, n-1}{\Delta t_n} \right] P_2^n \left(t' \right) \tag{A-13e}$$

For a closed or open body of revolution,

$$I_{t}^{mo} = I_{t}^{m}, \ ^{N+1} \equiv 0$$
 (A-13f)

and are appropriately represented by half pulses as shown in Figure A-2a. Similarly, for a closed body of revolution, the current J_{φ}^{m} (t') approaches zero as t' \rightarrow t₀ and t' \rightarrow t_{N+1} for m \neq ±1, and approaches a constant for m=±1 so that the full pulses I_{φ}^{m} , L+1 are very small values.

To reduce the coupled integral equations to a matrix form, Equation A-12a is tested at the various match points t_{v_1} , v_2 , v_3 , v_4 , v_5 , v_5 , v_6 , v_7 , v_8 , v_8 , v_8 , v_8 , v_9

$$\psi (t_1, t_2; t_v, m) = \int_{t_1}^{t_2} G_m (t_v, t') dt'$$
 (A-14a)

$$\psi^{\rho}(t_1, t_2; t_v, m) = \int_{t_1}^{t_2} G_m(t_v, t') \rho' dt'$$
 (A-14b)

and the matched weight functions

$$W_{s} (\Delta t_{v}, \gamma_{v}) = \frac{1}{2} [\Delta t_{v+1} \sin \gamma_{v+1} + \Delta t_{v} \sin \gamma_{v}]$$
 (A-14c)

$$W_{c} (\Delta t_{v}, \gamma_{v}) = \frac{1}{2} [\Delta t_{v+1} \cos \gamma_{v+1} + \Delta t_{v} \cos \gamma_{v}]$$
 (A-14d)

we obtain the linear algebraic modal equations:

$$V_{t_{v}}^{m} = Z_{11_{v}}^{mn} I_{t}^{mn} + Z_{12_{v}}^{mn} I_{\phi}^{m1}$$
 (A-15a)

$$V_{\phi_p}^{m} = Z_{21_p}^{mn} I_{t}^{mn} + Z_{22_p}^{m1} I_{\phi}^{m1}$$
 (A-15b)

$$n = 1, 2,N$$

 $v = 1, 2,N$
 $l = 1, 2,N+1$
 $l = 1, 2,N+1$

where the various modal impedance parameters are given by,

$$\begin{split} Z_{11}^{mn} &= \frac{j\omega\mu_{0}}{8\pi} \sin\,\gamma_{n} \,\, W_{s} \,\, (\Delta t_{v},\,\gamma_{v}) \,\, \big[\psi(t_{n-\frac{1}{2}},\,t_{n};\,t_{v},\,m+1) \\ &\quad + \,\psi(t_{n-\frac{1}{2}},\,t_{n};\,t_{v},\,m-1)\big] \\ &\quad + \frac{j\omega\mu_{0}}{8\pi} \,\sin\,\gamma_{n+1} \,\, W_{s} \,\, (\Delta t_{v},\,\gamma_{v}) \,\, \big[\psi(t_{n},\,t_{n+\frac{1}{2}};\,t_{v},\,m+1) \\ &\quad + \,\psi(t_{n},\,t_{n+\frac{1}{2}};\,t_{v},\,m-1)\big] \\ &\quad + \frac{j\omega\mu_{0}}{4\pi} \,\cos\,\gamma_{n} \,\, W_{c} \,\, (\Delta t_{v},\,\gamma_{v}) \,\, \big[\psi(t_{n-\frac{1}{2}},\,t_{n};\,t_{v},\,m)\big] \\ &\quad + \frac{j\omega\mu_{0}}{4\pi} \,\cos\,\gamma_{n+1} \,\, W_{c} \,\, (\Delta t_{v},\,\gamma_{v}) \,\, \big[\psi(t_{n},\,t_{n+\frac{1}{2}};\,t_{v},\,m)\big] \\ &\quad + \frac{j}{4\pi\omega\epsilon_{0}\Delta t_{n}} \,\, \big[\psi(t_{n-1},\,t_{n};\,t_{v+\frac{1}{2}},\,m) \,-\,\psi(t_{n-1},\,t_{n};\,t_{v-\frac{1}{2}},\,m)\big] \\ &\quad - \,\, \frac{j}{4\pi\omega\epsilon_{0}\Delta t_{n+1}} \,\, \big[\psi(t_{n},\,t_{n+1};\,t_{v+\frac{1}{2}},\,m) \,-\,\psi(t_{n},\,t_{n+1};\,t_{v-\frac{1}{2}},\,m)\big] \end{split} \tag{A-15c} \end{split}$$

$$\begin{split} Z_{12}^{m1} &= \frac{\omega \mu_{0}}{4} \; W_{S} \; (\Delta t_{v}, \; \gamma_{v}) \; [\psi^{\rho}(t_{\chi-1}, \; t_{\chi}; \; t_{v}, \; m-1) \\ &- \psi^{\rho}(t_{\chi-1}, \; t_{\chi}; \; t_{v}, \; m+1)] \\ &- \frac{m}{2\omega\mu_{0}} \; [\psi(t_{\chi-1}, \; t_{\chi}; \; t_{v+\frac{1}{2}}, \; m) \; - \; \psi(t_{\chi-1}, \; t_{\chi}; \; t_{v-\frac{1}{2}}, \; m)] \qquad (A-15d) \\ Z_{21}^{mn} &= \frac{\omega\mu_{0}}{8\pi} \; \Delta t_{p} \; \sin \, \gamma_{n} \; [\psi(t_{n-\frac{1}{2}}, \; t_{n}; \; t_{p-\frac{1}{2}}, \; m+1) \\ &- \psi(t_{n-\frac{1}{2}}, \; t_{n}; \; t_{p-\frac{1}{2}}, \; m-1)] \\ &+ \frac{\omega\mu_{0}}{8\pi} \; \Delta t_{p} \; \sin \, \gamma_{n+1} \; [\psi(t_{n}, \; t_{n+\frac{1}{2}}; \; t_{p-\frac{1}{2}}, \; m+1) \\ &- \psi(t_{n}, \; t_{n+\frac{1}{2}}; \; t_{p-\frac{1}{2}}, \; m-1)] \\ &- \frac{m\Delta t_{p}}{4\pi\omega\varepsilon_{0}} \frac{[\psi(t_{n-1}, \; t_{n}; \; t_{p-\frac{1}{2}}, \; m)]}{[\psi(t_{n}, \; t_{n+1}; \; t_{p-\frac{1}{2}}, \; m)]} \qquad (A-15e) \end{split}$$

and

$$Z_{22_{p}}^{m1} = \frac{j\omega\mu_{0}}{4} \Delta t_{p} \left[\psi^{\rho}(t_{\ell-1}, t_{\ell}; t_{p-\frac{1}{2}}, m+1) + \psi^{\rho}(t_{\ell-1}, t_{\ell}; t_{p-\frac{1}{2}}, m-1) \right] - \frac{jm^{2} \Delta t_{p}}{2\omega\epsilon_{0}^{\rho}p^{-\frac{1}{2}}} \left[\psi(t_{\ell-1}, t_{\ell}; t_{p-\frac{1}{2}}, m) \right]$$
(A-15f)

Now, the left-hand-side excitation terms in Equations A-15a and A-15b are obtained for a particular incident plane-wave excitation. For negative values of the modes (-m), $Z_{11}^{-mn} = Z_{11}^{mn}$, $Z_{12}^{-m\,\ell} = -Z_{12}^{m\,\ell}$, $Z_{21}^{-mn} = -Z_{21}^{mn}$ and $Z_{22}^{-m\,\ell} = Z_{22}^{m\,\ell}$.

IV. Modal Excitation Terms

In Equation A-4, for a plane wave incident on a body of revolution (Figure A-1), we have

$$\vec{E}^{i} (\vec{r}) = \vec{E}_{o}^{i} e^{-jk \hat{n}^{i} \cdot \vec{r}}, \qquad (A-16a)$$

and in terms of θ - and ϕ - polarization of the incident field we have

$$\vec{E}_0^i = E_\theta^i \hat{\theta}^i + E_\phi^i \hat{\phi}^i . \tag{A-16b}$$

The plane wave can be resolved into a sum of cylindrical modes given by

$$e^{-jk\hat{n}^{\dagger}\cdot\hat{r}} = e^{jkz} \cos \theta^{\dagger} \sum_{n=-\infty}^{\infty} j^{n} J_{n}(kp \sin \theta^{\dagger}) e^{jn(\phi-\phi^{\dagger})}$$
 (A-16c)

where J_n is the Bessel function of order n. According to Equations A-12a and A-12b, by performing the modal expansion for the E_t^i and E_ϕ^i components of the plane wave excitation, we obtain the following driving terms for Equations A-15a and A-15b:

$$V_{t_{v}}^{m} = \begin{cases} E_{\theta}^{i} \cos \theta^{i} W_{s} (\Delta t_{v}, \gamma_{v}) \left[j^{m-1} J_{m-1} (k \rho_{v} \sin \theta^{i}) \right] \\ + j^{m+1} J_{m+1} (k \rho_{v} \sin \theta^{i}) \right] - 2E_{\theta}^{i} \sin \theta^{i} W_{c} (\Delta t_{v}, \gamma_{v}) \end{cases}$$

$$\left[j^{m} J_{m} (k \rho_{v} \sin \theta^{i}) \right] - E_{\phi}^{i} W_{s} (\Delta t_{v}, \gamma_{v}) \cdot J_{m-1}^{m} \left[J_{m-1} (k \rho_{v} \sin \theta^{i}) + J_{m+1} (k \rho_{v} \sin \theta^{i}) \right] \end{cases} \pi e^{jkz_{v}} \cos \theta^{i} - jm\phi^{i} = V_{t_{v}}^{m\theta} + V_{t_{v}}^{m\phi} \tag{A-17a}$$

and

$$V_{\phi_{p}}^{m} = \left\{ E_{\theta}^{i} \cos \theta^{i} j^{m} \left[J_{m-1}(k\rho_{p-l_{2}} \sin \theta^{i}) + J_{m+1}(k\rho_{p-l_{2}} \sin \theta^{i}) \right] + E_{\phi}^{i} \left[j^{m-1} J_{m-1}(k\rho_{p-l_{2}} \sin \theta^{i}) + j^{m+1} J_{m+1}(k\rho_{p-l_{2}} \sin \theta^{i}) \right] \right\}$$

$$\pi \Delta t_{p} e^{jkz_{p-l_{2}} \cos \theta^{i}} e^{-jm\phi^{i}}$$

$$= V_{\phi_{p}}^{m\theta} + V_{\phi_{p}}^{m\phi} \qquad (A-17b)$$

where E^i_θ and E^i_φ are the amplitudes for the $\theta-$ and $\varphi-$ polarizations. We note in Equations A-17a and A-17b the driving vector for a given mode is the sum of contributions from the two $\theta-$ and $\varphi-$ polarizations. For negative values of the modes (-m), $V^{-m\theta}_t = V^{m\theta}_t$, $V^{-m\theta}_\varphi = -V^{m\theta}_\varphi$, and $V^{-m\varphi}_t = -V^{m\varphi}_t$, $V^{-m\varphi}_\varphi = V^{m\varphi}_\varphi$.

V. Modal Matrix Solution

According to Equations A-15a and A-15b, we have the matrix equation for mode m,

$$\begin{bmatrix} z_{11}^{mn} & z_{12}^{m\ell} \\ z_{21}^{mn} & z_{22}^{m\ell} \end{bmatrix} \qquad \begin{bmatrix} I_{t}^{mn} \\ I_{\phi}^{m} \end{bmatrix} = \begin{bmatrix} v_{t}^{m} \\ v_{\phi}^{m} \end{bmatrix}$$

$$(A-18)$$

The matrix equation is solved and the solution for the induced current vectors obtained both for θ - and ϕ - polarizations, for +m modes

$$\begin{bmatrix} I_{\mathbf{t}}^{mn} \\ I_{\mathbf{\phi}}^{m\ell} \end{bmatrix} = \begin{bmatrix} I_{\mathbf{t}}^{mn} \\ I_{\mathbf{\phi}}^{m\ell} \\ I_{\mathbf{\phi}_{\theta}}^{m\ell} \end{bmatrix} + \begin{bmatrix} I_{\mathbf{t}}^{mn} \\ I_{\mathbf{\phi}}^{m\ell} \\ I_{\mathbf{\phi}_{\Phi}}^{m\ell} \end{bmatrix}$$
(A-19a)

and for -m modes

$$\begin{bmatrix} I_{\mathbf{t}}^{-mn} \\ I_{\Phi}^{-m\ell} \end{bmatrix} = \begin{bmatrix} I_{\mathbf{t}}^{mn} \\ -I_{\Phi}^{m\ell} \end{bmatrix} + \begin{bmatrix} -I_{\mathbf{t}}^{mn} \\ I_{\Phi}^{m\ell} \end{bmatrix}$$

$$(A-19b)$$

Hence, referring to Equations A-11a and A-11b; A-13a and A-13b; and A-19a and A-19b, the distribution of the induced current for a given plane wave excitation is given by:

$$J_{\mathbf{t}}(\mathbf{t}, \phi) = \frac{1}{2\pi\rho} \sum_{n=1}^{N} \left[I_{\mathbf{t}_{\theta}}^{\text{on}} + 2 \sum_{m=1}^{\infty} \left\{ I_{\mathbf{t}_{\theta}}^{\text{mn}} \cos m\phi \right\} \right]$$

$$+ I_{\mathbf{t}_{\phi}}^{\text{on}} + 2 \sum_{m=1}^{\infty} \left\{ I_{\mathbf{t}_{\phi}}^{\text{mn}} \sin m\phi \right\} \right] P_{\mathbf{l}}^{n} (\mathbf{t}) \qquad (A-20a)$$

$$J_{\phi}(t, \phi) = \sum_{n=1}^{N+1} \left[I_{\phi_{\theta}}^{on} + 2 \sum_{m=1}^{\infty} \left\{ I_{\phi_{\theta}}^{mn} \cos m\phi \right\} + I_{\phi_{\phi}}^{on} + 2 \sum_{m=1}^{\infty} \left\{ I_{\phi_{\phi}}^{mn} \sin m\phi \right\} \right] P_{2}^{n} (t)$$

$$(A-20b)$$

VI. Application to the Hybrid MOM/FD-TD Case Studies of Section 7.4

Cases 1 and 2: Illumination of an Open-Ended Cylinder

Figure A-3 depicts the coordinate systems used for the MOM/FD-TD hybrid analysis of the open-ended cylinder for both Case 1 - Axial Incidence and Case 2 - Oblique (45°) Incidence with TM polarization. Note the different coordinate systems used for the MOM part of the analysis [9] and the FD-TD part of the analysis.

Figure A-4 graphs the magnitude of the MOM modal coefficients* of the equivalent surface electric current at the cylinder aperture for Case 1. Since only the m=1 mode is present, the equivalent aperture current is given by [9]

$$\overline{J}(t, \phi) = \hat{t} J_t(t) \cos \phi + \hat{\phi} j J_{\phi}(t) \sin \phi$$
 amps/meter (A-21)

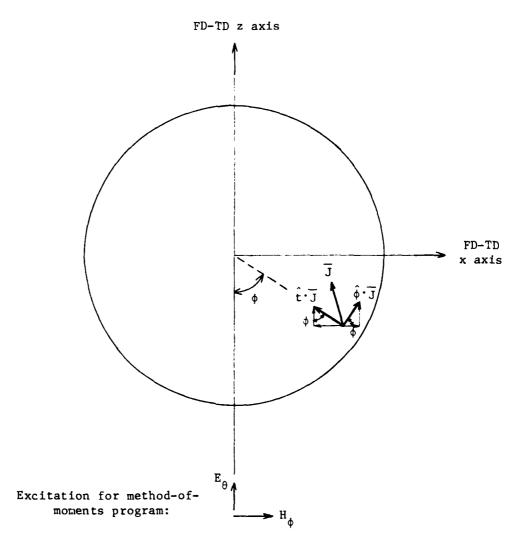
for any point (t, ϕ) on the aperture. This can be easily converted to the \hat{x} and \hat{z} coordinates of the FD-TD system to derive J_{χ} and J_{z} for step 2 of the analysis, as follows:

$$J_x = (\hat{\phi} \cdot \overline{J}) \cos \phi - (\hat{t} \cdot \overline{J}) \sin \phi$$
 amps/meter (A-22a)

$$J_z = (\hat{\phi} \cdot \overline{J}) \sin \phi + (\hat{t} \cdot \overline{J}) \cos \phi$$
 amps/meter (A-22b)

At all locations of E_X and E_Z in the cylinder aperture, J_X and J_Z can now be inserted as field sources via the ∇ x \overline{H} part of the FD-TD algorithm. Specifically, Equations 9d and 9f of Section 2.2.1 are re-written for these points as

^{*}For clarity, only the magnitude is graphed. However, in computing \overline{J} (t, ϕ), both the real and imaginary parts are required.



 $\hat{\textbf{t}}$, $\hat{\boldsymbol{\phi}}$: method-of-moments program co-ordinates

J: surface current derived from method-of-moments program

Fig. A-3. COORDINATE SYSTEMS FOR MOM/FD-TD HYBRID ANALYSIS
OF OPEN-ENDED CYLINDER AT CYLINDER APERTURE
(AXIAL INCIDENCE CASE AND 45°/TM INCIDENCE CASE)

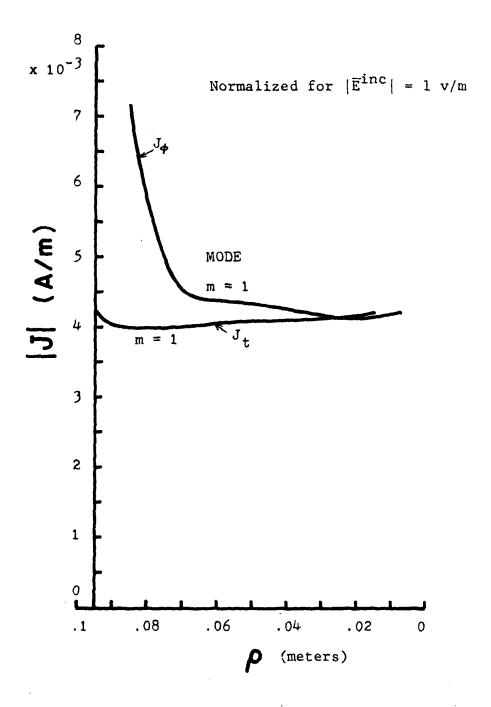


Fig. Λ-4. MODE COEFFICIENTS FOR APERTURE EQUIVALENT ELECTRIC CURRENT, HYBRID MOM/FD-TD FORMULATION OF AXIAL INCIDENCE ILLUMINATION OF OPEN-ENDED CYLINDER

$$m = MEDIA(i+\frac{1}{2},j,k)$$

$$\widetilde{E}_{x}^{n+1} = C_{a}^{n} (m) \widetilde{E}_{x}^{n} (i+\frac{1}{2},j,k) + C_{b}^{n} (m) (H_{z}^{1}(i+\frac{1}{2},j+\frac{1}{2},k) - H_{z}^{1}(i+\frac{1}{2},j-\frac{1}{2},k) + \frac{n+\frac{1}{2}}{y} (i+\frac{1}{2},j,k-\frac{1}{2}) - H_{y}^{1}(i+\frac{1}{2},j,k+\frac{1}{2}) + J_{x}^{1}(i+\frac{1}{2},j,k)$$

$$(A-23a)$$

 $m = MEDIA(i,j,k+\frac{1}{2})$

In Equation A-23a, specifying J_{χ} in the aperture is equivalent to specifying the addition of a discontinuity in the z-directed tangential magnetic field, H_{χ} , across the aperture source plane. Namely, we have added

$$J_{x} = H_{z}^{-} - H_{z}^{+},$$
 (A-24a)

where H_Z^- and H_Z^+ are tangential magnetic fields located an infinitesimal distance to either side of the equivalent aperture source plane. This procedure is consistent with that originally discussed by Schelkunoff [23]. In a similar manner, specifying J_Z in the aperture in Equation A-23b is equivalent to specifying the addition of a discontinuity in the x-directed tangential magnetic field, H_V , across the aperture source plane, namely

$$J_{z} = H_{x}^{-} - H_{x}^{+}.$$
 (A-24b)

Figures A-5a and A-5b graph the magnitude of the MOM modal coefficients of the equivalent electric current at the cylinder aperture for Case 2. Here, it is seen that modes 0, 1, 2, and 3 predominate for $J_{\rm t}$, and modes 1, 2, and 3 predominate for $J_{\rm p}$. Thus, the equivalent aperture current is given by [9]

$$J_{t} \hat{t} = \hat{t} \{J_{t_{0}} + \sum_{m=1}^{\infty} J_{t_{m}} \cos(m\phi)\}$$

$$\simeq -\hat{\rho} \{J_{t_{0}} + \sum_{m=1}^{3} J_{t_{m}} \cos(m\phi)\}$$

$$J_{\phi} \hat{\phi} = \hat{\phi} \{\sum_{m=1}^{\infty} J_{\phi_{m}} \sin(m\phi)\}$$

$$\simeq \hat{\phi} \{\sum_{m=1}^{3} J_{\phi_{m}} \sin(m\phi)\}$$

$$(A-25b)$$

for any point (t, ϕ) on the aperture. (Note that $\hat{t} = -\hat{\rho}$ on the aperture locus.) Again, this can easily be converted to the \hat{x} and \hat{z} coordinates of the FD-TD system to derive J_x and J_z for step 2 of the analysis using Equations A-22a and A-22b.

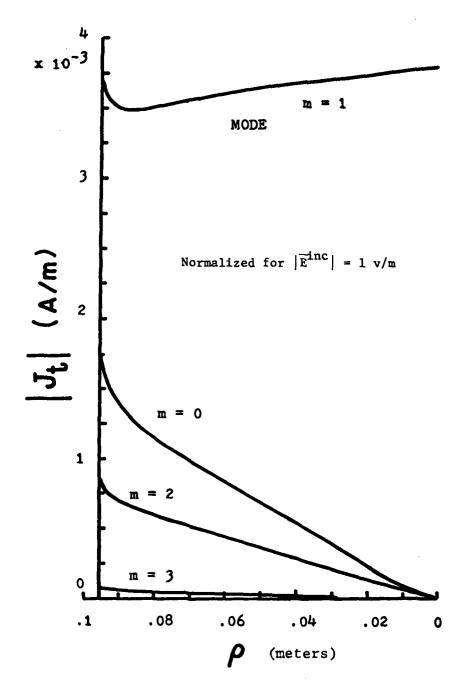


Fig. A-5a. MODE COEFFICIENTS FOR APERTURE EQUIVALENT ELECTRIC CURRENT, HYBRID MOM/FD-TD FORMULATION OF OBLIQUE INCIDENCE TM ILLUMINATION OF OPEN-ENDED CYLINDER

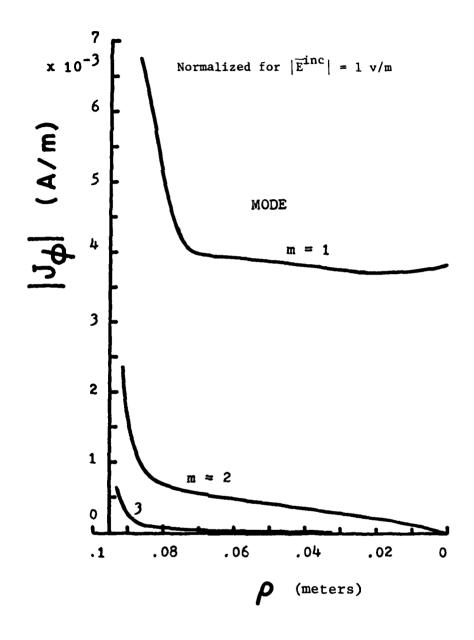


Fig.A-5b. MODE COEFFICIENTS FOR APERTURE EQUIVALENT ELECTRIC CURRENT, HYBRID MOM/FD-TD FORMULATION OF OBLIQUE INCIDENCE TM ILLUMINATION OF OPEN-ENDED CYLINDER

Case 3: Illumination of a Missile Guidance Section

Figure A-6 depicts the geometry and coordinate systems used for the MOM/FD-TD hybrid analysis of the loaded missile guidance section. The coordinate systems used are the same as shown in Figure A-3 for the open-ended cylinder.

Figure A-7 graphs the magnitude of the MOM modal coefficients of the equivalent electric current at the nose cone sleeve-fitting aperture and the nose aperture. Similar to the axial-incidence case of the cylinder, only the m=1 mode is present.

For the nose aperture, both J_t and J_φ coefficients were used to form J (t, φ), and then, J_χ and J_Z components for the FD-TD analysis of step 2. However, for the sleeve-fitting aperture, only the J_t coefficient was used to form J (t, φ) and then, J_y for the FD-TD analysis. This is because $|J_\varphi| \leq 0.05 \ |J_t|$ at the sleeve fitting, and could thus be neglected without significant error.

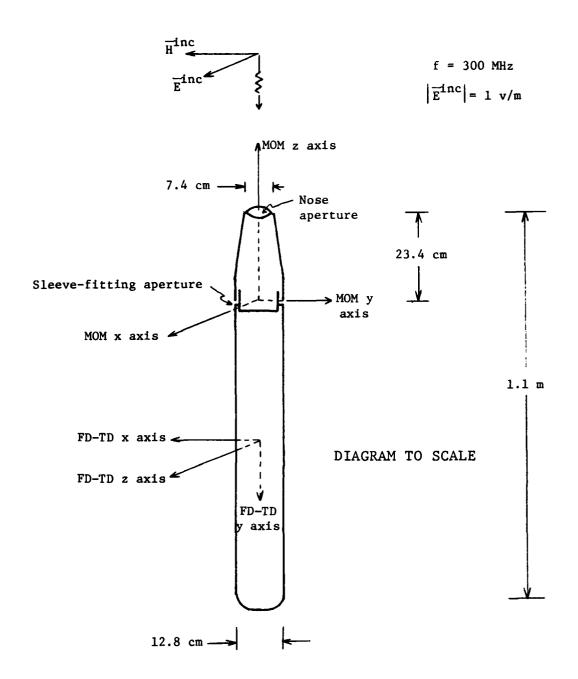


Fig. A-6. GEOMETRY AND COORDINATE SYSTEMS FOR MOM/FD-TD HYBRID ANALYSIS OF MISSILE GUIDANCE SECTION, AXIAL INCIDENCE

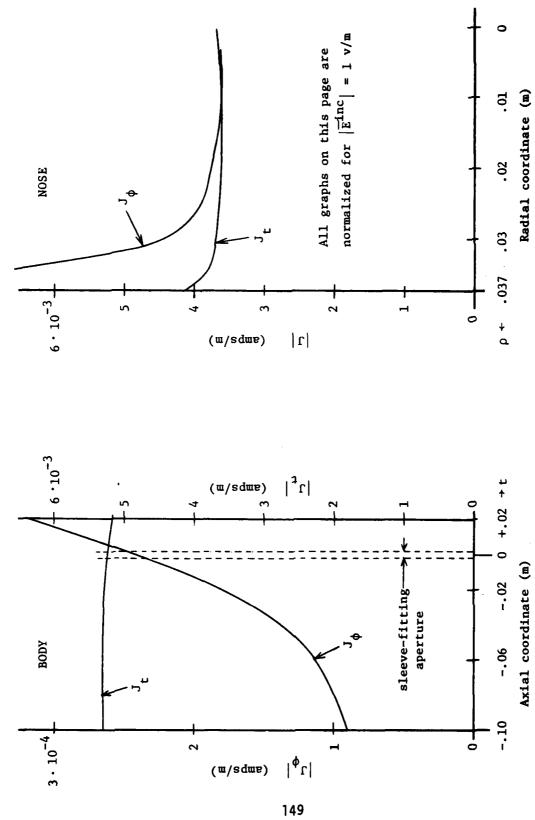


Fig. A-7. MODE COEFFICIENTS FOR APERTURE EQUIVALENT ELECTRIC CURRENT, HYBRID MOM/FD-TD FORMULATION OF AXIAL INCIDENCE ILLUMINATION OF MISSILE GUIDANCE SECTION

APPENDIX B

Integral Equations for the Finite Wire / Narrow Slot Geometry

This appendix summarizes the integral equations which have been utilized to obtain the numerical results shown in Section 7.0 of this report for the wire / slot geometry of Figure 36. The complete set of integro-differential equations for the general problem of a finite-length wire excited through a narrow slot in a conducting screen appears in detail in the literature in References 11, 27, and 28. These references also provide numerical results for coupling between the slot and the wire based on the location and orientation of the wire with respect to the slot.

For the narrow slot / finite wire geometry, we have the coupled integral equations [27]:

$$\left(\frac{\partial^{2}}{\partial x^{2}} + k^{2}\right) \frac{\varepsilon}{2\pi} \int_{y'=-\frac{w}{2}}^{+\frac{w}{2}} \int_{x'=-\frac{\ell}{2}}^{+\frac{\ell}{2}} m(x')\xi(y') K_{SS}(x, x', y') dx'dy' + \frac{j_{\omega\varepsilon}}{2} \frac{\partial Ay}{\partial z}(x) = -j \frac{k^{2}}{\omega} H_{x}^{i}(x)$$
(B-1a)

$$x \in (-\frac{\ell}{2}, +\frac{\ell}{2}), SLOT$$

$$\left(\frac{\partial^{2}}{\partial s^{2}} + k^{2}\right) \frac{\mu}{4\pi} \int_{s'=-\frac{L}{2}}^{+\frac{L}{2}} I(s') K_{WW}(s, s') ds'$$

$$+ j \omega \mu \cos \beta \frac{\partial F_{x}(s)}{\partial z} = 0$$
(B-1b)

s
$$\epsilon$$
 $\left(-\frac{L}{2}, +\frac{L}{2}\right)$, WIRE

$$K_{SS}(x, x', y') = \frac{e^{-jkR}ss}{R_{SS}}$$
(B-2a)

$$R_{SS} = [(x-x')^2 + y'^2]^{\frac{1}{2}}$$
 (B-2b)

$$K_{WW}(s, s') = \frac{e^{-jkR_{WW}}}{R_{WW}} - \frac{e^{-jkR^{i}}}{R^{i}}$$
 (B-3a)

$$R_{ww} = [a^2 + (s-s^2)^2]^{\frac{1}{2}}$$
 (B-3b)

$$R^{i} = [4Z_{c}^{2} + (s-s')^{2}]^{\frac{1}{2}}$$
 (B-3c)

$$\frac{\partial A_{y}}{\partial z} = -2 \cdot \cos \beta \cdot z_{c} \cdot \frac{\mu}{4\pi} \int_{s'=-\frac{L}{2}}^{+\frac{L}{2}} I(s') G_{SW}(x, s') ds'$$
(8-4a)
$$(x, y=0, z=0)$$

$$G_{SW}(x, s') = -\left[\frac{jk}{d} + \frac{1}{d^2}\right] \frac{e^{-jkd}}{d}$$
 (B-4b)

$$d = \{[x-(x_c + s' \cos \alpha)]^2 + [y_c + s' \cos \beta]^2 + [z_c]^2\}^{\frac{1}{2}}$$
 (B-4c)

$$\frac{\partial F_{X}}{\partial z} | = z_{C} \frac{\varepsilon}{2\pi} \int_{X'=-\frac{R}{2}}^{+\frac{R}{2}} m(x') G_{WS}(s, x') dx'$$
(B-5a)

$$G_{WS}(s, x') = -\left[\frac{jk}{D} + \frac{1}{D^2}\right] \frac{e^{-jkD}}{D}$$
 (B-5b)

$$D = \{[(x_c + s \cos \alpha) - x']^2 + [y_c + s \cos \beta]^2 + [z_c]^2\}^{\frac{1}{2}}$$
 (8-5c)

The integral equations (B-la and b) are solved by the method-of-moments numerical approach [13], [27].

MISSION of Rome Air Development Center

RADC plans and executes research, development, test and selected acquisition programs in support of Command, Control Communications and Intelligence (C^3I) activities. Technical and engineering support within areas of technical competence is provided to ESP Program Offices (POs) and other ESD elements. The principal technical mission areas are communications, electromagnetic guidance and control, surveillance of ground and aerospace objects, intelligence data collection and handling, information system technology, ionospheric propagation, solid state sciences, microwave physics and electronic reliability, maintainability and compatibility.

END

DATE FILMED

DTIO

DTIC